Investigation of Grating based Resonating Structures on SOI Platform for Photonic Biosensors

Doctoral Thesis

Submitted by

Sourabh Sahu
Research Scholar
(College ID-2014REC006)

Under Supervision of

Dr. Ghanshyam Singh
Associate Professor,
Dept. of ECE, MNIT, Jaipur

DEPARTMENT OF ELECTRONICS & COMMUNICATION ENGINEERING
MALAVIYA NATIONAL INSTITUTE OF TECHNOLOGY, JAIPUR, INDIA

October 2017

Investigation of Grating based Resonating Structures on SOI Platform for Photonic Biosensors

Submitted By

Sourabh Sahu
Research Scholar
(College ID-2014REC9006)

Under Supervision of

Dr. Ghanshyam Singh
Associate Professor
Dept. of ECE, MNIT, Jaipur

Submitted in fulfillment of the requirements of the degree of Doctor of Philosophy to the

DEPARTMENT OF ELECTRONICS & COMMUNICATION ENGINEERING
MALAVIYA NATIONAL INSTITUTE OF TECHNOLOGY, JAIPUR, INDIA

October 2017

©Malaviya National Institute of Technology, Jaipur, India - 2017.

All rights reserved.

Certificate

This is to certify that the thesis entitled "**Investigation of Grating based Resonating Structures on SOI Platform for Photonic Biosensors**" being submitted by Sourabh Sahu is a bonafide research work carried out under my supervision and guidance in fulfillment of the requirement for the award of the degree of Doctor of Philosophy in the Department of Electronics & Communication Engineering, Malaviya National Institute of Technology Jaipur, India. The matter embodied in this thesis is original and has not been submitted to any other University or Institute for the award of any other degree.

_____

Dr. Ghanshyam Singh

(Associate Professor)

(Dept. of ECE, MNIT, Jaipur)

Declaration of Authorship

I, Sourabh Sahu, declare that this thesis titled, 'Investigation of Grating based Resonating Structures on SOI Platform for Photonic Biosensors' and the work presented in it are my own. I confirm that:

- This work was done wholly or mainly while in candidature for a research degree at this University.
- Where any part of this thesis has previously been submitted for a degree or any other qualification at this University or any other institution, this has been clearly stated.
- Where I have consulted the published work of others, this is always clearly attributed.
- Where I have quoted from the work of others, the source is always given. With the exception of such quotations, this thesis is entirely my own work.
- I have acknowledged all main sources of help.
- Where the thesis is based on work done by myself jointly with others, I have made clear exactly what was done by others and what I have contributed myself.

Signed: _____

Date: _____

Acknowledgment

I believe that in this world no one has been fulfilled without the support of the team. Here, I will take the opportunity to thank everyone who directly or indirectly makes an impression on my mind while working on my Ph.D.

I would like to express my sincere gratitude to my supervisor Dr. Ghanshyam Singh, Associate Professor in Department of Electronics and Communication Engineering. I am very fortunate to have him as my Ph.D. supervisor. His deep insight and motivating words always encouraged me to excel my skills. He is a person behind the evolution of my personality as a researcher. His unconditional help and suggestions always helped me to take a step forward in achieving my goals. He is an undoubtedly one of the most influential people in my career. I like to thank Dr. Vijay Janyani, Dr. Ritu Sharma and Dr. Ravi Kumar Maddila, members of my departmental research evaluation committee (DREC), for timely providing me the feedback on my work. Their suggestions always ignite me with some key ideas that helped me to think more clearly and precisely. It is my pleasure to thank our head of department Prof. K. K. Sharma, Prof. Vineet Sahula, and Prof. Vishwanath Sinha for the courses they taught me due to which I have developed an ability to think more clearly.

I am grateful to Prof. Jalil Ali (UTM, Malaysia) and Prof. Preecha P. Yupapin (TDT University, Vietnam) for providing me the fast and quick review on my work. I would also acknowledge the joint and collaborative research between the researchers of MNIT Jaipur, UTM Malaysia, and TDH Vietnam. Their suggestions helped me in improving the quality of my work, and especially increased the efficiency of my writing skills. I also thank the NSERC and SiEPIC program for providing the online course through edX that helped me to develop theoretical and experimental concepts related to recent technologies.

I am very fond of my family members for their love and kind support. My parents have a strong faith in me that helped me to concentrate more on my work. Whenever I feel depressed, a word with them relishes my energy. I am incredibly thankful to my wife Shivali, and this work would not be possible without her support. She has enthusiastically

supported me to accomplish my work. My son Gaurang, his humming sound in the evening made me forget all the tensions and helped me to reenergize myself.

Now I would like to thank all my friends and colleagues for their love and support. All the happier moment spent with them created timeless memories, which is impossible to forget. It is not possible to consider the contribution of all, but I take an opportunity to thank few ones who have significantly helped me that includes Nitesh Kumar, Shailendra Tripathi, Amit Garg, Yogendra Kumar, V Ramakrishna, Ashish Tyagi, Bipin Saw, Prathmesh Dali, Abhishek Godbole, Shruti Kalra, Dr. Sandeep Vyas, Dr. Monica Mathur, Dr. Nikhildeep Gupta, and Dr. Mukesh Gupta.

At last, above all, I would like to thank my God (Krshna and Shiv baba) for their kind love, support, and blessings. Their association with me is a sense of inner peace and joy.

Abstract

In this thesis, we have evaluated the performance of optical resonating device for the biosensing application. Mainly if the device uses the silicon-on-insulator (SOI) platform, then it is embedded with benefits such as advanced fabrication technology, an abundance of materials, simplified surface chemistry, etc. Photonic sensors are well suited for a label free biosensor, which have the immobilized biorecognition layer on the surface that binds only the intended analyte from the biomaterial. The change in the refractive index of the biomaterial on the surface alters the propagation characteristics of the optical mode that can be quantified for the detection of the biomaterials. Several photonic biosensor on SOI are utilizing this principle, each have their own advantages and limitations. The use of interferometer-based sensors is limited in terms of structure area for higher sensitivity, whereas the ring resonators suffer from low FSR values and requirement of a large substrate area. Substantive losses and increased complexity limit the use of Photonic crystal based sensing devices, while structures, which uses the surface-plasmon-resonance effect are very much sensitive to the quality of the deposited materials even a small deformity in the thickness or roughness occurred during the fabrication deviates the output of the device significantly. However, the sharp corners of the gratings are often rounded-off during the fabrication process. Due to this variability, only a slight shift in the stop band region occurs, but it can preserve the characteristics of the device. On comparing with other photonic structures, the sidewall grating based resonating device provides high Q factor with the linear response to a change in refractive index of the biomaterial

In this context, the thesis proposes the grating waveguide based resonating devices for biosensing application. The first structure comprises of the cascading of the grating waveguides, since in the conventional grating waveguides the lower stopband region limits the detection range. Therefore, the structure comprising of the cascading of two sidewall grating waveguides tuned to a different stopband regions is proposed. The configuration provides high Q resonating band at the center of the stopband of the order of 10^5. The study regarding the temperature stability is also performed. The device is having a sensitivity of

90 nm/RIU and a detection limit of the order of 10^{-4} RIU. For further improving the sensitivity, we have modified the structure to have a narrow reflection band by opting cladding modulated grating waveguide configuration. The structure is designed to have a lower interaction between the propagating field and gratings for lower periodic perturbation in the refractive index. For a variation of the waveguide thickness biosensing parameters are evaluated, and higher sensitivity is found for the 100 nm thick waveguide.

However, for further lowering the detection limit and increasing the sensitivity slot waveguide is used for the resonating structure. The purpose of is to increase the light-biomaterial interaction, and have a high Q resonating band. Here the considered configuration is based on the single and dual slot waveguides. The configuration of the waveguides are theoretically optimized to have higher sensitivity and then the gratings are designed. The dual slot waveguide shows a promising enhancement of the biosensing characteristics by providing a high sensitivity and a detection limit of the order of 10^{-6} RIU.

In a last segment, the resonating device consisting of the sub-wavelength (SWG) grating and strip waveguide for ring resonator is proposed. The SWG is used as a parallel bus waveguide and strip waveguide is used for the ring segment. The periodic configuration of the SWG waveguide allows the biomaterial to enter in the gap between the two subsequent gratings segments causes the direct interaction with the field components. Overall, in this thesis we have investigated the performance of the various resonating structure that uses SOI platform and can be fabricated using the CMOS fabrication facility and also suitable for lab-on-chip applications.

Contents

List of figures

List of Tables

Chapter 1

Introduction

The healthcare concern and expenses are the major societal problem. More easily accessible diagnostic equipment can remarkably improve the results. Currently, available diagnostics system such as ELISA (Enzyme-Linked-Immunosorbent-Assay) is having a sophisticated facility that can only be handled by well-trained personnel [1,2]. In addition, it consumes a high volume of reagents and antibodies for detection purposes. The ELISA technique is very sensitive, but it suffers from significant disadvantages such as costlier processing, required complicated lab setup, and time-consuming [3]. Hence, it is not extensively developed for the use of routine diagnostics of the disease. Over the last decade, researchers have been investing their energies for the development of a biosensor that has a high sensitivity, cheaper and can be readily available. The focus is to develop the micro or nanoscale sensor that can consume the lower volume of reagents and can be used for lab-on-chip applications.

Researchers have examined the performance of various sensing methods. The photonic sensor is a preferable choice due to its capability of providing high sensitivity and a lower detection limit, which is comparable to an existing laboratory based diagnostics [4–6]. These photonic sensors also have advantages such as compact size, immunity to electromagnetic interferences, ability to operate at room temperature, and are easily mass-produced [7,8]. For a photonic biosensor, label-free approach is a preferred methodology that provides a real-time monitoring of the specific molecular activity by capturing it to a surface of a sensor through particular bio-receptors, as compared to a more conducive method of labeling an intended analyte with a fluorescent tag [9–11]. It was shown that a nanostructured sensor offers advantages regarding sensitivity, selectivity, detection limit, and binding kinetics as against a non-structured biosensor. Additionally, if the nanostructured resonating device utilizes the silicon or compound of silicon material, the

biosensor embedded with benefits like low cost, flexible geometric possibility, and existing surface functionalization chemistry.

Silicon photonics is an emerging field and growing exponentially, it will soon outrun the current electronic-integration technology. Like the electronic industry revolutionized the computational process of equipment and enabled the production of gadgets such as tablets, mobile etc. Similarly, photonic technology is currently expanding to replace the well-equipped electronic industry [12]. The biosensor application is one of the excellent exploration of silicon photonics. The application of biosensors are drug detection, smart home healthcare systems, genetic disease, forensic analysis etc. The compact size biosensing devices with a microfluidic framework can easily integrate for Lab-on-chip (LOC) application.

The fundamental part of the biosensing device is a waveguide, which can facilitate the propagation of a signal. The waveguide on silicon-on-insulator (SOI) platform have high index contrast (ratio of the refractive index of the core and cladding region) that causes the signal to confine in the core region of the waveguide. Only small portion of the field manage to reach and propagate on the surface of the device (called as evanescent field). This evanescent field of the waveguide penetrates the biomaterial attached to its surface, which alters the propagation characteristics of the waveguide and the same is utilized for the quantification of a biomaterial [13–16]. However, it is seen that a use of the slot waveguide for resonators can be an excellent technique for detection of low concentration of analyte. Despite confining light in high index region of a waveguide, slot waveguide confines light in the low refractive index nanometer-size slot region. Thus, support an increase in light and biomaterial interaction [17–19]. Based on the optical modal propagation in these waveguides, several integrated optical devices have been investigated for sensing applications. The important considered biosensing characteristics are sensitivity and a detection limit. The efficient biosensor must have high sensitivity and lower limit-of-detection.

1.1 Literature Survey

The ideology behind the photonic biosensor is dependent on interaction between the light and biomaterial. The purpose is to observe the presence of biochemical analyte by measurable optical signals. There are various methods of implementations of photonic sensor, which are broadly classified corresponding to the optical characteristics harnessed [20–24]. In particular it is intuitive to distinguish between the refractive index (RI) and non-RI based sensor. Non-RI sensor's working principle are dependent on Stimulated Raman scattering (SERS), Fluorescence and Optical absorption [3,25–36].

The most fundamental photonic sensor is based on the linear waveguides, in this method absorption spectra of the intended biomolecule is utilized for detection purpose. The working of this sensor is govern by the Beer Lambert law that directly relates the optical absorption of the signal to the concentration of the molecules [37–39]. Hence, for highly sensitive device higher length of waveguide is desirable. Most prominently, the typical length of waveguide is of the order of millimeters to facilitate high mode to biomaterial overlap [15,40]. However, the longer length of waveguide embed with an additional disadvantage of increasing the propagation losses that significantly affect the performance of a device [14,41,42]. Apart from the planar waveguide based sensors, researchers have proposed a spiral waveguide and folded waveguides that significantly reduced the overall area of the sensing unit but the problem of losses persist [43–45]. Therefore, the researcher shifted their concentration for a development of compact resonant devices that could significantly reduce the overall dimension and can be utilized for LOC applications. The sensors based on resonant micro cavities are called as label free sensors or RI based sensors.

In RI based sensors, the change in spectral position corresponding to a change in refractive index of biomaterial is evaluated as a detection principle. A homogenous sensing which is referred to a presence of biomaterial over the cover or upper cladding region of the sensor is the fundamental entity required for a characterization of the biosensor. The change in the refractive index of a biomaterial changes the effective index of the mode propagation in a waveguide hence alters the resonance condition [46–50].

In particular, ring resonator configuration is widely explored by the researchers for biosensing applications. It works for two configuration all-pass and add-drop, which is dependent of the number of bus waveguide coupled to a ring waveguide. The dimension of the ring is required to be select in such a manner to accomplish a phase shift which is a multiple of 2π for different modes couple in a ring so that each one interferes constructively to support a resonance in the transmission spectra. In transmission spectra, series of resonant peaks are found that are concentrated on various wavelengths. The main optical characteristic concerning its spectra is Free Spectral Range (FSR) that relates the distance between the two consecutive resonance peaks. Bruns et al. in [51] explored a coupling of multiple ring in a single bus waveguide and introduced a possibility of multiplexed detection. Several researchers also explored the possibility of combining the resonance effect and optical absorption of a biomaterial using a vernier effect [24,52–54]. Lei et al. utilized a cascading of two rings to detect the various ethanol concentration and achieved a Q–factor of 2×10^4 and limit of detection (LOD) of 1.15×10^{-2} RIU [53]. A resonator-interferometer compound structure is represented in [55] showed a sensitivity of 688.3 nm/RIU. However a sensor consisting of a typical combination of SOI chip and surface plasmon Mach Zehnder interferometer demonstrated a sensitivity of 102 nm/RIU [56]. A study concerning a ring resonator based on slot waveguide demonstrated a sensitivity of 300 nm/RIU [57]. A resonator utilizing whispering gallery mode is presented in [58] with a sensitivity of 120 nm/RIU. The use of thinner waveguide increases the presence of field on the surface of the waveguide [13–15]. The ultra-thin waveguide (thickness < 100 nm) based ring resonator for biosensing application is proposed in [13], they have achieved a sensitivity of 100 nm/RIU and a LOD of 5×10^{-4} RIU for 90 nm thin waveguide. However, the main problem associated with the ring resonator architectures is an additional bending loss. It also requires large area in a substrate in fact higher ring radius is desirable for getting higher Q-factor that significantly influenced the sensitivity of the biosensor device. So one of our objective is to design a resonating structure that does not requires bend and have straight geometry.

The Bragg grating is one such configuration that provides straight resonating structure. Juggeser et al. have demonstrated a grating waveguide based resonating structure for a biosensing application on SOI platform [59]. They have demonstrated a generation of stop band region by periodically altering the waveguide width. The shifting of trailing edge of stop band region is used for change in refractive index of biomaterial. A reported sensitivity is 160 nm/RIU without an evaluation of LOD. Prabhathan et al. and Wang et al. have demonstrated a configuration that enables a generation of narrow peak at a middle of the stop band region [46,60]. Reported LOD in [46] is around 10^{-5} RIU and in [60] is around ~10^{-4} RIU. The narrow stop band region is limiting the overall detection range in both these devices. Kehl et al. in [61] studied the more advanced configuration, they have designed surface grating in a rib waveguide they have achieved a sensitivity of 75.8 nm/RIU and LOD of around 10^{-4} RIU. The main disadvantage of this configuration is the surface grating that required multiple fabrication steps for generation of precise grating hence increases the complexity. To further enhancing the biosensing characteristics slot waveguide is used for devising of resonator structures.

Unlike a strip and rib waveguide, slot waveguide confines an electric field of propagating signal in a low refractive index region. The higher presence of field in a slot region causes higher interaction between a signal and biomaterial. Claes et al. in [57] reported a biosensor based on slot waveguide based ring resonator with a sensitivity of 290 nm/RIU and LOD of 4.2×10^{-5} RIU. In corresponds to a grating resonator two configurations have been reported, first one have gratings on the outside of slot waveguide the higher sensitivity of 340 nm/RIU has been reported with a LOD of 3×10^{-4} RIU [62]. The other configuration have gratings in the inside of slot waveguide have reported a sensitivity of 290 nm/RIU with an improved LOD of ~10^{-5} RIU [63]. However, slot waveguide suffers from higher losses but direct interaction of electric field with gratings requires lesser number of gratings that significantly reduce the overall size of the device. Based on the study provided study we have modified the design to implement gratings in dual slot waveguide.

1.2 Motivation and Objectives

The aim of this thesis is to investigate and analyze the simplified optical resonating device that can be used for biosensing purpose. The proposed configurations make use of the silicon-on-insulator platform that also supports the CMOS fabrication feasibility. Based on the SOI platform various biosensing device such as an interferometer, ring resonator, disk resonator, photonic crystal, surface plasmon resonance, and Bragg grating have been proposed. Each configuration has their own characteristic features and limitations. The brief overview of the configurations are presented in chapter 2, however, the fundamental limitations that inhibit their functionality for an efficient biosensor are discussed here.

The use of interferometer for sensing applications is limited by sinusoidal dependence of the intensity that causes uncertainty in the detection of biomaterials, also the direct dependency of sensitivity for a length of an unbalanced arm increases the overall dimension of the device, and moreover, a low Q-factor is obtained which affects the limit-of-detection [20–22,24,64]. The ring and disk resonators based sensors have a lower value of free spectral range (FSR) that limits its detection range and additionally it suffers from higher bending losses that significantly affected the performance of the device [25,51,53,65]. The photonic crystal based sensor is highly sensitive and compact in size, but the complexity of manufacturing a precise dimension of the holes limits its usability. In addition, it also has a higher propagation and coupling losses. The inefficient coupling between the planar slab waveguide and photonic crystal waveguide notably alters the propagation characteristics of the device [66–70]. Whereas the response of the devices based on surface plasmon resonance is highly affected due to the thickness deformity of the deposited material, or the roughness occurred during fabrication [71–74]. In the grating waveguide, sharp corners of the gratings are often rounded-off during the fabrication process [75–77]. Due to this variability, only a slight shift in the stop band region occurs, but it can preserve the characteristics of the device.

In the view of above, we have aimed to design a resonant biosensor based on the sidewall grating structure. The following objectives have been contributed in this thesis,

- Before an actual design of the resonating device, the strip waveguide is studied and characterize through the experimental verification of the Michelson interferometer. Here we have discussed the various losses affecting the performance of the devices and biosensing parameters are evaluated.
- By considering the configuration of the strip waveguide, a sidewall grating is designed through the transfer matrix method. We have also provided a method to increase the stop band region in the transmission spectra by cascading two grating waveguides. Then the biosensor is designed by utilizing the configuration.
- To design a narrowband clad modulated grating waveguide for a generation of the narrow stop band in the transmission spectra. The aim is to minimize the interaction between the electric field and gratings to have a lower perturbation in the change in effective index of a waveguide. In addition, the effect of height for increasing the light matter interaction is discussed in detail for increasing the sensitivity and limit-of-detection.
- To confine a propagating electric field in a low refractive index slot region. The aim is to increase the interaction between a propagating field and biomaterial. Here we have proposed a novel technique of dual slot waveguide for enhancing the biosensing parameters. Apart from that, the sidewall gratings are also designed that provides a wide stop band region for a comparatively smaller number of gratings. The configuration provide high sensitivity and a detection limit of the order of 10^{-6} RIU.
- To design a hybrid resonating structure that consists of a sub-wavelength grating waveguide and strip waveguide. Since the sub-wavelength-grating waveguide is ideally, a loss less waveguide and the presence of a field on the gap region causes the increase interaction between the field and biomaterial. Moreover, the strip waveguide ideally have very low bending losses, hence the two configuration are combined to make a ring resonator configuration. The device is investigated for biosensing application with a value of sensitivity is around 206 nm/RIU.

1.3 Structure of Thesis

In this section, the brief overview of the various chapters of the thesis is presented. The work is carried out with an aim to demonstrate a nanostructured configuration suitable for a biosensing application. The content of the thesis is as follows – Chapter 1 introduces the fundamental requirements of the biosensor. The motivation and the brief introduction of objectives considered in this thesis are discussed in the later part of the chapter.

The chapter 2 consist of the detailed study of the biosensors including the importance of biorecognition layer and transducing mechanism. In this chapter, we have discussed the various key concepts such as the mechanism of optical sensing, requirements of lab-on-chip devices, a label based and label-free detection, biosensing performance metrics, etc. The brief overview of the various optical based sensing methodologies and photonic device configurations have also been discussed.

In chapter 3, theoretical and analytical methods for analyzing the photonic device is discussed. The detailed derivation with cutoff conditions is provided for mode propagation in the strip and slot waveguide. The brief study of the transfer matrix method and eigenmode expansion method is also considered. This thesis is concentrated on an application of the sidewall grating waveguide, hence the analytical modeling of the device and various terminologies related to it are derived in this chapter.

The configuration of the planar strip waveguide is utilized for the design of the Michelson Interferometer in chapter 4. The simulation and experimental study of the device is performed. The biosensing capability of the MI is also provided.

The resonating structure utilizing the sidewall grating is discussed in chapter 5. This chapter is divided into two parts; the first part discussed of a generation of the resonant band in the stop band region, while in the second part the novel design to generate the narrow stop band region using cladding modulated grating waveguide is presented. Both configurations are exploited for biosensing application. The analytical modeling of the cascaded grating waveguide is discussed in detail. The design is also considering the effect of temperature on the performance of the device. Whereas the cladding modulated grating

waveguide is designed that causes a minimal alteration in the effective index of the waveguide for a grating and non-grating region. Hence, the device provides narrow reflection band, and that characteristic is utilized for biosensing application. However, for increasing the sensitivity of a device it is analyzed with the variation in thickness values.

The chapter 6 provides an intuitive information about the slot waveguide. The dual slot waveguide is theoretically analyzed for optimizing the biosensing parameters, and then the gratings are designed in it. The sensitivity and limit-of-detection are superiorly improved through this configuration.

In the chapter 7, the novel design of ring resonator is presented. The design is a hybrid structure of the sub-wavelength grating and strip waveguide. The add-drop configuration of the ring resonator is designed in which two parallel channel are composed of sub-wavelength gratings and the central ring waveguide is made up of strip waveguide. The sensitivity of the ring resonator is improved by employing this configuration.

At an end chapter 8 provided with a conclusion and the future scope in this domain. In addition, the brief introduction about the use of porous silicon for resonating structure is discussed. The pores nature of the material is suitable for increasing the light matter interaction hence can be explored in future.

Chapter 2

Biosensor and its Characteristics

2.1 Introduction

A biosensor is a terminology used to represent the innovation in the field of detection of biomaterials. The definition of a Biosensor has modified according to the application, due to an advancement in the technology, terminologies, and method of implementation. For instance, the International Union of Pure and Applied Chemistry (IUPAC) defines a biosensor as a "detecting device that uses specific biochemical reactions mediated by isolated enzymes, immune-systems, tissues, organelles, or whole cells to detect chemical compounds by optical, electrical or thermal signals" [78]. However, M. Cooper said that a biosensor is "a device that uses biological or chemical receptors to detect the analyte (molecules) in a sample" [26]. S.P.J. Higson provides a conceptual definition that it is "a chemical sensing device in which a biologically derived recognition entity is coupled to a transducer, to allow the quantitative development of some complex biochemical parameter" [27].

2.2 Structure of a Biosensor

In a biosensor, the biorecognition layer is the key component as it immobilizes on a surface of a transducer to bind the suitable analyte (or molecule) from a biomaterial (Figure 2.1.1). The biorecognition layer utilizes the biochemical reactions to detect the specific binding analyte. It is a coating of a bioreceptor, which has a capability of selectively detecting the analyte among the various biomolecules present on the biomaterial. The binding capacity or specificity have dependent on the affinity between the bioreceptor and targeted analyte. Hence, only the intended analyte alters the physiochemical properties of the sensor [25,28]. After that, the transduction mechanism of a biosensor controls the process of detecting the physiochemical changes and provide the signals to convert it into human-readable form.

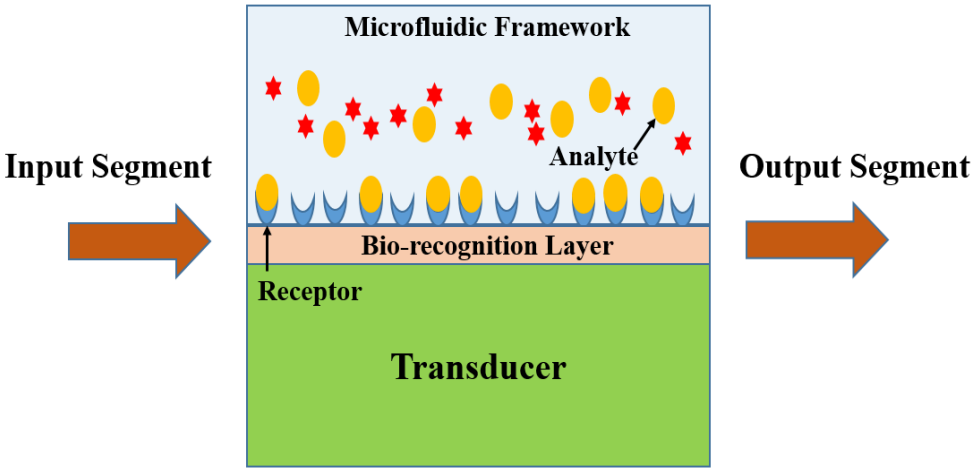

Figure 2.2.1: Biosensor having biorecognition layer

The biorecognition layer deposited on the sensor surface should be highly functional. The biosensing parameters such as sensitivity, limit-of-detection, scalability, uniformity, etc. is dependent on it [3,25,79]. The most commonly used molecules for biorecognition layer are antibodies, single stranded DNA, amino acids, enzymes, proteins, etc. The typical dimension of the antibody is around ~3 nm, and cells may vary from 5-50 µm as shown in Figure 2.2.2. Hence, the biosensor should also be of nanometer to micrometer scale, so that it can efficiently collects the small amount of biomolecule. The development of miniaturized biosensor is due to size constraint of the analyte molecules. The most commonly used bioreceptor and biorecognition mechanism is presented in Figure 2.2.3.

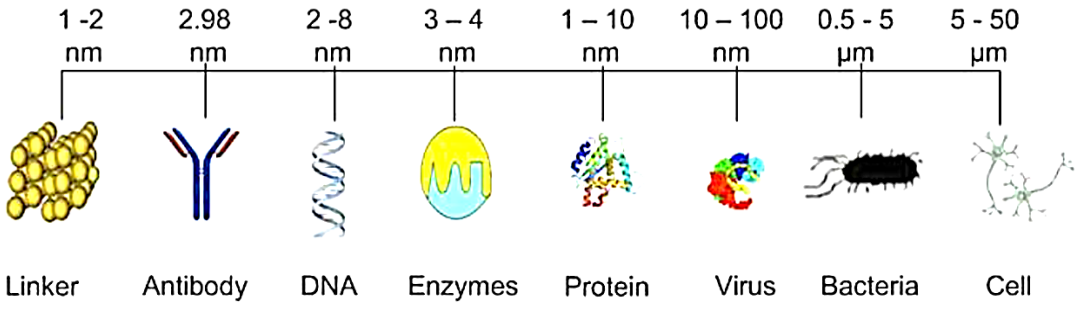

Figure 2.2.2: Dimensions of various biomolecules

Bioreceptor Components	Recognition Mechanism
Enzymes, Proteins	They can catalyze specific chemical reactions. It can be measured by conversion of the analyte into a detectable signal. The detection of the analyte can act as a inhibitor or activator of the reaction.
Antibodies and Antigens	The antigen triggers the immune response of the organism to produce antibodies. Therefore the antibody specifically recognizes the antigens in the sample
DNA Strands	The recognition process is based in the hybridization of complementary DNA strands through double helix.
Cellular Structures	A whole microorganism can be used as a recognition element such as non catalytic receptor.
Biomimetic	The recognition is achieved using genetically engineered molecules, for example, artificial membrane and molecules imprinted polymers imitate the shape of the bioreceptor molecules in order to attract the target molecules.

Figure 2.2.3: Bioreceptor and biorecognition combination [29]

2.3 Biosensors based on Transduction Mechanism

The transducer is the primary component of a sensing device. It provides the quantitative measure of the physical/chemical reaction occurred between the bioreceptor and analyte. In this section, the various transduction mechanism based on electrical, thermal and optical are presented with a brief overview consisting of working principle and recent advancements. Specifically optical transducers have elaborately described here since the further work in this thesis is dependent on it.

2.3.1 Electrochemical Transducers

The Electrochemical transducer works based on the variation of the electrochemical properties such as impedance, voltage, and current. It consists of two electrodes, sensing, and a reference electrode. The biorecognition layer overlays on a surface and is subjected to a biomaterial. The binding event causes the variation in the electrical properties thus performs a detection of the target analyte [28,30]. Various types of electrochemical transducers are amperometric, potentiometric, and conductometric.

2.3.2 Amperometric Transducer

The amperometric biosensor measures the current flow between the electrodes at a constant potential. When analyte bind to a coated enzyme, the electrode undergoes oxidation/reduction process. This binding event modulates the flow of current between the electrodes and that can be quantified to get the concentration of the molecular species [27]. The main feature of the amperometric biosensor is its ability to detect several molecules simultaneously via a coated layer of an enzyme. The practically implemented sensors based on amperometric principle are glucose oxidase-based sensor, a sensor to detect the presence of hydrogen peroxide in the flow systems, Immunoassays, etc. [31,80].

2.3.3 Potentiometric Transducer

The electrodes used for potentiometric transducers becomes inert when an electrochemical reaction occurs. The most likely used electrode materials are gold, silver, platinum, and stainless steel. This transducer utilizes the logarithmic relationship between the induced potential and the targeted ion [33]. It measures the potential between the electrodes at zero current. Therefore, the ability to detect the analyte depends on the selectivity of a membrane layer and the associated generated potential.

The potentiometric transducer has an ability to detect a wider range of detection limits. However, it requires very stable electrodes at the reference end whose performance may not differentiate due to an alteration in the temperature or other environmental factors [30]. The most commonly available potentiometric sensors are based on metal oxide, glass electrodes, and ion selective electrodes.

2.3.4 Conductometric Transducer

The principle behind this transducing method is to find the change in the electrical conductivity of the solution. The ionic strength of the solution gets affected due to the presence of specific enzymes that result in the variation of the conductivity of the solution. It can be used in APA (alkaline phosphate activity) analysis required for the detection of Cholera algae, and utilized for a determination of Creatinine [31,34,68].

2.4 Thermal Transducers

The calorimetric sensor works on the principle of detection of heat, which is generated due to the result of the biochemical reactions between the analyte and the specific enzyme. During the binding event, heat is absorbed (endothermic) or produced (exothermic) which is proportional to the concentration of the molecules involved in the reaction. The most commonly used calorimetric transducer involves the use of the thermistor, which is called as enzyme thermistor (ET). This type of sensor is used in biomedical applications such as observation of enzyme reaction, metabolite analysis, and identification of immobilized biocatalysts [3]. Apart from that, its applications are also found in food industry, environmental monitoring, pharmaceutical industries, etc.

2.5 Mechanical Transducers

In this mechanism, the detection of an analyte is evaluated with mechanical vibrations. Similar to the previous transduction techniques here also the detection of the analyte is dependent on the specificity and functionalization of the bio-receptors. Here we discuss two types of mechanical sensor, which are based on the piezoelectric effect (quartz crystal microbalances (QCM), and microcantilever [35].

The operating principle of the QCM is based on the detection of the resonant frequency, which is generated due to the applied electric field across the piezoelectric crystal. When biomaterial attached to the surface causes to alter the mass of a crystal hence changes the overall oscillating frequency of the QCM. In this technique, the surface wave propagated on the surface of crystal, which is also called as surface-acoustic-waves (SAW). Whenever the SAW encounters the physiochemical changes on the surface, its oscillating frequency becomes reduced. On this basis, the quantitative analysis of the intended biomolecule can be made. However, the disadvantage of this method is the generation of the nonlinearities in the oscillation due to the presence of liquid biomaterial (occurrence of hydration and visco-elasticity phenomena in the QCM) [36,81].

In micro cantilever type of mechanical transducers, the variation in the vibrational frequency is the basis of the detection. The bending occurs whenever mass in the arm increases. It converts the response to a change in the molecular interaction, which takes place on the surface of the cantilever into an observable mechanical response [82]. Detection of a Hepatitis C virus using RNA oligonucleotide is an example of a biosensor utilizing this transduction mechanism [83,84].

2.6 Optical Transducers

Optical transducers for biosensing applications use a variation in optical characteristics for detection purposes. After the interaction of the signal with a biomaterial, alteration in optical properties mainly in the form of light intensity, polarization, resonant wavelength shift, and a change in angular wavelength can be observed, and that can be quantified to detect the presence of an analyte [25]. The optical sensor depends on a change in the effective refractive index of a waveguide. The variations in the optical properties may be occurred due to an attachment of biomaterials on its surface. The attachment of an analyte on the surface change the physiochemical properties of the material cause variation in the velocity of the propagated optical modes [43]. For a higher detection rate, the higher presence of a field component is desired in a biomaterial region.

The optical transducers use an optical waveguide for transmitting signal. Most frequent waveguide configurations are optical fibers, slab/rib/slot, photonic crystal. Different waveguides have their specialty and method of operations; hence based on the applications and measurement of characteristic, various devices can be made. Majority of an optical device for biosensing applications take advantage of the presence of an evanescent field. The evanescent field is the small fraction of a field of an optical mode propagates outside the core region of the waveguide [11,85]. The optical biosensor can be of two types, based on the configuration of a device, and based on a sensing mechanism. Apart from that, it can also be classified based on the detection methodology that is label-based and label-free.

2.6.1 Types of Sensing Mechanism

(a) Raman Spectroscopy

Raman scattering occurs when the interaction between the incident photon and vibrating molecules of the sample becomes inelastic. When an interaction occurs the transfer of energy takes place between photon and molecules of a sample either the photon give energy to molecules or it receives. Hence, on this basis, the Raman spectroscopy came into existence and works on two conditions. The positive change between the energies of incident and scattered photons called as Raman-Stokes scattering, and when the change is negative it is called as Raman-Anti-stokes scattering [86].

The difference in the energy is dependent on the vibrational energy of the molecules. In Raman-stokes scattering, incident photon transfers energy to the molecules present in the sample and force them to go to higher energy states, while returning to an original state these molecules release energy in the form of low energy photons. The difference between the energies is utilized for the prediction of the vibration states of the molecules. Similarly, in Raman to Anti-stokes, the incident photon receives an energy from the vibrational molecule and hence release the photon of high energy or lower wavelength. In both the methods, the wavenumber changes which is responsible for a measurement of vibrational energy of the molecules [86,87].

(b) Fluorescence

In this sensing mechanism, the external light source is required that provide an external energy to an immobilized molecule of the biomaterial. The fluorophores property of the biomolecule causes to absorb the higher energy of short wavelength radiation and then re-emit the photon of lower energy [88]. In this sensing mechanism, fluorescent tags are assembled in either target molecule or the biorecognition layer. The re-emitted photon intensity determines the strength of an analyte and immobilized layer [89].The detailed study is provided in the review paper [89]. It is used in glucose monitoring and DNA sequencing [66,90].

(c) Optical Absorption

It is based on the absorbance capacity of a molecule. When a photon is incident on a molecule part of the energy is absorbed which can be directly proportional to the concentration of the targeted analyte according to the Beer-Lambert law. It states that an optical absorption is directly proportional to the concentration (C) of molecules molecule and an optical path length (L). The biosensor based on this principle works by detecting the intensity of light coupled back to a fiber after interacting with an analyte. The intensity of the light is changes based on Beer-lambert law given as [14],

$$I = I_0 e^{\varepsilon \cdot C \cdot (\Delta L)} \qquad (2.6.1)$$

Where I_0 is the intensity of the incident photons, ε is the molar absorptivity coefficient and ΔL is the optical path length. Through this simple technique, absorption spectra of an intended analyte can be studied. This is used in the development of optical fiber based pH sensor for medical applications [37,38].

(d) Evanescent Field Sensing

In 1980's first time, it is reported that the light-guiding characteristics of the waveguides are affected when it come across changes in the environmental conditions [91]. It became the basis of further evaluation of characteristics for the use of optical waveguides in applications of biochemical, and chemical sensors. Figure 2.6.1, shows the most prominently used planar waveguide configuration.

The light can be guided in a waveguide either as a traveling wave or as a standing wave. Based on applications optical waveguide can be designed. For a biosensor, a biorecognition layer requires being placed on an upper surface of the waveguide core. So the configuration must be designed in such a way that a significant fraction of the field must be present outside the core region that can directly interact with the biorecognition layer.

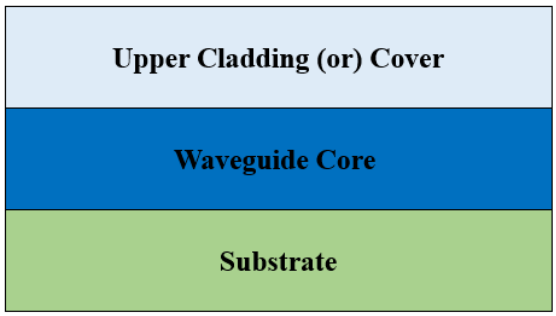

Figure 2.6.1: Planar waveguide configuration having a core, cladding and substrate

The interacted fraction of field changes the overall effective index of the optical mode propagated in a waveguide which is due to the change in the phase velocity of a propagating optical mode [39], and it is given as,

$$v_p = {}^{c}/_{n_{eff}} \qquad (2.6.2)$$

where c is a speed of light in a vacuum, and n_{eff} is the effective index of the waveguide.

From the expression, it is evaluated that the v_p decreases in the presence of the cover materials, and due to the increase in the value of the cover refractive index, v_p decreases. The change in v_p may result in an effective refractive index change (Δn_{eff}).

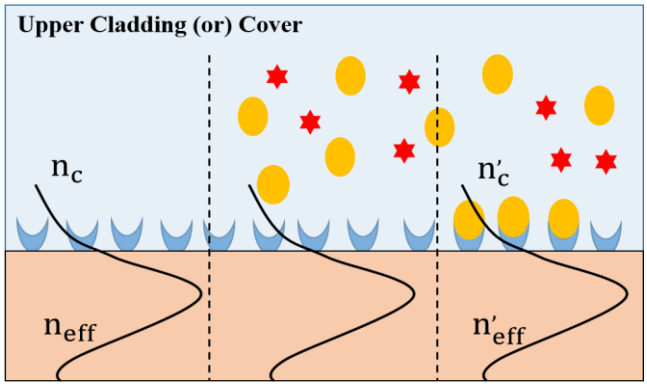

Figure 2.6.2: Evanescent field sensing

The decay of the evanescent field is exponential which can be represented as,

$$E = E_0 e^{-\delta \cdot \frac{2\pi}{\lambda} \cdot \sqrt{n_{eff}^2 - n_c^2}} \quad (2.6.3)$$

Where E_o is the electric field component on the surface, δ is the vertical distance (penetration depth) from the surface. For an operating range of wavelength of 800-1550 nm, the penetration depth is around ~90 - 300 nm [62]. Since the penetration depth is too short, the evanescent field only interact with a biomaterial in a close proximity of the surface. Therefore, this type of sensing mechanism is suitable for biomaterials that directly sticks on the surface such as antibody, DNA and several proteins, which can only attach the targeted molecule and cannot be influenced by the presence of other molecules Figure 2.6.2 [15].

Several optical biosensor configurations utilize this principle. The fundamental idea is to provide the biomaterial in a region where high field intensity is present. Due to the larger field and biomaterial interaction, higher sensitivity can be achieved.

2.7 4 Configurations of Photonic Biosensors

Several types of optical biosensor are already elaborated which are based on geometry and mechanism of working such as interferometer, photonic crystals, surface plasmon resonance, resonating structures based on planar slab waveguide.

2.7.1 Interferometer Photonic Biosensor

The interferometric biosensors are very sensitive to detect a change in refractive index of a biomaterial. Its sensitivity is dependent on a principle of working: The light wave split into two arms and allows propagating in two different optical path length. Hence, out of the two optical path lengths, one will have an optical sample on their surface called as sample arm, while another one will act as a reference arm. The biomaterial sample, above the surface, changes the effective index of the sample arm due to this the phase variation can be observed when both the waves interfere. The intensity of the interfering waves (I) can be a periodic function represented as [40],

$$I = I_R + I_S + 2\sqrt{I_R \cdot I_S}\cos\Delta\varphi \quad (2.7.1)$$

Where I_R and I_S are intensities of the light at reference and sample arm, and $\Delta\varphi$ is periodic phase variation due to the variation in the light intensities. The change in phase is directly dependent on the bio-molecular activity or the change in refractive index of the biomaterial on the surface of the sample arm, and it is proportional to the length of sample arm. Hence, a higher sensitivity can be achieved from the interferometer architecture by making a larger sample length. The most commonly used designs are Mach Zehnder (MZI), the Young Interferometer, the Michelson Interferometer (MI), and Bimodal waveguide interferometer. The brief study of various configurations are provided as follows, the Michelson interferometer based biosensor be discussed in detail in chapter 4.

(a) Mach-Zehnder Interferometer (MZI)

For a MZI configuration two 3-dB Y-junction couplers are required, the light from a waveguide divides from Y-junction into two arm sample arm and a reference arm. The presence of biomaterial in a sample arm alters the characteristics of the optical mode, when both signals from the two arms combine at second Y-junction provides a phase variation as shown in Figure 2.7.1. The expression for phase variation is given as,

$$\Delta\varphi = \frac{2\pi}{\lambda} \cdot L \cdot \Delta n_{eff} \quad (2.7.2)$$

Where L is the length of sample arm at operating wavelength λ, and Δn_{eff} is the change in the effective index of the waveguide.

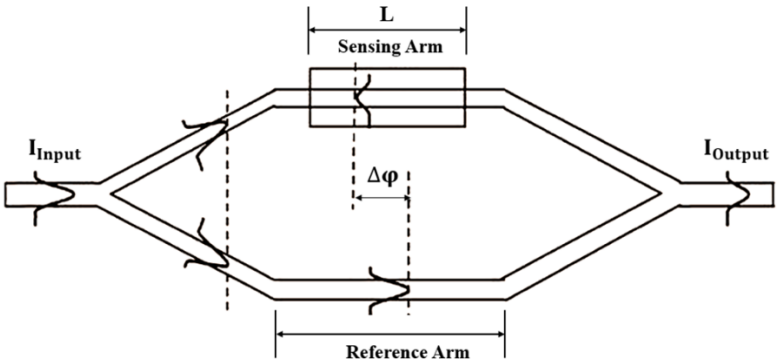

Figure 2.7.1: Balanced Mach Zehnder interferometer having sensing and reference arm

The relationship between I_{Output} and I_{Input} can be represented in terms of cosine function as,

$$I_{Output} = I_{Input} \cdot \cos^2 \frac{\Delta\varphi}{2} = I_{Input} \cdot \cos^2 \frac{\pi \cdot L}{\lambda}(\varphi_S - \varphi_R) \qquad (2.7.3)$$

From the equation (2.7.3), it is easily observable that the sample arm directly increase the sensing ability. The drawback of this configuration is the cosine-based intensity, which provides ambiguous interpretation of the biomaterials due to the periodic fluctuation and the signal is not easy observable near the maxima and minima. The best limit-of-detection achieved with this is of the order of 10^{-6} RIU [21,64].

(b) Young Interferometer

It also uses the 3-dB Y-junction, the light coupled to a Y-junction from a planar waveguide is divided into two waveguide parts: first part consists of the biomaterial and the second part is used for reference purpose. The output from both waveguides are provided into a CCD camera located at a distance L. The CCD camera convert the intensity to an interferogram, and further Fast Fourier Transform (FFT) is applied to it, which provides the quantitative data of biomaterial [45]. From this configuration, minimum achievable limit-of-detection is of the order of 10^{-8} [44,45]. The drawback of YI is the generation of the random vibrations due to distance between the waveguide and a CCD camera, and it is less suitable for LOC devices [44].

(c) Bimodal Waveguide Interferometer

The Bimodal waveguide interferometer works by evaluating the interference of the two-mode of same polarization but different in order such as TE_0 and TE_1. Light first coupled to a waveguide segment that supports only TE_0 mode than after some distance it gets coupled to another waveguide segment that can support two mode TE_0 and TE_1 [92]. When both the modes passes a region of biomaterial the effective index of both the propagating modes gets changed, and that can produce a phase variation which is represented as,

$$\Delta\varphi = \frac{2\pi}{\lambda} \cdot L \cdot \left(n_{eff}(TE_1) - n_{eff}(TE_0)\right) \qquad (2.7.4)$$

where L is the path-length of sensor area.

In this configuration, the light at the output end is provided on two different photo-detectors that may generate current I_0 and I_1. Hence the ratio of $(I_1 - I_0)/(I_1 + I_0)$ is proportional to $\cos(\Delta\varphi \cdot t)$. With this configuration, the relationship between interference and intensity can be neglected and hence the problem of wrong evaluation of biomaterial can be solved. However, this method is still having a drawback of phase uncertainty.

2.7.2 Surface Plasmon Resonance (SPR) based Biosensor

Plasmonic biosensor uses the surface-plasmon-waves for a sensing application. Surface plasmon waves (SPW) are a transverse magnetic (TM) polarization of an optical mode that is generated due to an oscillating nature of the electron charge density at a metal-dielectric boundary [93]. In this way both incident photon and oscillating electron density are involved in the initiation of SPW. Hence, the sensor utilizing it, can easily detect any change in the refractive index of the biomaterial present at the interface of the boundary.

A response of SPR devices provides a sharp dip in the transmission spectra at a point of interaction between photons and SPW. The shift in resonance spectra is utilized for a detection of the presence of an analyte. The parameters responsible for shifting the resonance wavelength are the dielectric constant of materials (metal and substrate), the

angle of incidence, and the operating wavelength. For a label-free detection, the change in the refractive index of a biomaterial causes a change in the position of a resonance dip and an angle of incidence. For excitation of the SPW generally, prisms are used. However, due to the limitations such as bulkier in size, and complex in integration, optical fibers can also be used for excitation [94–96].

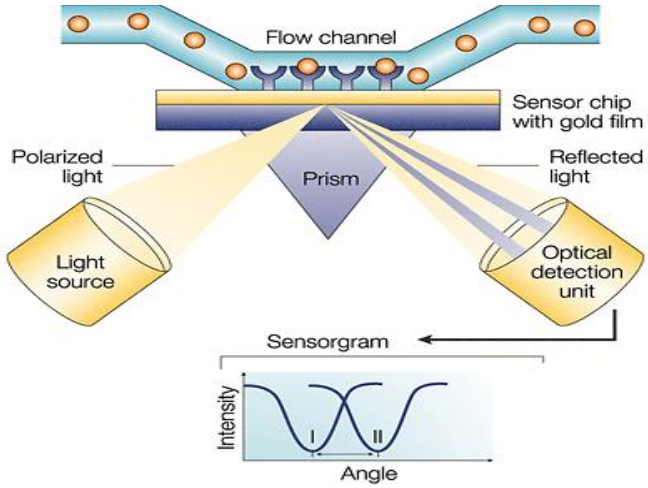

Figure 2.7.2: Surface plasmon resonance based biosensor

Optical fiber-based surface plasmon resonance can be small and requires minute concentration of biomaterial for sensing. The schematic of the surface-plasmon-resonance biosensor is shown in Figure 2.7.2. In which tuned laser source provide the input illumination at the interface between the metal-dielectric and the output signal after reflection is received in the sensogram that plot the fluctuation of the intensity concerning wavelength. Hence, for variation in the refractive index of the biomaterial the incident wavelength or the angle of incidence is changed [71].

The sensing ability is dependent on the metal. Generally, gold, and silver are used. The real part of the dielectric constant is more for gold, which results in higher shift of the resonant wavelength. Similarly, the imaginary part of dielectric function is more for silver hence it is used when curve with narrow width is required for higher accuracy. The chemical stability for Gold is more, silver is more prone to oxidation when it is exposed to air or

water [97]. Other metals such as copper or aluminum are highly oxidized in nature, and they suffers from corrosion, hence are not suitable for sensing applications [93].

2.7.3 Planar Waveguide Resonator based Biosensor

In this thesis, we have considered the silicon-on-insulator platform for designing and studying various architecture. Biosensor based on the resonator device is suitable for providing high sensitivity and precise measurement of the biomaterial. High Q factor and large shift in the resonator wavelength is required for precise detection and highly sensitive biosensor. In last decade resonating biosensor based on ring resonator, disk resonator, Bragg gratings, photonic crystal cavities etc. have been exploited for maximizing its performance. Here we have considered the working of only ring resonators and Bragg gratings based resonators.

(a) Ring Resonators

A ring resonator is a combination of a bus waveguide and a ring waveguide. The high index contrast of SOI platform lower the scattering losses due to bending and allows to make a small diameter ring. A light signal allows passing through a bus waveguide couples into ring waveguide. The signal in the ring interfere constructively causes to resonant in the ring. The resonance condition of ring resonator is provided in equation (2.7.5) as follows,

$$\lambda_{res} = \frac{n_{eff} \cdot L}{m} \tag{2.7.5}$$

Where m is an integer, L is a length of the ring. The typical configuration of the ring resonator have bus and a waveguide.

The evanescent end of the field of a propagating optical mode interact with the ring waveguide and couples its portion of energy into it. The length of the coupling decides the strength of coupling of optical modes. Based on this, ring resonators are divided into two configurations, all-pass and add-drop [98,99]. The schematic of the two configuration with their transmission spectra is shown in Figure 2.7.3.

In an all-pass configuration the fraction κ of the propagated mode couples to the ring and resonant occurs on satisfying the phase matching condition for constructive interference, light then couple-back from ring to a bus waveguide can interfere destructively and it chopped of the portion of the signal from the spectra as shown in Figure 2.7.3.

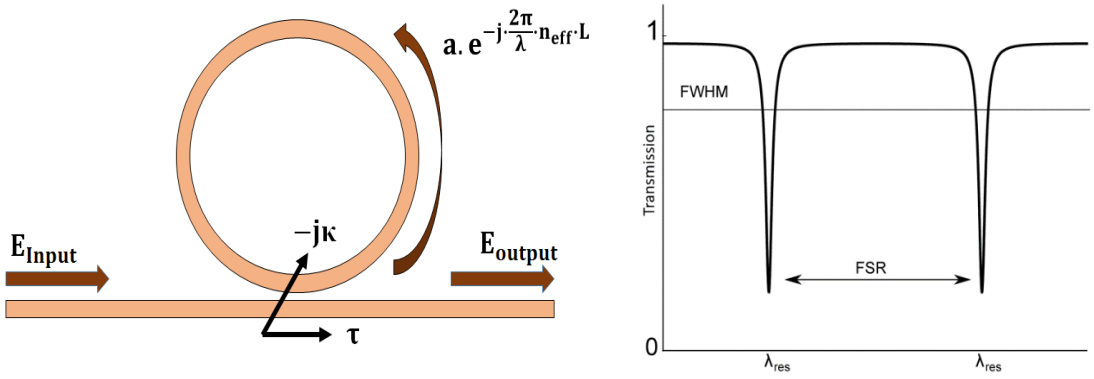

(a)

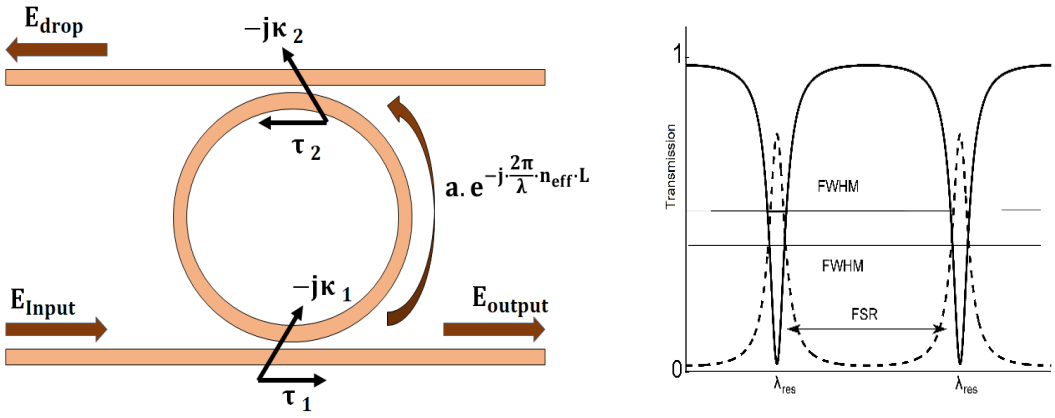

(b)

Figure 2.7.3: (a) All-pass, and (b) add-drop configuration of the ring resonator and their transmission spectra

The equation (2.7.6) provides expression for transmission, which is given as,

$$T_{all-pass} = \frac{a^2 - (2a\tau) \cdot \cos\varphi + \tau^2}{1 - (2a\tau) \cdot \cos\varphi + (a\tau)^2} \quad (2.7.6)$$

Where $\varphi = (2\pi/\lambda) \cdot n_{eff} \cdot L$, a is the reduction in amplitude due to the propagation loss in a waveguide.

Similarly, in an add-drop configuration two bus waveguides are used with a ring waveguide as shown in Figure 2.7.3. The second bus waveguide facilitate to either drop or add an additional signal to a ring resonator. The working is similar to an all-pass configuration except the additional bus waveguide also withdraw fraction of an optical field from the ring waveguide due to its direct coupling it and drop at the drop port. The output port shows a drop in the transmission spectra and its value become maximum under no couple condition.

$$T_{output} = \frac{a^2 {\tau_2}^2 - (2a\tau_1\tau_2) \cdot \cos\varphi + {\tau_1}^2}{1 - (2a\tau_1\tau_2) \cdot \cos\varphi + (a\tau_1\tau_2)^2} \quad (2.7.7)$$

$$T_{drop} = \frac{a \cdot (1 - \tau_1^2) \cdot (1 - \tau_2^2)}{1 - (2a\tau_1\tau_2) \cdot \cos\varphi + (a\tau_1\tau_2)^2} \quad (2.7.8)$$

Where $\varphi = (2\pi/\lambda) \cdot n_{eff} \cdot L$.

The resonating condition and the transmission spectra depends on the value of the effective refractive index (n_{eff}). When the resonator is supplied with a biomaterial, the specific analyte binds the biorecognition layer causes the change in the refractive index in the upper cladding region of the resonator. This change in the refractive index of the upper cladding alters the effective index of the waveguide and subsequently changes the resonant condition of the device. The shift in the resonant wavelength corresponding to a change in refractive index through the binding event can be expressed as,

$$\Delta\lambda = \frac{\Delta n_{eff} \cdot \lambda_{res}}{n_g} \quad (2.7.9)$$

Where $\Delta\lambda$ is a resonant wavelength, n_g is the group index and Δn_{eff} is the change in effective index of a waveguide. The group index represent the impact of dispersion and can be written as, $n_g = n_{eff} - \lambda \frac{dn_{eff}}{d\lambda}$. Since the resonant wavelength shift is directly dependent on the Δn_{eff}, larger value leads to a higher sensitivity. In a conventional waveguide based resonator, only evanescent field interacts with the biomaterial. The low fraction of the evanescent field does not provide high sensitivity.

The increase in the light matter interaction can be acquired by two methods, either to use a slot waveguide or an ultra-thin waveguide. The slot waveguide based ring resonator can significantly increase the Δn_{eff} due to its ability to confine light in the low refractive index slot region. However, it is fond of higher propagation losses that make impact the precise detection of an analyte [51,100–102]. The use of ultra-thin waveguide is most promising method for increasing the field concentration on the surface. In the [16] ultra-thin waveguide of 90 nm thickness is considered for devising a ring resonator. The reported propagation loss is around 2.3 dB/cm.

(b) Bragg Grating Resonator based Biosensor

A Bragg grating is a configuration that comprises of a periodic alteration of the refractive indices. The change in the periodic refractive index creates a phase shift. This phase shift is high at a specific wavelength called as a Bragg wavelength. All wavelength in the close vicinity of the Bragg wavelength are highly reflective. The constructive reflection creates a stop band region at the transmission spectra. Several methods are presented in a literature for their implementation. Most profoundly used architecture utilizes the optical fiber and planar slab waveguide. Apart from the stop band region, it also provides a sharp resonant band in the stop band region because of insertion of the phase shift cavity. The resonance condition and stop band region both are dependent on the effective index of the propagating optical mode. The shift of resonance wavelength occurs on account of alteration of the

effective index. By using this phenomenon, several biosensors are proposed. The resonating band can be architecture to have a high Q factor, and a high sensitivity. The high Q factor enable us to detect the small possible change in the refractive index of the biomaterial, hence we can conferred that it can be used to lower the limit of detection [48,61,85,103]. The more detailed study of the mode propagation and other characteristics are discussed in detail in chapter 3.

2.8 Labelled and Label Free Biosensor

Label based identity is the most widely used technique for biosensing applications. This method requires an agent with specific chemical properties such as fluorescence, radioactive, and bio-affinity for proteins [44]. The materials used for radioactive tags are antibodies, nucleic acids, magnetic pearls, enzymes, dyes etc. Tests are selected based on their targeted coupling capability so that they can be bind with targeted biomolecules. Binding can be in the form of covalent bonds. Fluorescent tags are used most often between different label based search technologies.

Fluorescence is a property of the material to absorb the radiation energy of a wavelength and then releases the energy at a longer wavelength. The requirement of fluorophores particles is to be highly selective so that it can bind the desired analyte from a group of molecules. When light falls on the fluorophores particles, then it reaches to an excitation state and when the signal returns to normal condition, the signal releases the energy detected by the photodetector. The prediction of the presence of an analyte is made through the quantitative analysis of the detected labels. This detection methodology is highly sensitive and, it can sense up to a single molecule. However, the recombination between the biomaterial and fluorescent materials can cause a severe change in the characteristics of the biomaterial, which sometimes makes this method unstable. The intensity of the radiated photon is very low and have the short lifetime. Hence it requires very high-quality equipment. Besides, it requires expertise in handling the particular process during binding event make this approach laborious and complicated [44,45,87].

Whereas in Label free detection, an immobilized bioreceptor is attached to the sensor surface that only binds the particular analyte. The biorecognition process (binding between analyte and bioreceptor) changes the surface properties of the sensor, which can be characterized to detect the presence of a targeted biomaterial [25]. The bioreceptor is usually a protein (or enzyme) capable of binding a targeted molecule or an analyte. Hence, the label free detection does not require any secondary reactant, it also eliminate the problem of the alteration of surface chemistry due to the presence of a radioactive material [28,79]. Moreover, simplified binding kinetics can provide an accurate quantitative analysis of the detected biomaterial.

2.9 Characteristics of Biosensor

Biosensors are an integral part of the various sub units like drug detection, healthcare monitoring, disease detection etc. To determine the effectiveness of the sensor various performance parameters need to considered. Here we have only discussed specific parameters, which are usually considered for the evaluation of biosensor.

2.9.1 Sensitivity

The sensitivity is the representation of the coupling of the electromagnetic waves with the biomaterial present on the surface. It specifically depend on the design of the sensor that allows proportion of the electric field outside the core region of the waveguide. Various factors affecting the electric field fraction such as penetration-depth of an evanescent field, waveguide width and thickness, material of core and cladding region, and geometric uncertainty [14].

The sensitivity is the fundamental parameter of the sensing device. It is a derived from the signal strength of a transduction mechanism corresponding to an alteration in the change in the physicochemical characteristics of an analyte. For example sensitivity for resonating photonic biosensor is the ratio of change in the resonant wavelength and a change in the refractive index of an analyte ($\Delta\lambda/\Delta n_c$) [104].

The refractive index sensitivity of the sensor is given as,

$$S = \frac{\Delta\lambda_{res}}{\Delta n_c} = \frac{\lambda_{res}}{n_g}\frac{dn_{eff}}{dn_c} \quad (2.9.1)$$

Where n_g is the group index and λ_{res} is the resonant wavelength. The following depiction has been made from the equation (2.7.1).

(a) Δn_c change in the refractive index of the upper cladding region directly changes S.

(b) The resonator sensitivity is significantly affected by the dispersion of the waveguide. The effect of the dispersion is included through the consideration group index n_g. The value of n_g also varies on changing the operating wavelength.

(c) The value of S directly proportional to dn_{eff}/dn_c hence the index change causes alteration in the mode.

2.9.2 Homogenous Sensing

Homogenous sensing refers to a change in the biomaterial (fluid form or gaseous state) present over the surface of a waveguide. The change in a refractive index of a biomaterial (upper cladding region) also changes the overall effective index of the propagated modal field of a waveguide and shifts the resonant wavelength. The homogenous sensing can be numerically formulated as a ratio of change in effective index of a waveguide and change in refractive index of a biomaterial ($\Delta n_{eff}/\Delta n_c$). Figure 2.9.1 represent the schematic diagram of homogenous sensing [13].

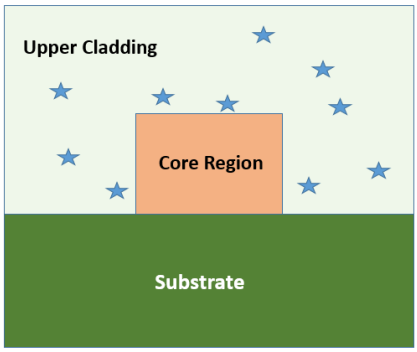

Figure 2.9.1: Homogenous sensing

2.9.3 Detection Limit (LOD)

For a transducer to respond, minimal change in the refractive index of the biomaterial is required. The LOD for photonic biosensor is an intrinsic capability of the sensing device which specifically dependent on its architecture.

A LOD for configuration of planar waveguide is characterize by considering the effect of noise or random errors occurred in the sensing operation.

$$\mathrm{LOD} = \frac{3\sigma}{S} \tag{2.9.2}$$

Where σ is the minimum-resolvable signal and S is the sensitivity. The LOD can be lower by increasing the sensitivity or decreasing the noise in the sensor. The most common factor for inclusion of noise are temperature fluctuations and the thermal expansion in different regions of the sensing unit [11].

Whereas for resonating type of a biosensor the detection limit is dependent on both sensitivity and quality factor (Q-factor). The high Q factor of the resonant signal easily resolve the smallest possible change in the refractive index of a biomaterial [104]. The expression for LOD comprising of S and Q is given as,

$$\mathrm{LOD} = \frac{1}{Q \cdot S} \tag{2.9.3}$$

The LOD can also be expressed as inversely proportional to $\mathrm{dn_{eff}}/\mathrm{dn_c}$, the expression is,

$$\mathrm{LOD} = \frac{\Delta\lambda_{\min}}{(2 \cdot \Lambda)\left(\frac{\mathrm{dn_{eff}}}{\mathrm{dn_c}}\right)} \tag{2.9.4}$$

Where $\Delta\lambda_{min}$ is the one-fifteenth of the minimum $\Delta\lambda_{-3dB}$ (Full width at half maximum) [46].

2.10 Lab on a Chip Device (LOC)

The LOC is a Micro-Total-Analysis-System (μTAS), this concept was introduced in 1980, which was presented as a system with a laboratory function on a chip such as a sample preparation, stabilization of analyzer, filtering, signal analysis, etc. Likewise, the development of electronic computation capability provided us with compact high-performance handheld devices [6]. It is expected that the similar evolution of the photonic technologies would replace the traditional method of laboratory testing with high performance portable LOC device.

The schematic is shown in Figure 2.10.1 where complete chip consists of several subsystems. The main two fundamental block of the LOC are microfluidic framework and the photonic sensor. The microfluidic framework allows passing the biomaterial to a photonic sensor after being preprocessed through the reagents, mixing, filtering, pumping etc. The biomaterial then passes on to a photonic biosensing system. The primary purpose of it is to detect the presence of an analyte precisely [105,106]. Both of these units are in the intense research for improving the performance of an overall LOC system.

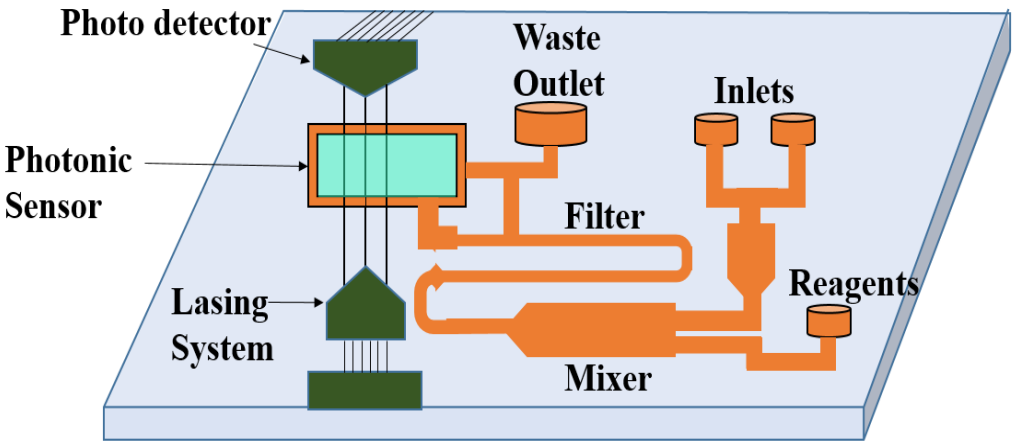

Figure 2.10.1: Lab-on-chip configuration

The LOC devices have all units on the chips, presently available sensors such as pregnancy or glucose detector, uses an immobilized bio-receptor is for a detection of an analyte cannot be considered as LOC devices [107]. In such a biosensors target analyte is only required to

stick on a provided micro assays. These point-of-care sensory devices are used for initial prediction and testing. However, these devices are lacking with the various functionalities that are required to provide human readable observations and the preciseness in evaluation of the disease or an analyte. The other advantages of the LOC devices are compactness, robustness, requires lower sample concentration, provide faster measurement and user friendly.

2.11 Summary

In this chapter, the fundamental principles behind the most important biosensing devices have been discussed with their working principles and their sensing mechanism. The biorecognition layer is a backbone of the biosensor, it appears on the surface of the sensor, and it is responsible for binding the targeted analyte from the group of other biomolecules. Various biological receptors such as enzymes, antibodies, DNA strands, etc. have also been discussed for different biorecognition processes. The biosensor is an integral part of our society, to date, many biosensors based on various transduction methods are available each has their capability and mechanism of working, and almost all utilize the biorecognition method for binding an analyte onto it.

The most likely transduction mechanism is based on advancements in optical or photonic technologies. From Raman Spectroscopy to an evanescent field sensing, many photonic transducing techniques have been used to develop an efficient and accurate biosensor. Especially the evanescent field-based biosensor is the fundamental principle behind many configurations of photonic biosensors. Evanescent field sensor makes use of an interaction between the fraction of field present on the surface and the biomaterial. For maximizing, the sensitivity higher interaction is desirable. Comparative studies between sensors require general biosensing attributes that extend in detail. In the end, potential capacity lab-on-chip sensing units have also discussed.

Chapter 3

Theory and Mathematical Modeling

Photonic structures can be analyzed through analytical and simulation modeling. The analytical modeling is computationally more efficient to implement, since it does not requires the lots of resources [104]. The method such as Beam propagation method (BPM) and finite element method (FEM) requires dividing the complete structure into several smaller regions called mesh. Fine mesh grids are required for accurate results. Also the BPM is a unidirectional method and requires a paraxial (small angle) ray approximation [108]. The FEM is a bidirectional approach that converts a field into ordinary differential equations, which can be numerically computed through finite-difference-time-domain (FDTD) method or a transfer matrix method (TMM). The methods FDTD also requires the meshing of the overall structure, hence the approach is computationally demanding [109]. However, the TMM method divides the complete structure into sub-layers, the analytical equivalent of each divided layers is represented by a matrix, and the overall response of the device requires the matrix multiplications of all the sub-layers [42]. In this chapter, we are representing various mathematical methods to evaluate the performance of photonic devices.

3.1 Optical Modes

The commonly used configuration of the optical waveguides consists of core and cladding grown on a substrate. The core of a waveguide is of high refractive index (n_h) material in comparison to a cladding material (n_l), refractive index of the substrate (n_s) can be in between $n_l < n_s < n_h$, and cover region is n_c.

The schematic diagram of the strip and rib waveguide is shown in Figure 3.1.1. The two-dimensional structure allows the modal confinement in x and y direction. The signal projected at z = 0 is propagated along the z-direction, on fulfilling the total internal

reflection (TIR) condition. The TIR requires two conditions into consideration, first, the value of core refractive index must be higher than that of the cladding, and secondly the launch angle should be adjusted for confinement of the field at the core of a waveguide.

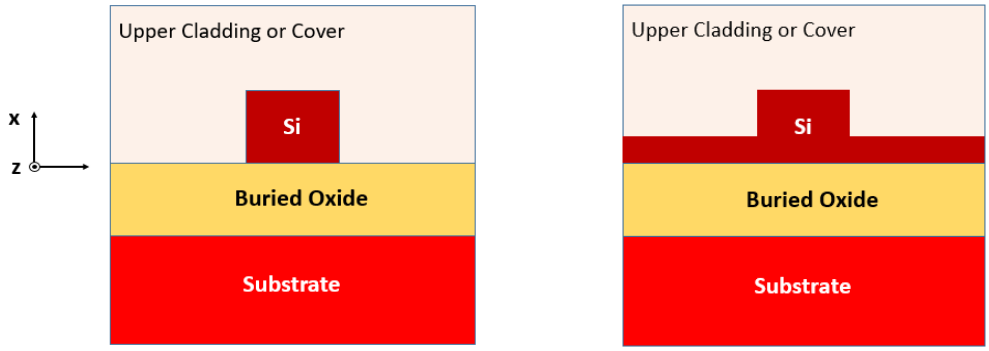

Figure 3.1.1: Planar strip and rib waveguide

The waveguide have three types of modes that depends on the launch of the field.

(a) The propagation constant ($\beta = k \cdot n_{eff}$) for a guided mode lie in between n_h and n_l ($n_l < n_{eff} < n_h$).

(b) When the modes $n_{eff} > n_c$, and $n_{eff} < n_l$ condition results in a mode propagation in transverse direction in the substrate called as substrate radiation mode [110].

(c) Finally when $n_{eff} < n_c$ modes becomes oscillatory in all the regions and their major portion lies in cladding hence called as cladding radiation mode.

In some cases, evanescent field may exist, in which a propagated mode have purely imaginary effective index.

To get a more insight of the optical modes in a planar waveguide structure, we have considered a linear waveguide having an isotropic permittivity constant, which is surrounded by a cover region. The electric and magnetic field for such a configuration is given as [111]

$$E_m = E_m(x, y) \cdot e^{-i \cdot (\omega t - \beta_m z)} \qquad (3.1.1)$$

$$H_m = H_m(x, y) \cdot e^{-i\cdot(\omega t - \beta_m z)}$$

where m is the mode number, $E_m(x,y)$ and $H_m(x,y)$ are the electric and magnetic components of the optical mode, β_m is the propagation constant of the guided optical mode.

From the modal propagation constant the effective index of the mode can be deduced as, $\beta_m = \kappa \cdot neff,\ neff = (\beta_m \cdot \lambda)/(2\pi)$.

We have assumed that the modal confinement in two dimensions (x and y), hence it can have two mode numbers p and q for a propagating guided field. For the evaluation of the field components in the waveguide we need to consider the fundamental Maxwell's equation which are given as,

$$\begin{aligned} \nabla \times E &= -\mu_0 \frac{dH}{dt} \\ \nabla \times H &= \varepsilon \frac{dE}{dt} \\ \nabla \cdot D &= \rho \\ \nabla \cdot B &= 0 \end{aligned} \qquad (3.1.2)$$

The E and H are described in equation (1), the various field components can be,

$$\begin{aligned} \frac{dE_z}{dy} &= i\beta E_y + i\omega\mu_0 H_x \\ \frac{dE_z}{dx} &= i\beta E_x - i\omega\mu_0 H_y \\ \frac{dE_y}{dx} - \frac{dE_x}{dy} &= i\omega\mu_0 H_z \\ \frac{dH_z}{dy} &= i\beta H_y - i\omega\varepsilon E_x \\ \frac{dH_z}{dx} &= i\beta H_x + i\omega\varepsilon E_y \end{aligned} \qquad (3.1.3)$$

$$\frac{dH_z}{dx} - \frac{dH_x}{dy} = -i\omega\varepsilon E_z$$

Through the longitudinal component, the transverse component of the electric and magnetic field can be expressed as,

$$(\kappa^2 - \beta^2) \cdot E_x = i\beta \frac{dE_z}{dx} + i\omega\mu_0 \frac{dH_z}{dy}$$

$$(\kappa^2 - \beta^2) \cdot E_y = i\beta \frac{dE_z}{dy} - i\omega\mu_0 \frac{dH_z}{dx}$$

$$(\kappa^2 - \beta^2) \cdot H_x = i\beta \frac{dH_z}{dx} - i\omega\varepsilon \frac{dE_z}{dy}$$

$$(\kappa^2 - \beta^2) \cdot H_y = i\beta \frac{dH_z}{dy} + i\omega\varepsilon \frac{dE_z}{dx} \qquad (3.1.4)$$

Where $\kappa^2 = \omega^2\mu_0\varepsilon$, based on equation (3.1.4) it can also be depicted that the computation of the longitudinal modes facilitate the computation of the transverse modes. The classification of the transverse modes for various conditions are as follows,

(a) $E_z = 0$, TE (Transverse Electric) mode,

(b) $H_z = 0$, TM (Transverse Magnetic) mode,

(c) $E_z = H_z = 0$, TEM (Transverse Electric and Magnetic) mode, and

(d) $E_z \neq H_z \neq 0$, Hybrid modes.

Since the work in this thesis is mostly concentrated on the Transverse electric (TE) mode, we further evaluates the precise expression of electric and magnetic field components,

$$\frac{d^2E_y}{dx^2} + (\kappa^2 - \beta^2) \cdot E_y = 0 \qquad (3.1.5)$$

Where $\kappa = \omega \cdot n(x, y)/c$.

From the evaluation of the Ey, the depicted values of Hx and Hz are,

$$H_x = \frac{-\beta}{\omega\mu_0} E_y$$

$$H_z = \frac{1}{\omega\mu_0} \frac{dE_y}{dx} \qquad (3.1.6)$$

Similarly calculation for TM mode can be performed. For an analysis of the complex waveguide structure, other semi analytical methods can also be used such as EIM (effective index method) and ADI (alternate-direction implicit).

3.2 Modes of Strip Waveguide (and Cutoff Condition)

From the previous section, it is known that the TE mode comprises of three field components for the propagated optical modes, which are E_y, H_x and H_z. The components of the magenetic field (H_x and H_z) are dependent on the E_y.

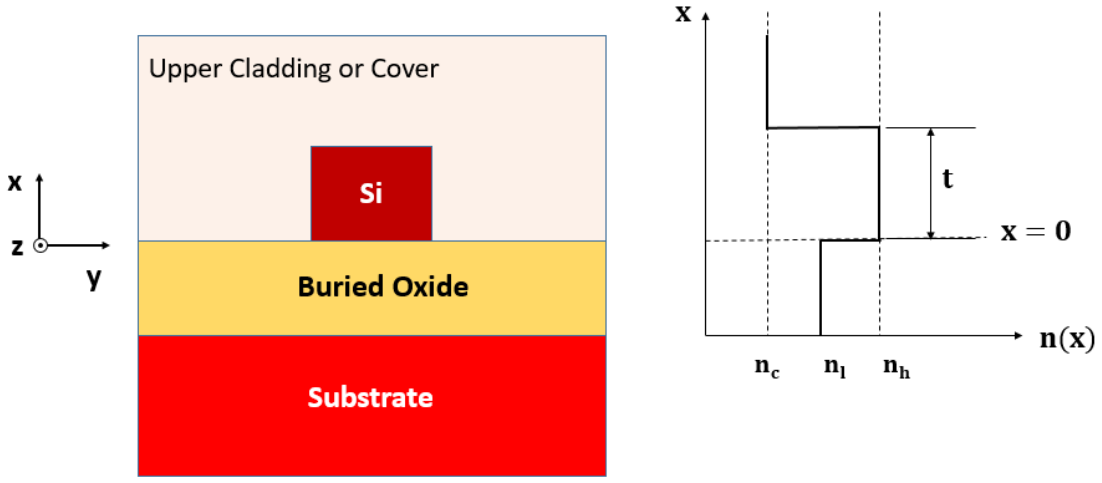

Figure 3.2.1:Strip waveguide with the refractive index profile

The schematic of the strip waveguide with the refractive index profile is shown in Figure 3.2.1). The expression mentioned in equation (3.1.4) must be continuous at an interface x = 0 and t by checking the continuity of E_y and $^{dE_y}/_{dx}$. Since we have already mentioned

that, the oscillation produced at the different region of the waveguide must have different propagations constants. At the core region, the confinement of the mode is at the core region hence the propagation constant (γ_h) represented as, $\gamma_h = \sqrt{\kappa^2 n_h^2 - \beta^2}$ derives the expression of Ey,

$$E_y(x) = E_h \cdot \cos(\gamma_h x + \varphi)$$

$$\frac{dE_y}{dx} = -(\gamma_h \cdot E_h) \cdot \sin(\gamma_h x + \varphi) \qquad (3.2.1)$$

Similarly the oscillation at the substrate and the cladding regions can also be expressed, the propagation constants at substrate is γ_s, and cladding γ_c. The expressions are,

$$\gamma_s = \sqrt{\beta^2 - \kappa^2 \cdot n_s^2}$$

$$\gamma_c = \sqrt{\beta^2 - \kappa^2 \cdot n_c^2} \qquad (3.2.2)$$

Based on the propagations constants mentioned in equation (3.2.2), has utilized for an evaluation of the electric field components,

The field component at substrate region are.

$$E_y(x) = E_s \cdot e^{\gamma_s (x-t)}$$

$$\frac{dE_y}{dx} = (\gamma_s \cdot E_s) \cdot e^{\gamma_s (x-t)} \qquad (3.2.3)$$

The field components at the cladding region are,

$$E_y(x) = E_c \cdot e^{\gamma_c \cdot x}$$

$$\frac{dE_y}{dx} = (\gamma_c \cdot E_c) \cdot e^{\gamma_c \cdot x} \qquad (3.2.4)$$

The electric field profile of a TE mode is written as [111],

$$E_y(x) = f(x)$$
$$= \begin{cases} E_c e^{-\gamma_c x}, & x > t \\ E_c\left[\cos\gamma_h(x-t) - \frac{\gamma_c}{\gamma_h}\sin\gamma_h(x-t)\right], & 0 \le x \le t \\ E_c\left[\cos(\gamma_h t) - \frac{\gamma_c}{\gamma_h}\sin(\gamma_h t)\right] \cdot e^{\gamma_s x}, & x < 0 \end{cases} \quad (3.2.5)$$

By equating the components of the field at position of x provides the value of constants.

At x = 0,

$$E_h \cdot \cos(-\gamma_h \cdot t + \varphi) = E_s$$
$$-\gamma_h E_h \cdot \sin(-\gamma_h \cdot t + \varphi) = \gamma_s \cdot E_s \quad (3.2.6)$$

By combining equation (3.2.6),

$$\tan(-\gamma_h \cdot t + \varphi) = -\left(\gamma_s/\gamma_h\right) \quad (3.2.7)$$

Simlarly at x = t,

$$E_h \cos\varphi = E_c$$
$$(\gamma_h E_h) \cdot \sin\varphi = \gamma_c \cdot E_c \quad (3.2.8)$$

From equations (3.2.6) and (3.2.7), we get,

$$\tan(\varphi) = \frac{\gamma_c}{\gamma_h} \quad (3.2.9)$$

By combining equations (3.2.7) and (3.2.9), the characteristics equation of TE mode can be evaluated as,

$$\gamma_h \cdot t = \tan^{-1}\left(\frac{\gamma_s}{\gamma_h}\right) + \tan^{-1}\left(\frac{\gamma_c}{\gamma_h}\right) + p \cdot \pi \tag{3.2.10}$$

The deduced parameters can be further simplify through a method provided by Kogelnik and Ramaswamy [112],

The characteristic equation of the transverse electric mode (TE) can be represented as,

$$V\sqrt{1-b} = \tan^{-1}\sqrt{\frac{a+b}{1-b}} + \tan^{-1}\sqrt{\frac{b}{1-b}} + p \cdot \pi \tag{3.2.11}$$

where $V = \kappa \cdot t\sqrt{n_h^2 - n_s^2}$, $a = \frac{n_s^2 - n_c^2}{n_h^2 - n_s^2}$ and $b = \frac{n_{eff}^2 - n_s^2}{n_h^2 - n_s^2}$.

From equation (3.2.10), cutoff condition can be implied which shows the transformative value of V, when a mode becomes substrate radiative.

$$V_p^c = \tan^{-1}\sqrt{a} + p \cdot \pi \tag{3.2.12}$$

$$\lambda_p^c = \frac{2\pi}{V_p}\sqrt{n_h^2 - n_s^2} \tag{3.2.13}$$

The number of guided modes TE modes at an operating value of wavelengths are,

$$N = \frac{V}{\pi} - \frac{1}{\pi}\tan^{-1}\sqrt{a} \tag{3.2.14}$$

3.3 Modes of Slot Waveguide

The complete multislot waveguide is divided into several layers. The schematic of the single slot waveguide is shown in Figure 3.3.1. Before describing the solution for multislot waveguide, we present here the generalized solution of each layer by considering single slot waveguide (Figure 3.3.1).

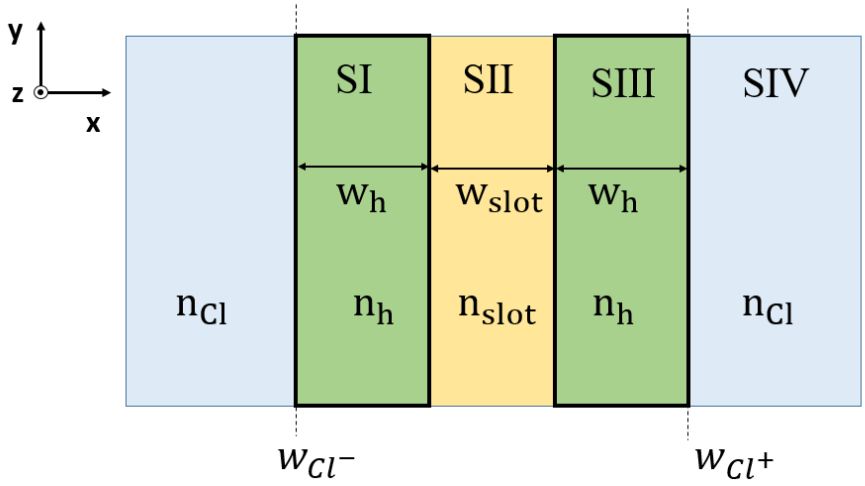

Figure 3.3.1: Layered structure of a waveguide

The structure is divided into several waveguide segments represented as SI, SII, SIII, and SIV. The width w_{slot} and w_h representing the width of slot layer (SII) and width of high index layer (SI and SIII). The solution of each segment can be find by solving the Helmholtz equation given as,

$$f(x) = \begin{cases} \frac{d^2E_x}{dx^2} - \gamma_{slot}E_x = 0, & x \in \text{Slot} \\ \frac{d^2E_x}{dx^2} + \gamma_h^2 E_x = 0, & x \in H \\ \frac{d^2E_x}{dx^2} - \gamma_{Cl}^2 E_x = 0, & x \in Cl\ (Cl^- \text{ or } Cl^+) \end{cases} \quad (3.3.1)$$

where γ_{slot}, γ_h, and γ_{Cl} represents the propagation constant of the slot, high refractive index and cladding regions.

The solutions of each sub layer is,

$$E_x(x) = \begin{cases} e^{\gamma_{Cl}(x - W_{Cl^-})}, & x \in Cl^- \\ A_{slot}\cosh[\gamma_{slot}(x - W_{slot})] + B_{slot}\sinh[\gamma_{slot}(x - W_{slot})], & x \in Slot \\ A_h\cos[\gamma_h(x - W_h)] + B_h\sin[\gamma_h(x - W_h)], & x \in H \\ A_{Cl}e^{-\gamma_{Cl}(x - W_{Cl^+})}, & x \in Cl^+ \end{cases} \quad (3.3.2)$$

where Cl^- and Cl^+ are the extreme edges of the waveguide.

The expression for coefficients at waveguide segment SI,

$$\begin{pmatrix} A_h \\ B_h \end{pmatrix} = \begin{pmatrix} n_{Cl}^2 / n_h^2 \\ \gamma_{Cl} / \gamma_h \end{pmatrix} \quad (3.3.3)$$

The coefficient at waveguide segment (SII), are evaluated such that there values can be dependent on the segment SI,

$$\begin{pmatrix} A_{slot} \\ B_{slot} \end{pmatrix} = M_{h-slot} \begin{pmatrix} A_h \\ B_h \end{pmatrix} \quad (3.3.4)$$

where, $M_{h-slot} = \begin{pmatrix} \frac{n_h^2}{n_{slot}^2}\cos(\gamma_h w_h) & \frac{n_h^2}{n_{slot}^2}\sin(\gamma_h w_h) \\ -\frac{\gamma_h}{\gamma_{slot}}\sin(\gamma_h w_h) & \frac{\gamma_h}{\gamma_{slot}}\cos(\gamma_h w_h) \end{pmatrix}$

Similarly the coefficients at the waveguide segments SIII and SIV are,

$$\begin{pmatrix} A_h \\ B_h \end{pmatrix} = M_{slot-h} \begin{pmatrix} A_s \\ B_s \end{pmatrix} \quad (3.3.5)$$

where, $M_{slot-h} = \begin{pmatrix} \frac{n_{slot}^2}{n_h^2}\cosh(\gamma_{slot} w_{slot}) & \frac{n_{slot}^2}{n_h^2}\sinh(\gamma_{slot} w_{slot}) \\ \frac{\gamma_{slot}}{\gamma_h}\sinh(\gamma_{slot} w_{slot}) & \frac{\gamma_s}{\gamma_h}\cosh(\gamma_{slot} w_{slot}) \end{pmatrix}$

and,

$$\begin{pmatrix} A_{Cl} \\ A'_{Cl} \end{pmatrix} = M_{h-Cl} \begin{pmatrix} A_h \\ B_h \end{pmatrix} \tag{3.3.6}$$

where, $M_{h-Cl} = \begin{pmatrix} \frac{n_h^2}{n_{Cl}^2}\cos(\gamma_h w_h) & \frac{n_h^2}{n_{Cl}^2}\sin(\gamma_h w_h) \\ \frac{\gamma_h}{\gamma_{Cl}}\sin(\gamma_h w_h) & -\frac{\gamma_h}{\gamma_{Cl}}\cos(\gamma_h w_h) \end{pmatrix}$

At the end, the Eigen solution of the slot waveguide structure can be evaluated by equating, $A_{Cl} = A'_{Cl}$.

This method can be implemented for multislot waveguide. The important point of consideration is that, the waveguide should contain a well-defined rectangular geometry and slot size should be small enough to confine light in it.

3.4 Generalized Transfer Matrix Method (TMM)

The transfer matrix method (TMM) is utilized for evaluating the response of the multilayered structure. This approach is more efficient and is computationally easy to implement. The TMM divide the complete structure into multiple layers, then the evaluation of the reflectance and transmittance is performed at an interface, and finally, it is represented in the form of a matrix. The complete structure can be described concerning the matrix multiplication of all the layers. This method can also be applied to the structure having varied parameters [80].

The method is specifically dependent on the continuity of electric field (E and derivatives) at an interface.

At interface S1

$$E_{S1} = E_{iS1} + E_{rS1} = E_{tS1} + E'_{rS2} \tag{3.4.1}$$

$$H_{S1} = \frac{1}{Z_1}(E_{iS1} - E_{rS1}) = \frac{1}{Z_1}(E_{tS1} - E'_{rS2})$$

where $Z_1 = \sqrt{\frac{\mu_0}{\epsilon_0}} \cdot \frac{1}{\sqrt{\epsilon_r}} = \sqrt{\frac{\mu_0}{\epsilon_0}} \cdot \frac{1}{n_1}$, $Z_2 = \sqrt{\frac{\mu_0}{\epsilon_0}} \cdot \frac{1}{n_2}$, and $Z_3 = \sqrt{\frac{\mu_0}{\epsilon_0}} \cdot \frac{1}{n_1}$

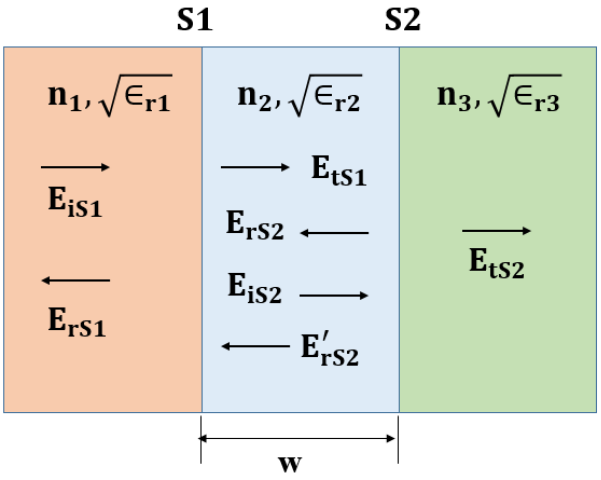

Figure 3.4.1: Layered structure having reflectance and transmittance

In the interface S2,

$$E_{S2} = E_{iS2} + E_{rS2} = E_{tS2}$$

$$H_{S2} = \frac{1}{Z_2}(E_{iS2} - E_{rS2}) = \frac{1}{Z_3}E_{tS2} \qquad (3.4.2)$$

A signal experiences a phase shift, after passing through a layer of width w, The phase acquire by the electric field is,

$$E_{iS2} = E_{ts1}e^{-\kappa_0 \cdot n_2 \cdot w}$$

$$E_{rS2} = E'_{rs2}e^{-\kappa_0 \cdot n_2 \cdot w} \qquad (3.4.3)$$

After substituting the value of equation (3.4.3) in equation (3.4.2)

$$E_{S2} = E_{tS1} e^{-\kappa_0 \cdot n_2 \cdot w} + E'_{rs2} e^{-\kappa_0 \cdot n_2 \cdot w}$$

$$H_{S2} = \frac{1}{Z_2} (E_{tS1} e^{-\kappa_0 \cdot n_2 \cdot w} - E'_{rs2} e^{-\kappa_0 \cdot n_2 \cdot w}) \quad (3.4.4)$$

By substituting equation (3.4.4) in equation (3.4.1)

$$E_{S1} = E_{S2} \cos \kappa_0 n_1 w + i \cdot (Z_2 \cdot H_{S2} \cdot \sin \kappa_0 n_2 w)$$

$$H_{S1} = \frac{E_{S2}}{Z_2} \cdot (i \cdot \sin \kappa_0 n_2 w) + H_{S2} \cdot \cos \kappa_0 n_2 w \quad (3.4.5)$$

The equivalent matrix representing equation (3.4.5) is,

$$\begin{pmatrix} E_{S1} \\ H_{S1} \end{pmatrix} = M_{S1} \cdot \begin{pmatrix} E_{S2} \\ H_{S2} \end{pmatrix}$$

$$M_{S1} = \begin{bmatrix} m_{11} & m_{12} \\ m_{21} & m_{22} \end{bmatrix}$$

$$= \begin{bmatrix} \cos \kappa_0 n_1 w & i \cdot (Z_2 \cdot H_{S2} \cdot \sin \kappa_0 n_2 w \\ \frac{E_{S2}}{Z_2} \cdot (i \cdot \sin \kappa_0 n_2 w) & H_{S2} \cdot \cos \kappa_0 n_2 w \end{bmatrix} \quad (3.4.6)$$

If the structure consists of the multiple layer, the solution of each layer can be formulated in the form of matrix and the response of the overall structure can be found by multiplying matrix of each layers. ($M = M_{S1} \cdot M_{S2} \cdot M_{S3} \cdot \ldots \cdot M_{Sn}$).

After formulation of matrix the transmittance and reflectance can be evaluated as,

Transmission coefficient, $t = \frac{|E_{tS1}|}{|E_{iS1}|}$

Reflection coefficient, $r = \frac{|E_{rS1}|}{|E_{iS1}|}$

The more simplified expression is,

$$t = \frac{2 \cdot Z_3}{Z_3 \cdot m_{11} + m_{12} + Z_1 \cdot Z_3 m_{21} + Z_1 \cdot m_{22}}$$

$$r = \frac{Z_3 \cdot m_{11} + m_{12} - Z_1 \cdot Z_3 m_{21} - Z_1 \cdot m_{22}}{Z_3 \cdot m_{11} + m_{12} + Z_1 \cdot Z_3 m_{21} + Z_1 \cdot m_{22}} \quad (3.4.7)$$

3.5 Eigenmode Expansion Method

In comparison to other discretizing structures like FDTD and FEM method, the EME method is computationally faster. The discretization in EME is performed on the invariant Z direction (propagation direction). In this method, the complete structure is divided into N number of non-varying substructures (multiple sub-structures), and then the calculation is performed for the fully vectorial modes in each substructure. The computed modes form a basis set for further evaluation of the mode matching analysis at the interface between the adjoining substructures. At the interface, the tangential continuity of the field components provides the transmission/reflection of the each substructure, and it is computed through the scattering matrix. Once the transmission/reflection of the substructure is known a basic matrix multiplication gives the propagation through the entire structure [113].

As we consider the propagation of wave in z-direction, the electric field is represented as, $E_{(x,y,z)} = \overrightarrow{e_n}(x,y) \cdot e^{j\beta_n z}$, where $\overrightarrow{e_n}(x,y)$ and β_n is the basic Eigen function and Eigen value respectively.

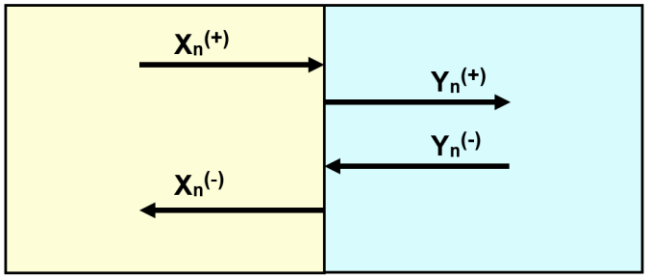

Figure 3.5.1: Forward and backward propagating modes for EME

From the Figure 3.5.1 it is shown that the incident guided mode propagating from a waveguide segment X to Y form a basis set of the modes that can be represented in terms of the forward and backward propagating modes. The tangential component of each substructure at the interface can be written as,

$$\sum_{k=1}^{n}\left(X_k^{(+)}e^{j\beta z}-X_k^{(-)}e^{-j\beta z}\right)\cdot E_{k,t}^{(X)}(x,y) = \sum_{k=1}^{n}\left(Y_k^{(+)}e^{j\beta z}-Y_k^{(-)}e^{-j\beta z}\right)\cdot E_{k,t}^{(Y)}(x,y) \quad (3.5.1)$$

Where $X_k^{(+)}, Y_k^{(+)}$ and $X_k^{(-)}, X_k^{(-)}$ are the amplitudes of modes propagating in +z and –z direction. After solving above-mentioned equation for transmission/reflection coefficient at the substructure and interface the response of the entire structure is done through scattering matrix method.

$$\begin{pmatrix} X^{(-)} \\ Y^{(+)} \end{pmatrix} = S\cdot\begin{pmatrix} X^{(+)} \\ Y^{(-)} \end{pmatrix} \quad (3.5.2)$$

Where S is the scattering matrix for the waveguide segments X and Y.

3.6 Bragg Grating Waveguide

Bragg grating waveguide is an extension of the well-known fiber Bragg gratings. The concept evaluates from the Bragg diffraction require studying the characteristics of the crystalline materials. The electromagnetic waves when incident on the crystal, the diffraction phenomena occurs and the scattered waves experience the constructive interference that follows the Bragg's law, ($n\cdot\lambda = 2\cdot d\cdot\sin\varphi$), where d is crystal period, φ is the angle of scattering [114–116].

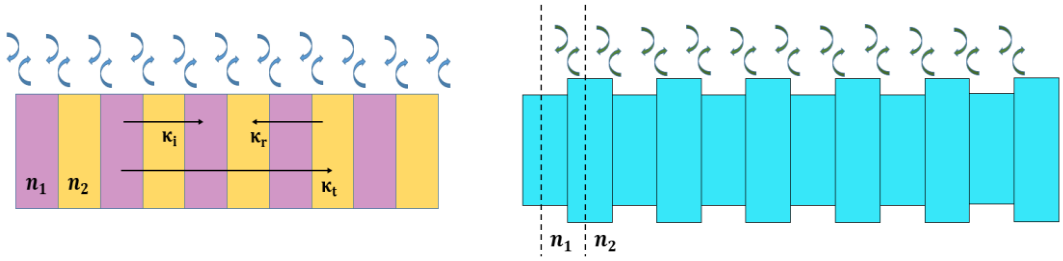

Figure 3.6.1: Bragg grating waveguide

The easiest way to achieve a Bragg response is by making periodic arrangements of the two different refractive indices as shown in Figure (3.6.1). The configuration can be achieved either by making use of two various materials or by providing periodic perturbation of the waveguide parameters, especially alteration of the waveguide width or height. This periodic perturbation changes the effective index of the propagating optical mode. At the interface of each altering effective index, the reflection of the propagating mode occurs. After several simultaneous reflections, only those attain constructive interference tend to be highly reflected, while others cancel out each other's and propagate through gratings. These reflected signals are in a narrow band around Bragg wavelength. This configuration can also be considered as a 1-dimensional photonic crystal, where the reflected narrowband signal appears as a stop band region of the transmission spectra.

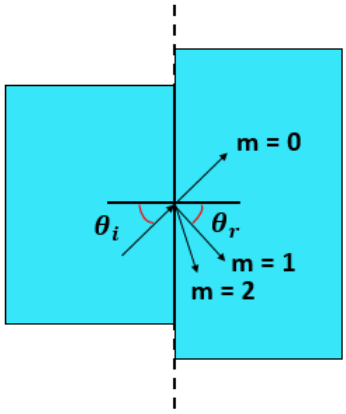

Figure 3.6.2: Diffraction phenomena due to Bragg gratings

The schematic shown in Figure 3.6.2 represents the diffraction of signal due to Bragg gratings. Consider a Figure 3.6.2 the propagating signal is represented through a wave vector κ_i and reflected signal wave vector is κ_r, both have a magnitude of $(2\cdot\pi)/\lambda$. The periodic structure can pass a signal is represented through a wave vector of κ_t. To evaluate the Bragg condition we must equate the matching of the wave vector,

$$\kappa_i + \kappa_t = \kappa_r$$

$$\kappa_r = n \cdot \sin\theta_r + m \cdot \frac{\lambda}{\Lambda} \tag{3.6.1}$$

where m is the diffraction order and Λ is the period of a grating.

For a stepwise variation in the refractive index the overall effective index (n_{eff}) of the mode can be considered as an average of n_1 and n_2 (effective indices of individual segment of waveguide gratings) [40]. The mode coupling at λ_B should have equal wave vectors of two contra propagating modes, $-\kappa_r = \kappa_i$, which gives,

$$-\left[n_{eff} + (-1) \cdot \frac{\lambda_B}{\Lambda}\right] = n_{eff}$$

$$\lambda_B = 2 \cdot \Lambda \cdot n_{eff} \tag{3.6.2}$$

In the perspective of coupled wave theory [117], we can represent the propagating optical mode as a sum of electric field components of two contra propagating modes, forward (F) and reflected (R),

$$E(z) = F(z)e^{-i\cdot\beta_0\cdot z} + R(z)e^{-i\cdot\beta_0\cdot z} \tag{3.6.3}$$

where $\beta_0 = \left(2\pi/\lambda\right) \cdot$ neff, is the propagation constant.

The coupled mode equation from [118] are,

$$\frac{dF}{dz} - i\Delta\beta R = i\kappa R$$

$$\frac{dR}{dz} + i\Delta\beta R = -i\kappa F \qquad (3.6.4)$$

where κ is the coupling coefficient defined as the aggregation of reflections per unit length. The reflection coefficient is considered by assuming Fresnel's equation, and at an interface, it is represented as a ratio of $(n_2 - n_1)/(n_2 + n_1)$. Every individual grating period provides two reflections, hence the coupling coefficient (κ) for a grating period is,

$$\kappa = 2 \cdot \frac{(n_2 - n_1)}{(n_2 + n_1)} \cdot \frac{1}{\Lambda} \qquad (3.6.5)$$

From the coupled mode theory the expression of reflection coefficient can be represented by [40,118],

$$r = \frac{-i \cdot \kappa \cdot \sinh(\gamma L)}{\gamma \cdot \cosh(\gamma L) + i \cdot \left(\frac{2 \cdot \pi}{\lambda}\right) \cdot \Delta n_{eff} \cdot \sinh(\gamma L)} \qquad (3.6.6)$$

where $\gamma^2 = \kappa^2 - \left(\left(\frac{2\cdot\pi}{\lambda}\right) \cdot \Delta n_{eff}\right)^2 = \kappa^2 - (\Delta\beta)^2$.

In equation (3.6.6) if $\left(\frac{2\cdot\pi}{\lambda}\right) \cdot \Delta n_{eff} = \Delta\beta = 0$, then, $r = -i \cdot \tanh(\kappa L)$.

Hence the peak power reflectivity, $R_P = \left|\tanh^2(\kappa L)\right|$

The bandwidth of the reflected signal is also an important parameter of concern. It is easily evaluated through the consideration of the coupled mode equation (3.6.4),

$$\frac{d^2F}{dz^2} + (\gamma^2)F = 0 \qquad (3.6.7)$$

There are two solution of the equation,

(i) when $\Delta\beta < \kappa$, the signal will decay exponentially and the reflection becomes stronger. The wavelength approaches to λ_B. Here $\gamma^2 = (\Delta\beta)^2 - \kappa^2$.

(ii) when $\Delta\beta > \kappa$, the signal wavelength lies at the outermost region of the stop band. At this point, $\gamma^2 = \kappa^2 - (\Delta\beta)^2$

After adjustments of the parameters, the value of bandwidth found out to be [40],

$$\Delta\lambda = \frac{\lambda_B^2}{\pi \cdot n_g}\sqrt{\kappa^2 + \left(\frac{\pi}{L}\right)^2} \tag{3.6.8}$$

where L is the length of the grating waveguide.

For a long period grating waveguide, the approximate solution of the bandwidth ($\Delta\lambda$),

$$\Delta\lambda = \frac{\lambda_B^2 \cdot \kappa}{\pi \cdot n_g} \tag{3.6.9}$$

From the equation it is also depicted that the by knowing the coupling coefficient (κ), bandwidth can be directly evaluated.

3.7 Finite Difference Time Domain Method (FDTD)

It is one of the most influential tools to analyze a structure for solutions of the propagating electromagnetic waves. The FDTD is used in various applications such as antenna and microwave circuits, photonic devices (such as couplers, photonic crystals, etc.), thermal absorption in the body, etc. This method has been proposed by K. Yee and is subsequently improved in the 1970s. The technique is simple to implement and works by discretizing the complete structure into number of cells, which are called as Yee's cell. Also it does not impose any dependency on material media. The schematic is shown in Figure (3.7.1).

The electromagnetic wave propagates from one cell to another. Bloch (or) perfectly matched layer (PML) boundary conditions are used for absorption of waves near the edges. The fundamental formulation is based on the electromagnetic curl equation [90].

$$\nabla \times E = -\frac{\partial B}{\partial t}$$
$$\nabla \times H = J + \frac{\partial D}{\partial t} \tag{3.7.1}$$

where $B = \mu E$, and $D = \varepsilon E$.

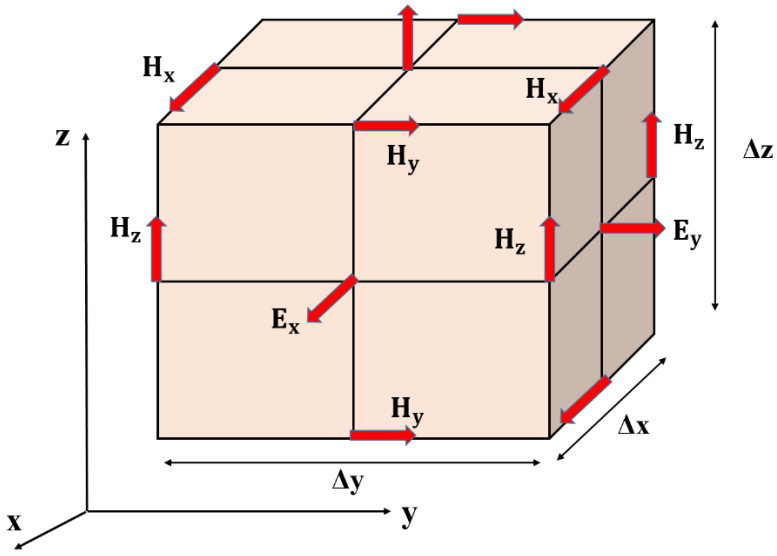

Figure 3.7.1: Schematic of Yee cell [90]

The equation must be substituted in the Yee cell so that it represent time and space discretization. Let us consider a cell of a structure represented by a function P,

$$\frac{\partial P^n(i,j,k)}{\partial x} = \frac{P^n\left(i+\frac{1}{2},j,k\right) - P^n(i-\frac{1}{2},j,k)}{\delta}$$
$$\frac{\partial P^n(i,j,k)}{\partial t} = \frac{P^{n+\frac{1}{2}}(i,j,k) - P^{n-\frac{1}{2}}(i-\frac{1}{2},j,k)}{\Delta t} \tag{3.7.2}$$

This two dimensional approximation (spatial and time) are implemented in all the six equations of electromagnetic waves for each component. Here for a demonstration we have consider the E_y field component,

$$E_y\Big|_{i,j+\frac{1}{2},k}^{n+1} = \frac{M_y\Big|_{i,j+\frac{1}{2},k}^{-}}{M_y\Big|_{i,j+\frac{1}{2},k}^{+}} + \frac{\Delta t}{\epsilon_{yy}\Big|_{i,j+\frac{1}{2},k} \cdot M_y\Big|_{i,j+\frac{1}{2},k}^{+}} \begin{bmatrix} H_x\Big|_{i,j+\frac{1}{2},k+\frac{1}{2}}^{n+\frac{1}{2}} - H_x\Big|_{i,j+\frac{1}{2},k-\frac{1}{2}}^{n+\frac{1}{2}} \\ H_z\Big|_{i+\frac{1}{2},j+\frac{1}{2},k}^{n+\frac{1}{2}} - H_z\Big|_{i-\frac{1}{2},j+\frac{1}{2},k}^{n+\frac{1}{2}} \end{bmatrix} \qquad (3.7.3)$$

where

$$M_y\Big|_{i,j,k}^{\pm} = 1 \pm \frac{\sigma_{yy}\Big|_{i,j,k} \cdot \Delta t}{2 \cdot \epsilon_{yy}\Big|_{i,j,k}}$$

Through this way, all other components of the electromagnetic wave can be derived. The time discretization satisfying the Courant condition is,

$$\Delta t < \frac{1}{\frac{c}{n} \cdot \sqrt{\frac{1}{\Delta x^2} + \frac{1}{\Delta y^2} + \frac{1}{\Delta z^2}}} \qquad (3.7.4)$$

The typical dimension of the mesh size (Δx, Δy, and Δz) should be less than $\lambda/10$ for getting the finer mesh and accurate approximation of the result.

3.8 Summary

In this chapter, we have discussed the analytical and simulation modeling of the waveguide. Modal calculation and the cutoff condition for a strip and slot waveguides are derived. As we know that, the finite-difference-time-domain method is not computationally suitable for wide and larger length devices. Therefore, for analyzing such devices, frequency domain based eigenmode expansion method has presented which has used for implementation of the periodic devices. Apart from these simulation techniques, analytical modeling of the periodic device using the transfer matrix method (TMM) is also discussed.

The TMM method is speedy, computationally stable and efficient, especially for a device with large geometric length. The study regarding an evaluation of the necessary parameters of the grating waveguide structure are also performed. The theoretical background concerning a fundamental implementation of the discussed photonic devices are utilized to analyze the more advanced photonic components in the further chapters.

Chapter 4

Characterization of the strip waveguide using Michelson Interferometer

In this chapter, we have presented the working of the Michelson interferometer (MI) for the characterization of waveguide parameters. The previous chapter introduced about the mathematical modelling of the planar waveguides that provides an intuitive information of the cutoff conditions and the number of modes propagation in a waveguide. Here we have performed the modal analysis of the waveguide by considering the eigenmode calculation method. Fundamental parameters such as effective index, group index, extinction ratio and FSR are studied and the experimental and simulation results are compared. The fabrication of the device is facilitate by the Applied Nanotool Inc. As the larger waveguides and the resonating structures often required the bending of the waveguide, hence minimizing the bending loss for bend radius is also presented here. At an end, the biosensing ability of the device for a TM operated mode is provided.

4.1 Introduction

The momentum of the photonic technology is shifted towards a development of the system by using a group of optimized devices. In a last decade, the integrated optical devices have been widely investigated. In every domain from homeland security to biomedical diagnostics, devices based on integrated optics (IO) have been implemented. The main advantages of IO are simple fabrication process, robust, flexible, and compact in size [105]. The IO technologies enhanced the performance-sensing device by utilizing the conventional CMOS fabrication facilities. Hence, on the same substrate the lasing source and detection unit can be implemented. The most profoundly used IO device is Mach Zehnder interferometer (MZI). The study is provided in chapter 2. In literature, various

applications of the device are reported [22,119–121]. For biosensing, the MZI provides high sensitivity and lower limit of detection [121].

MZI based biosensor provide higher sensitivity that is primarily reliant on the length of unbalanced arm. Higher sensitivity obtained for longer arm length, which also increase the overall dimension of the device [122]. Hence the probable alternate of MZI is Michelson Interferometer (MI) in which signal travels twice in both arms because of a loop mirrors attached at the end of both arms, so effective length of arm of MI device is twice as that of MZI. Hence, propose a simple and compact design of Michelson Interferometer for bio-sensing application.

4.2 Michelson Interferometer (MI)

The schematic of the MI is shown in Figure 4.2.1, the input is provided in the arm of the bidirectional couple, which is propagated and divided into two equal parts. The length of both the arms are different (L_1 and L_2), so the configuration is called as unbalanced MI. Both the arms provides a phase shift to the signals and by means of the attached loop mirrors, the signal propagated twice in both the arms. In comparison to the MZI, signals travels twice in both the arms hence contributing twice the phase shift [122].

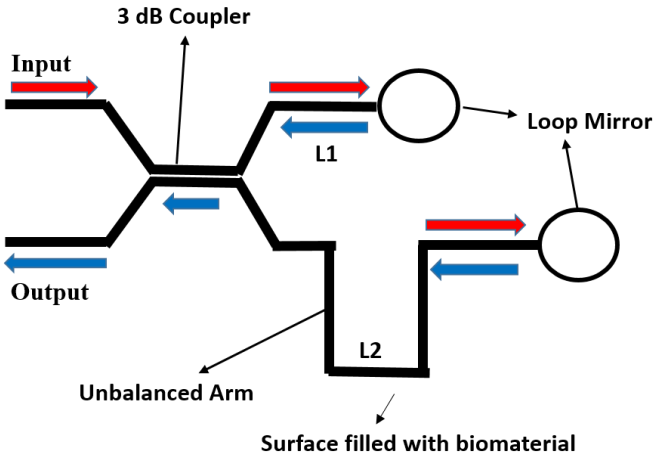

Figure 4.2.1: Michelson Interferometer

4.3 Characterization of a Strip Waveguide

The modal analysis of the waveguide is performed using the full-vector based Eigen mode solver method. The analytical study for an evaluation of the modal calculations is discussed in Sec. 3.2. The waveguide is drawn on SOI platform, with a waveguide height of 220 nm and thickness of 500 nm. The material used in the core region is silicon (Si) with a refractive index of 3.47. The height of the substrate and upper cladding region (silicon oxide, SiO_2) of 2 µm thickness is used, which is having a refractive index of 1.444.

The plot in the Figure 4.3.1 represents the wavelength dependency of the effective and the group index considering dispersion effects. The simulation is carried out for a wavelength range of 1500-1600 nm.

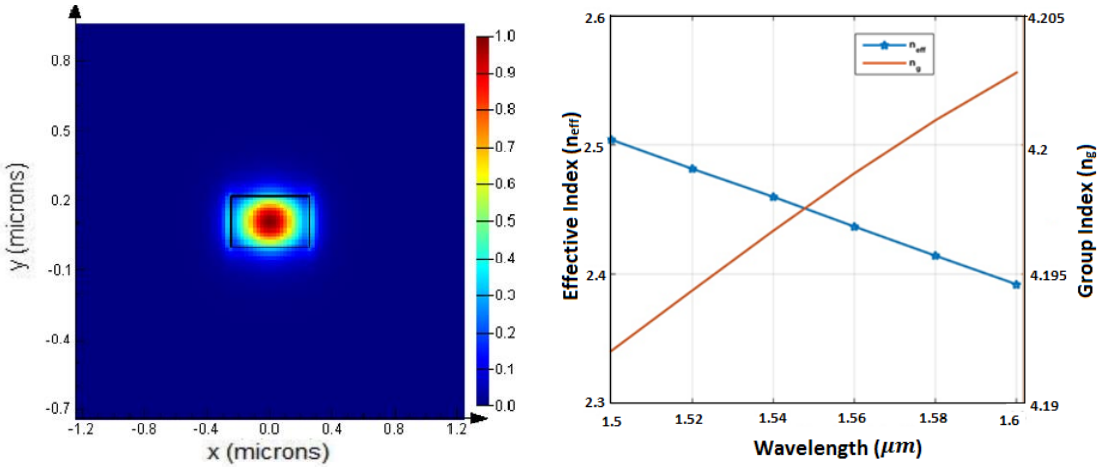

(a) (b)

Figure 4.3.1: (a) Electric field profile of a waveguide, (b) plot showing variation of the effective index and group index for a change in wavelength

Since the effective index is dependent on the waveguide parameters, so for the above mentioned configuration of a waveguide, the approximate compact model is,

$$n_{eff} = 2.44763 - 1.12907 \cdot (\lambda - 1.55) - 0.0354547 \cdot (\lambda - 1.55)^2 \qquad (4.3.1)$$

4.3.1 Loss factors

The dispersive component of the materials used in a waveguide contributes several types of losses, which may severely affects the performance of the device. The most fundamental losses are propagation and bending loss. The signal propagated in a waveguide is described by a comples refractive index (n + ik), so the expression of the electric field is [40],

$$E = E_0 e^{-i\frac{2\pi(n+ik)}{\lambda}L} \qquad (4.3.2)$$

where L is the length of a waveguide. The effective and group index is dependent on the n, and the complex portion (k) represents the optical losses. The optical losses in a waveguide is primarily occurred due to the roughness of the sidewalls because of the etching process during fabrication [123,124]. That is the reason of utilizing the high index contrast waveguide, because in that the modal confinement is high in the core region and small portion of the field present on the surface is affected by the surface roughness (nanometer size deformities). However, the bend losses are very important for the consideration, the most common applications requiring bending losses are ring reosnators, and IO devices requiring large waveguide segments. For an IO devices, often bending of the waveguides are required for an efficient utilization of the space. Sharp corners at a bending causes degradation of the signal strength due to the scattering losses [123].

The bending losses are occurred due to an occurnce of the radiation and modemismatch loss. When signal propagates in bending region of a waveguide, its orientation tends to move toward the sharp corners which causes a signal to radiate and looses its strength. Whereas, the modemismatch loss is occurred due to an imperfection in the overlapping of the modes from straight to a bending segment of a waveguide. The reported study with experimental verficiation shows that for the above mentioned waveguide parameters the bending loss gets reduced on increasing the radius of the bend. For a 1μm and 5 μm bend radius the losses are 0.1 dB and 0.01 dB per 90^0. As the bend radius increases the bend loss gets reduced, but the higher bending radius requires more of the substrate area. In this work,

we have simulated the bend radius, and optimized radius of 5 μm is considered, which have contributed a bending loss of 0.0134 dB.

4.3.2 Modeling of Michelson Interferometer

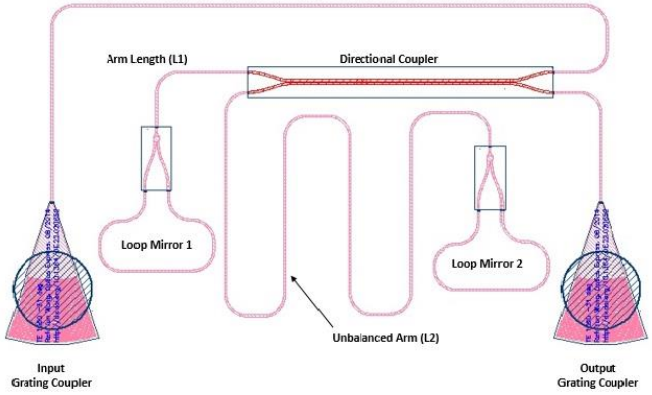

Figure 4.3.2: Fabricated schematic of a MI, drawn in Klayout

The schematic of the MI is shown in figure. The device consists of a 3-dB adiabatic directional coupler, two 3-dB Y branch couplers and two vertical grating couplers [23,125,126]. The two vertical grating couplers are attached at the two ends of the directional coupler that are used for an input and output ports. The other ends of the directional coupler is provided with two Y-branch coupler and are connected with a waveguide segment to make a loop. The length of unbalanced arms are L_1 and L_2. Complete device is drawn on SOI to occupy a 78.5 × 1458.06 μm^2 of substrate area.

4.3.3 Fabrication and Measurement

Applied Nanotools Inc. fabricated the devices with the NanoSOI e-beam fabrication service [127]. For fabrication, 100 keV Electron-Beam-Lithography (EBL) is utilized [128]. The fabrication employed a silicon-on-insulator (SOI) wafer with 220 nm thick silicon (Si) on 3 μm thick silicon dioxide (SiO_2). The substrates are 25 mm squares diced from 150 mm wafers. After a piranha cleanse with hot-plate dehydration bake, hydrogen silses-quioxane resist (HSQ, Dow-Corning XP-1541-006) is spin-coated at 2000 rpm and consequently baked. Electron beam lithography is performed using a Vistec EBPG 5000+

system operated at 100 keV energy, 8 nA beam current and 320 μm exposure field size. The equipment grid intended for design positioning is 2.5 nm, whereas the gaping between dwell points throughout the pattern making is 5 nm. The resist is developed using tetra-methyl-ammonium-hydroxide (25%) for 4 minutes, followed by a deionized water rinse and rinse in isopropyl alcohol. The silicon is removed from unexposed areas using an inductively coupled plasma etch in an Oxford Plasma lab System 100 etcher. Residual HSQ resist is then removed using a wet buffer oxide etch. Silicon dioxide cladding of 2.25μm thick-ness is finally deposited applying a Trion plasma enriched chemical vapour deposition (PECVD) process having tetra-ethoxysilane (TEOS) with oxygen at a temperature of 300ºC. To characterize the devices, a custom-built automated test setup with automated control software written in python is used [129]. For input source Agilent, 81600B tunable laser is used and for output, detector Agilent 81635B optical power sensor is used. The wavelength is swept from 1.5 μm to 1.6 μm in 10 pm steps. To maintain polarization of fiber a polarization maintain fiber is used to couple in and out of grating coupler to fiber.

For an evaluation of the transmission spectra of the device shown in the Figure 4.3.2, the power is injected from a tunable laser into the input grating coupler. Coupled power transfers from a waveguide to a bidirectional coupler are split into two signals and propagate in two loop mirrors. Two loop mirrors are separated by different path length ($\Delta L = L_2 - L_1$) experience the variation in phase difference. Signal again couples back to a bidirectional coupler and pass to an output grating coupler to be detected.

The power measured at output grating coupler is shown in the Figure 4.3.3, from the experimental results several parameters like group refractive index, free spectral range (FSR), extinction ratio are evaluated and compared with simulated results for variation in path length of MI. Extraction of parameters are performed by matching the experimental results to analytical model of the device. By performing the curve fitting using least square method we have determined the period of oscillations of the FSR and then by using it we have evaluated the group index.

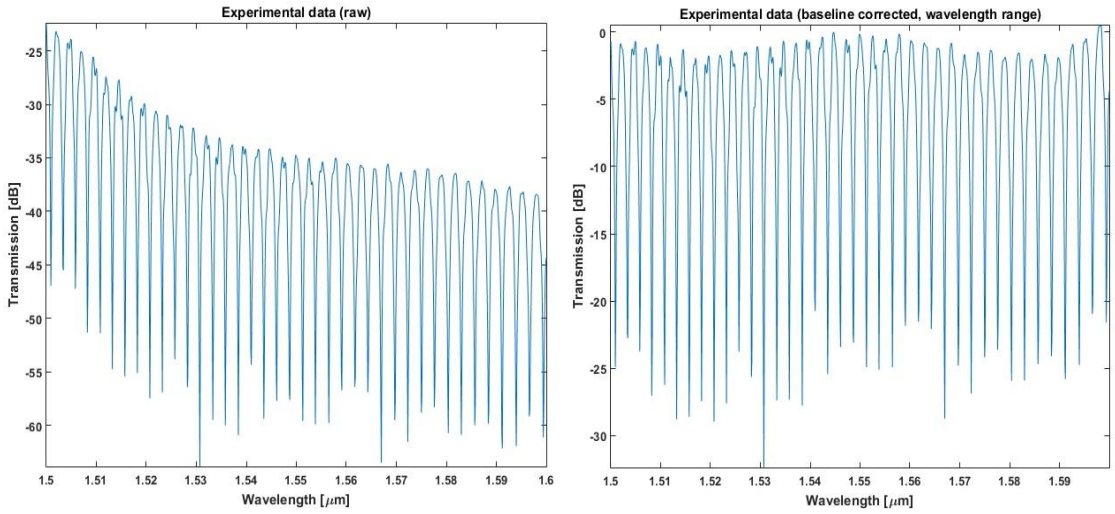

(a) (b)

Figure 4.3.3: (a) Plot of raw experimental data, (b) baseline corrected data for parameter extraction

Three MI devices are investigated, which are having a variating in the path length differenc. The measurement of parameter is done for the wavelength range of 1.54-1.56 µm.

Table 4.3.1: Experimental and simulated results corresponding to various path length of Michelson Interferometer

Device name	**Path Length ΔL (μm)**	**Experimental**			**Simulated**	
		n_g	**FSR (nm)**	**Extinction Ratio (dB)**	**FSR (nm)**	**Extinction Ratio(dB)**
MI01	108.7	4.2643	2.8	24.96	2.71	27.02
MI02	168.3	4.2473	1.9	23.53	1.72	26.8
MI03	214.11	4.2530	1.5	22.13	1.35	26.65

The first device under test is MI01 has a measured path length difference of 108 µm giving a relatively large free spectral range of 2.8 nm and extinction ratio of 24.959 dB. The other two device MI02 and MI03 consists of path length differences of 168.3 µm and 214.11 µm provided with the FSR value of 1.9 nm and 1.5 nm respectively. The results extracted from the experimental data of devices resembles close similarity with the simulation results. Minute differences arise due to imperfection in fabrication process or the calibration of

manufacturing unit. This device can also be used for sensing application utilizing the fact that it uses small footprint.

4.4 Biosensing characteristic

For bio-sensing application, the high presence of the field on the surface is desirable. The biorecognition layer is considered to be present on the top of the waveguide which only binds the intended analyte. The homogenous sensing is opted and the uniform refractive index at the upper cladding is considered for representing the presence of biomaterial.

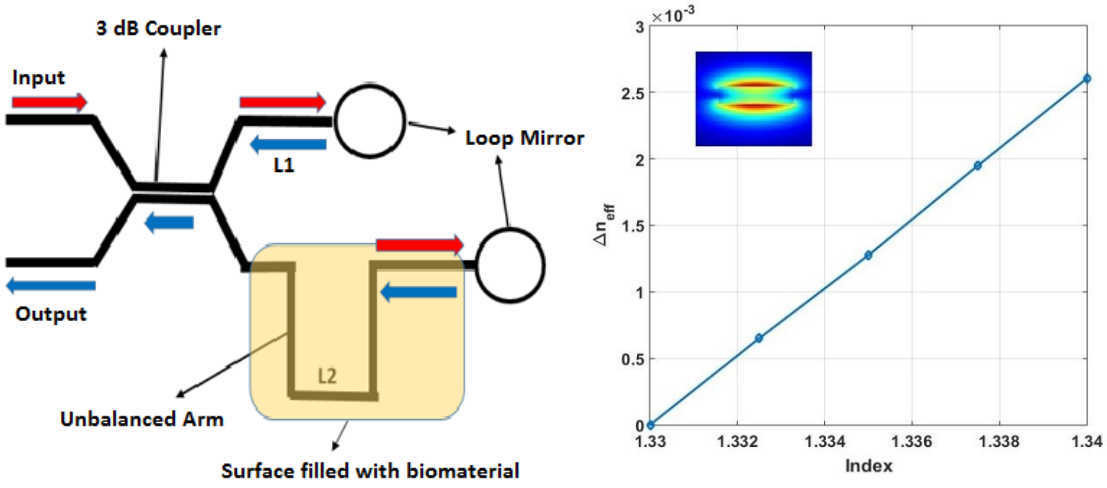

(a) (b)

Figure 4.4.1: (a) Schematic of proposed biosensor, (b) variation of a change in the effective index corresponding to a change in biomaterial

In continuation of the mentioned schematic of the MI (Figure 4.3.2), the arm lengths are L_2, L_1 are 500 µm and 31.7 µm respectively as shown in Figure 4.4.1. For a TM mode, concentration of signal lie above the surface of a waveguide, which increase the interaction between evanescent wave and biomaterial. Increase interaction causes to modify the effective index, which transforms the phase shift of device. The refractive index of an upper surface of an unbalanced arm region (sensing area) is 1.33 (refractive index of water). The expression of phase shift due to change in n_s can be written as,

$$\Delta\phi = \beta(2L_2) - \beta(2L_1) = \beta(2\Delta L) \tag{4.4.1}$$

where $\Delta L = L_2 - L_1$ represents path difference between two arms. Phase shift change occurs due to small change in index of biomaterial is,

$$\frac{\Delta\phi}{\Delta n_s} = \frac{2\pi}{\lambda}\frac{\partial n_{eff}}{\partial n_s}(2\Delta L) \tag{4.4.2}$$

Change in n_s for π phase shift,

$$\Delta n_s = \frac{\lambda}{2(2\Delta L)}\frac{\partial n_s}{\partial n_{eff}} \tag{4.4.3}$$

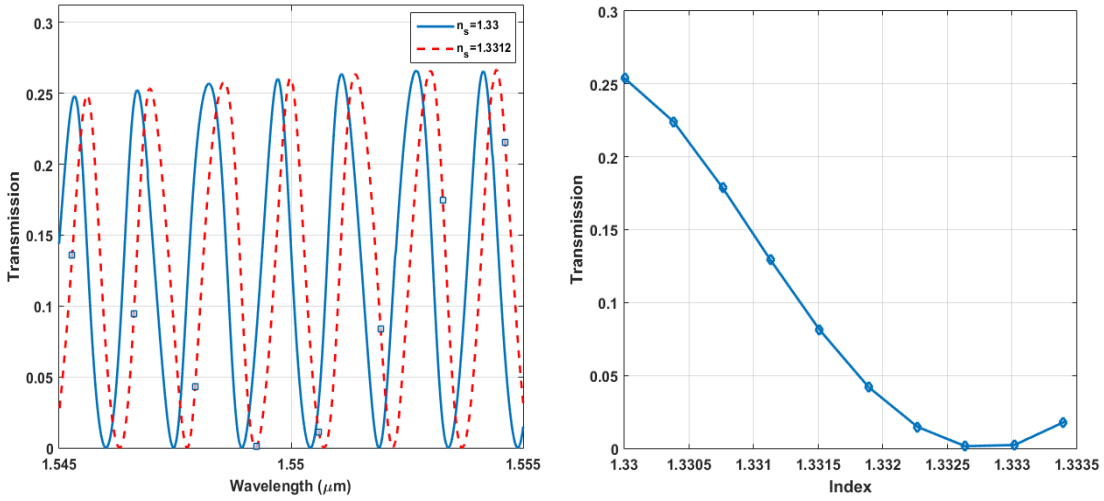

(a) (b)

Figure 4.4.2:Transmission spectra (a) for variation in the biomaterial refractive index (n_s), (b) of sensor for fixed value of wavelength (1.55 μm) for a n_s ranges from 1.33-1.3334

The change in effective index corresponding to change in index (n_s) is plotted in Figure 4.4.1, through this evaluation of minimum change in index required for making π phase shift is calculated which is found to be 0.00343. This is required to analyze the transmission spectra and to calculate sensitivity corresponding to change in sensing medium index (n_s)

at fixed wavelength of 1.55 μm (Figure 4.4.2). The sensitivity of device is calculated to be 225 nm/RIU. The device is having a high sensitivity but the detection limit is less than 3.43×10^{-3} RIU. Apart from that the output has a sinusoidal variation that causes a difficulty in prediction of the biomaterial and the collation of the several components (y-branch and contradirectional couplers) requires an optimized performance of all devices for an efficient working of the overall system.

4.5 Summary

In this chapter, the planar waveguide is characterized through the Michelson interferometer for a TE operated optical mode. The main feature of the SOI wafer is the high index contrast between the core and the cladding. The high index contrast supports strong modal confinement in the core region hence provide an advantages such as lower propagation loss, minimum bending loss, etc. Here in this work, we have considered the commercially available wafer of SOI and the selected waveguide dimensions are 500×220 nm. Applied Nanotool Inc. fabricated the device and the provided results are in good agreement with the simulated results. The studied fundamental parameters are effective index, group index, extinction ratio and FSR. The study concerning the losses associated with the bending of the waveguide is also considered, and that is utilized in the designing of the ring resonator discussed in chapter 7.

The MI configuration is surely an advantage corresponding to MZI configuration in terms of large phase shift and the dimension of the device. The loop mirrors at an end of the arms causes to signal to propagate twice in both the arm. For a biosensor, the smaller fraction of light is present on the surface hence the weaker interaction occurs between the considered biomaterial and the signal. For a TM operated mode, the biosensing capability is evaluated and the sensitivity of the device is found out to be 225 nm/RIU with a detection limit is around 3.43×10^{-3} RIU. There are few disadvantages associated with MI such as sinusoidal out variation, lower detection limit, collation of several components etc.. Hence the waveguide configuration is utilized for resonating structures in the later portion of the work.

Chapter 5

Straight Resonators based on Strip Waveguide

The evanescent field sensing often required the higher light matter interaction. The planar waveguide based architecture such as an interferometer suffers from the limitation of the sinusoidal variation of the output intensity, larger length of the device and an efficient integration of several components (directional couplers, y branch couplers etc.). The preferable approach is to use the resonator structure, which facilitate the higher presence of field for the confined mode. On presence of the biomaterial on the surface of the resonating structure, the effective index is modified that simultaneously changes the resonating condition. So the principle utilize for the detection purpose is to analyse the movement of the resonating band for a change in physiochemical properties of the biomaterial.

The working of the considered grating based resonating structure are dependent on the Bragg condition. The theoretical description of the relationship between the coupling coefficient and the bandwidth of the stopband is provided in Sec. 3.6 (equation 3.6.7 and 3.6.8). The first structure have a high coupling coefficient which generates the resonating band based on the insertion of the cavity whereas another structure generates the narrow reflection band which is due to the lower coupling between the optical field and the gratings. In this chapter, we have illustrated the analytical modeling and parameter evaluation of the photonic biosensor using cascaded silicon grating waveguides and the narrowband cladding modulated grating waveguide.

5.1 Cascaded Bragg Grating Waveguide

The proposed sensor consists of two cascaded waveguides with symmetric sidewall gratings to broaden the stop band region of the transmission spectra. Here, we first analyze the structure using the transfer matrix method. We then optimize the parameter values in

order to obtain sharp resonant peak in the center of the stop band. Notably, the resonant band of this structure provides a high Q factor of 1.544×10^5, which significantly improves the limit of detection. In this study, we have also demonstrated the effect of temperature on the detection of biomaterials. The evaluated temperature sensitivity of the device is -0.0075nm/^{o}C over a temperature range of 18 ^{o}C to 34 ^{o}C.

The grating based resonator structures have a capability of providing higher sensitivity and lower limit of detection [63]. The structure utilizes the conventional slab waveguide in which the mode is concentrated on the high index core region that is extended to sidewalls of the waveguide. The small deformity on the sidewall is replicated back by changing the optical characteristic of the structure. Therefore, the Bragg structure can be designed by periodically adjusting the waveguide width that correspondingly changes the effective refractive index. The periodic change of effective index is the basis of the stop band region on the transmission spectra. This structure can further be exploited for a creation of the sharp resonating band by placing a cavity at the center of the periodic grating structure [40,46,103]. The movement of the resonating band corresponding to a change in the refractive index of the surface biomaterial can be utilized for biosensing applications. Basically, a binding event of the molecules perturbed the refractive index of the surface of a sensor, resulting in a shift of the resonant wavelength. Such types of photonic sensors are highly sensitive, and can easily detect and differentiate minimal changes in refractive index by promoting higher interaction between light and biomaterial. Prabhathan et al. have demonstrated high Q and highly sensitive Bragg grating biosensor based on phase-shift cavity resonator [103]. Samira et al. show the temperature stability of the photonic sensor by considering the temperature variant microfluidic framework [130]. The proposed structure composed of the cascading of two grating waveguides, which widen the stop band region in the transmission spectra. The optimized cavity in between the two waveguides produces a sharp resonant peak of the order of ~10^5. In the end, the effect of variation of temperature on the upper cladding surface is also characterized. The content of the work is as per following, Sec. 5.1.1 presents the theory and analytical modeling of Bragg grating structure, Sec. 5.1.2 depicts device structure and discusses the methodology to model stop

band. Evaluation of bio-sensing parameters is described in Sec. 5.1.3. Temperature dependence of the defect cavity is investigated in Sec. 5.1.4.

5.1.1 Analytical modeling of a grating waveguide

The schematic of a single grating segment is shown in Figure 5.1.1. The signals when propagated through the structure suffers reflections at all interfaces. After many simultaneous reflections, only those signals that achieve constructive interference are highly reflected, while others cancel each other and propagate through gratings of a waveguide. The reflected signals are observed in the transmission spectra in the form of stop band [116].

Analytically through the transfer matrix method (TMM) the evaluation of the output response of the cascaded grating waveguides (CGW) is performed. The signal propagation in the interface 1-2 (step index) is represented by the reflection and transmission coefficient, which is evaluated through the consideration of the Fresnel's equation of the reflection $(n_2 - n_1)/(n_2 + n_1)$ [40], where n_1 and n_2 are effective refractive index of the waveguide segment shown in Figure 5.1.1. The corresponding matrix representation is,

$$\begin{bmatrix} F_2 \\ B_2 \end{bmatrix} = \begin{bmatrix} 1/t & r/t \\ r/t & 1/t \end{bmatrix} \cdot \begin{bmatrix} F_1 \\ B_1 \end{bmatrix} = \begin{bmatrix} \frac{n_1 + n_2}{2\sqrt{n_1 \cdot n_2}} & \frac{n_1 - n_2}{2\sqrt{n_1 \cdot n_2}} \\ \frac{n_1 - n_2}{2\sqrt{n_1 \cdot n_2}} & \frac{n_1 + n_2}{2\sqrt{n_1 \cdot n_2}} \end{bmatrix} \cdot \begin{bmatrix} F_1 \\ B_1 \end{bmatrix} = M_{1-2} \cdot \begin{bmatrix} F_1 \\ B_1 \end{bmatrix} \quad (5.1.1)$$

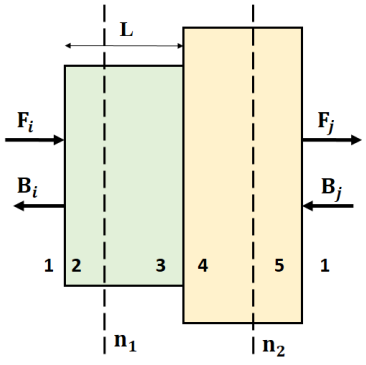

Figure 5.1.1: Layered structure (single grating segment of a waveguide)

Similarly, the matrix representation of the signal propagating from segment 2-3 (homogeneous waveguide) is,

$$\begin{bmatrix} F_3 \\ B_3 \end{bmatrix} = \begin{bmatrix} e^{-j\beta L} & 0 \\ 0 & e^{j\beta L} \end{bmatrix} \cdot \begin{bmatrix} F_2 \\ B_2 \end{bmatrix} = M_{2-3} \cdot \begin{bmatrix} F_2 \\ B_2 \end{bmatrix} \quad (5.1.2)$$

where β is a propagation constant considering effective index and propagation loss (α) and L is the length of the layer.

The overall matrix representation of the complete structure (M_{BG}) shown in Fig. 1 is,

$$M_{BG} = M_{1-2} M_{2-3} M_{3-4} M_{4-5} \quad (5.1.3)$$

Then the matrix representation of the complete grating waveguide with N number of grating periods is,

$$M = (M_{BG})^N \quad (5.1.4)$$

5.1.2 Cascaded grating waveguide (CGW) and stop band modeling

The proposed structure of a CWG is shown in Figure 5.1.2. The evaluation of a fundamental modes is performedd using finite difference based Eigen-mode solver approach. Although several modes are found but according to a requirement to produce a wide stop band, here we have considered the fundamental quasi-TE mode. The field concentration of the TM mode is mostly on the surface of the waveguide that causes a very low interaction with the corrugated sidewall of the waveguide. So, this produces very narrow stop band region that too found for the significantly large number of grating periods [131]. In the design of the grating waveguide, the phase matching condition needs to be verified that also corresponds to an evaluation of the grating period (Λ). The expression is $\Lambda = \frac{\lambda_B}{2 \cdot n_{eff}}$, where λ_B is the Bragg wavelength and n_{eff} is the average value of the effective refractive index of the waveguide layers (Figure 5.1.1). Since the value of the Λ depends on the value of the effective refractive index. The Λ is lower for TE mode than that of the

TM mode waveguide, hence the overall length of the grating waveguide is also less for TE mode operated grating waveguide [46,63,85].

The evaluation of transmission spectra of the structure (Figure 5.1.2) is evaluated by a method discussed in section 5.1.1. The considered value of the propagation loss is 3 dB/cm [63,132]. The device consists of three segments, first and the second segment of the device consist of grating waveguides with the corrugation width of ΔW_1 and ΔW_2. The number of the grating in individual segments are N = 375. Based on the results shown in Figure 5.1.3, it is found that the individual grating waveguides provide the stop band in the range of (1.53459 – 1.54452) µm for ΔW1 (Fig. 5.1.2 (a)) and (1.54288 – 1.55021) µm for ΔW2. The transmission spectra of the overall device show the band gap region of (1.53459 – 1.55021) µm which is greater than the band gap found for the individual grating waveguides. The various geometric parameters of the structure are listed in Table 5.1.1. The corresponding matrix representation based on equation (5.1.4) is, $M = (M_{BG1})^N \cdot (M_{BG2})^N$.

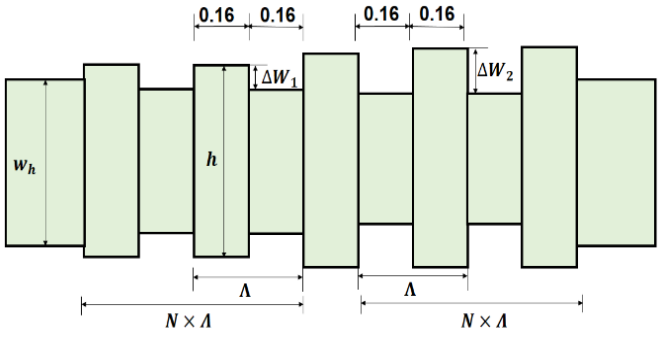

(a)

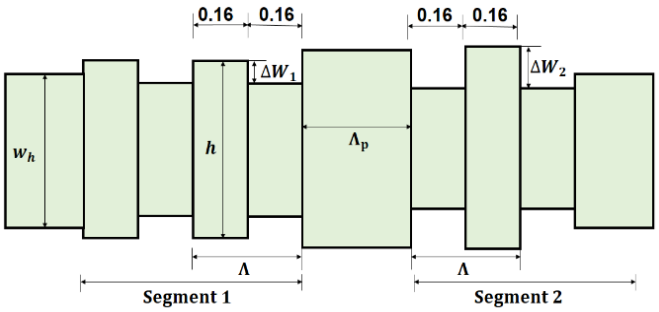

(b)

Figure 5.1.2: Cascaded grating waveguide with (a) corrugation widths of ΔW_1 and ΔW_2, and (b) with a cavity defect

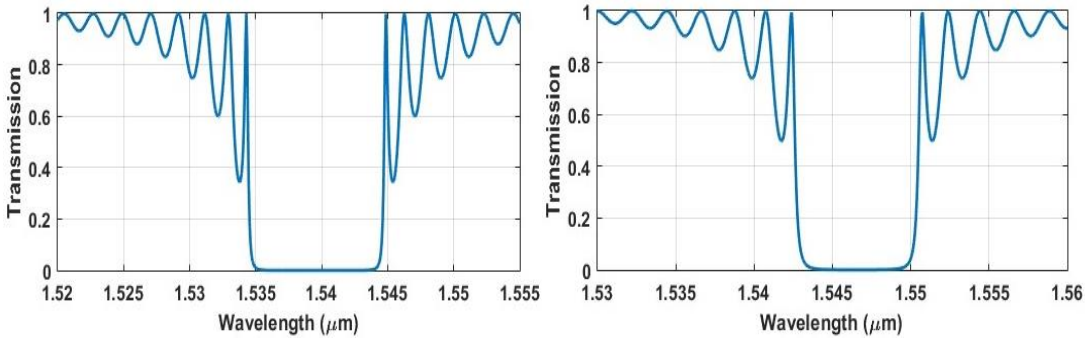

(a) (b)

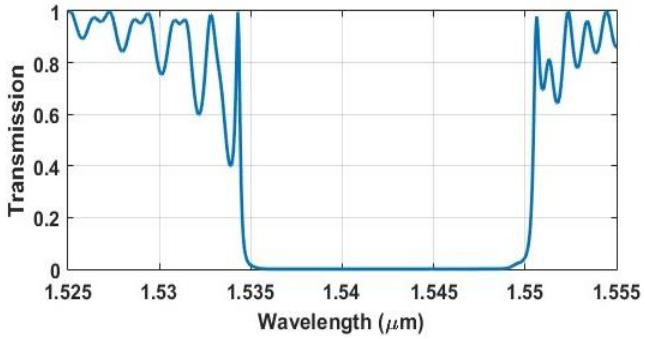

(c)

Figure 5.1.3: Individual transmission spectra of the grating waveguide (a) Segment 1, (b) Segment 2, and (c) Cascaded waveguide

Table 5.1.1: Geometric parameters of the structure shown (Figure 5.1.2)

Parameters	Value
$\mathbf{w_h}$	0.50 µm
h	0.52 µm
Λ	0.32 µm
$\mathbf{\Delta W_1}$	0.04 µm
$\mathbf{\Delta W_2}$	0.06 µm
$\mathbf{\Lambda_p}$	0.34 µm
N	375

Out of the three segments, the third segment represents defect cavity of length Λ_p shown in Figure 5.1.2 (b). The insertion of the cavity in between the two grating waveguide, provides a sharp resonant peak at the centre of the stop band region. The modified matrix representation is, $M = (M_{BG1})^N \cdot M_{cavity} \cdot (M_{BG2})^N$, where the calculation of the M_{cavity} is considered by homogeneous waveguide segment.

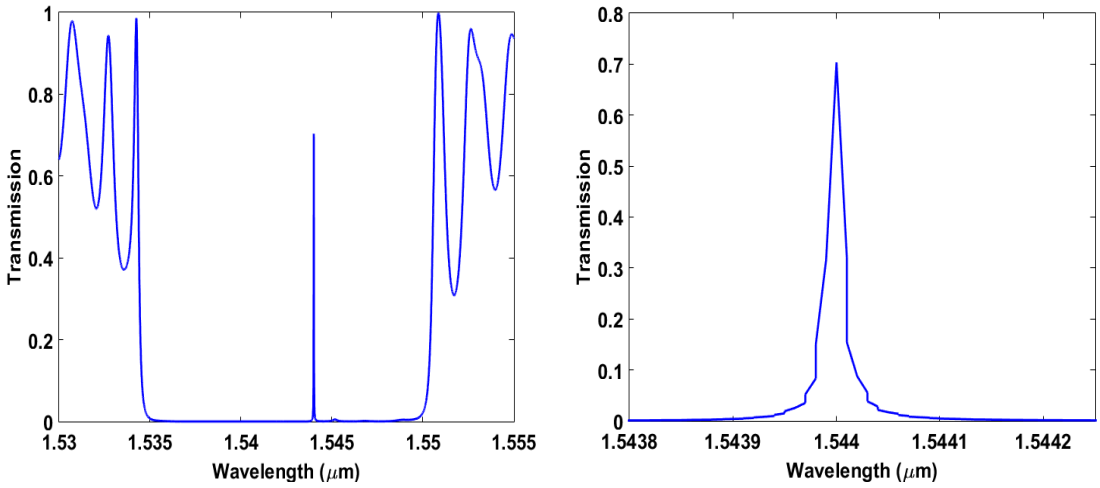

(a) (b)

Figure 5.1.4: Transmission spectra of the complete structure with a cavity defect, (b) zoomed version of the resonant peak

Transmission spectra of the full device are shown in Figure 5.1.4 with the zoomed version of the resonant wavelength. The spectacular sharp resonant peak and $\Delta\lambda_{FWHM}$ (half-width maximum width) have found at 1.544 microns and 0.01 nm. The measured quality factor (Q-factor) on this basis is 1.544×10^5, which is very high and can be utilized for applications such as multiplexing and sensing.

5.1.3 Bio-Sensing Characteristics

On continuation with the above analysis, we have evaluated the capacity of the device for the biosensing application. The microfluidic framework responsible for supplying biomaterials to the surface of the sensor is considered in the top part of the structure, which is the upper cladding region. The highly sensitive device requires larger variation in the effective index of a waveguide for a change in refractive index of a biomaterial. In this work the considered biomaterial are distilled water (RI = 1.33), Hemoglobin (RI = 1.38), Biotin-Streptavidin (RI = 1.45), and Bovine Serum Albumin (RI = 1.47).

For a change in biomaterial, significant shift in the resonant wavelength (λ_{res}) has observed in the spectra as shown in Figure 5.1.5 (a). The Figure 5.1.5 (b) represents the linear relationship between the resonant wavelength and n_c. From the graph, it is observed that the resonant wavelength shifted from 1554.02 at n_c = 1.33 to 1556.13 at n_c = 1.47. The performance parameters of the photonic biosensors are sensitivity and limit of detection. The sensitivity is defined as, $S = (\Delta\lambda_{res}/\Delta n_c)$ where $\Delta\lambda$ represents a shift of resonant wavelength and it is evaluated from the slope of Fig. 5.1.5 (b). The limit of detection (Δn_{min}) is the minimum possible resolution of the n_c required to get the observable shift of resonant wavelength. The evaluation of various parameters has performed by considering the equation (2.9.3). The theoretically calculated value of sensitivity is 90 nm/RIU. The normalized sensitivity is found out to be 0.0583 /RIU with a LOD of 1.1184×10^{-4} RIU.

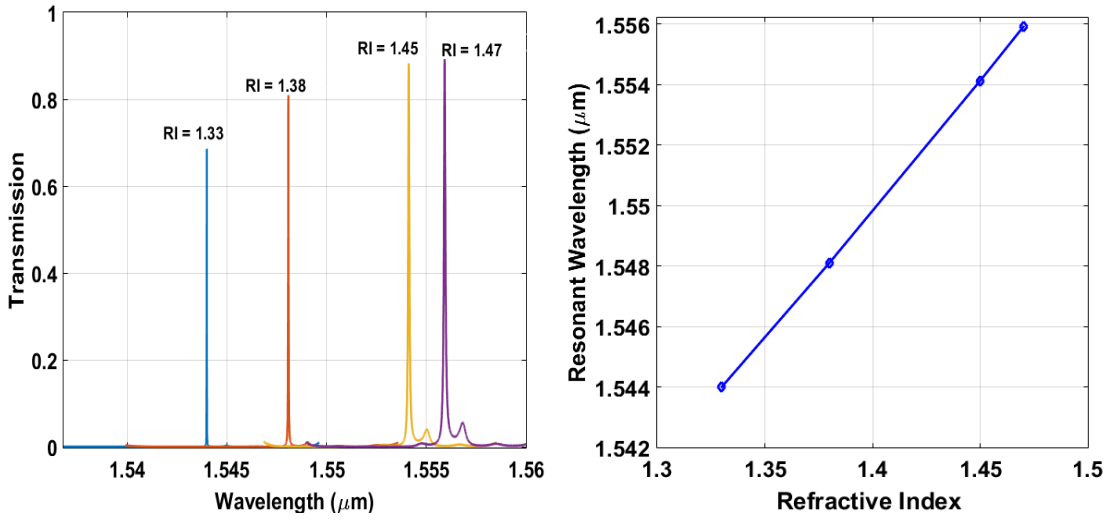

(a) (b)

Figure 5.1.5: (a) Transmission spectra, (b) resonant wavelength shifts as a function of the change in refractive index

5.1.4 Temperature dependence of structure

The materials have a significant impact due to environmental index changes, which can also change the optical characteristics of the device. However, it does not mean that it affects the work of the photonic structures. For improving the consistency of the designated device, some practical factors required to be considered. Most biological fluids have a significant proportion of water. It is the main component present in blood plasma, extracellular fluid, etc., so it seems to be necessary to study the effect of changes in temperature of water on the designed photonic sensor. Based on the previously reported literature it is found that the wavelength and temperature dependent refractive index of water can be found according to the equation (5.1.5) [133].

$$n(\lambda, t) = A(t) + \frac{B(t)}{\lambda^2} + \frac{C(t)}{\lambda^4} + \frac{D(t)}{\lambda^6} \qquad (5.1.5)$$

where λ= 1550 nm is the wavelength of light.

$$
\begin{aligned}
A(t) &= 1.3208 - 1.2325 \times 10^{-5}t + 1.8674 \times 10^{-6}t^2 + 5.0233 \times 10^{-9}t^3 \\
B(t) &= 5208.2413 - 0.5179t - 2.284 \times 10^{-2}t^2 + 6.9608 \times 10^{-5}t^3 \\
C(t) &= -2.5551 \times 10^{8} - 18341.336t - 917.2319t^2 + 2.7729t^3 \\
D(t) &= 9.3495 + 1.7855 \times 10^{-3}t + 3.6733 \times 10^{-5}t^2 - 1.2932 \times 10^{-7}t^3
\end{aligned}
\tag{5.1.6}
$$

where t (^{o}C) is the temperature.

In this work, we have considered the temperature range 18 ^{o}C to 34 ^{o}C in which water molecules exist in the biomaterials. From the Figure 5.1.6, it is observable that the water has a negative temperature coefficient that decreases its refractive index and hence the device has varied resonance wavelength.

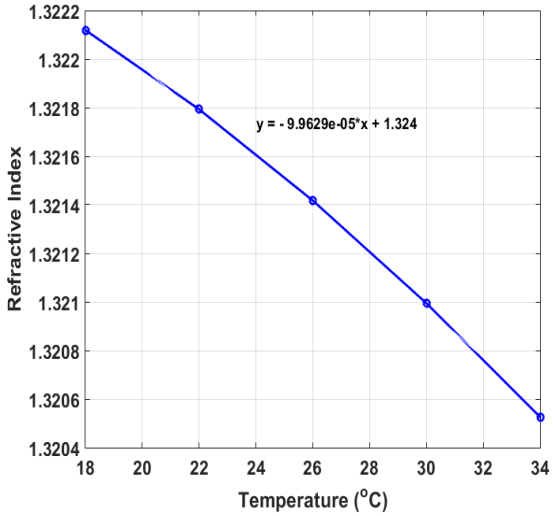

Figure 5.1.6: Change in refractive index due to change in temperature

In Figure 5.1.7(a) the shift in a resonant wavelength corresponding to temperature variation is shown. An almost linear behavior of the relationship has plotted in Figure 5.1.7(b) and the evaluated temperature sensitivity is found out to be -0.0075 nm/^{o}C that clearly indicates only 0.12 nm wavelength shift in the specified temperature range.

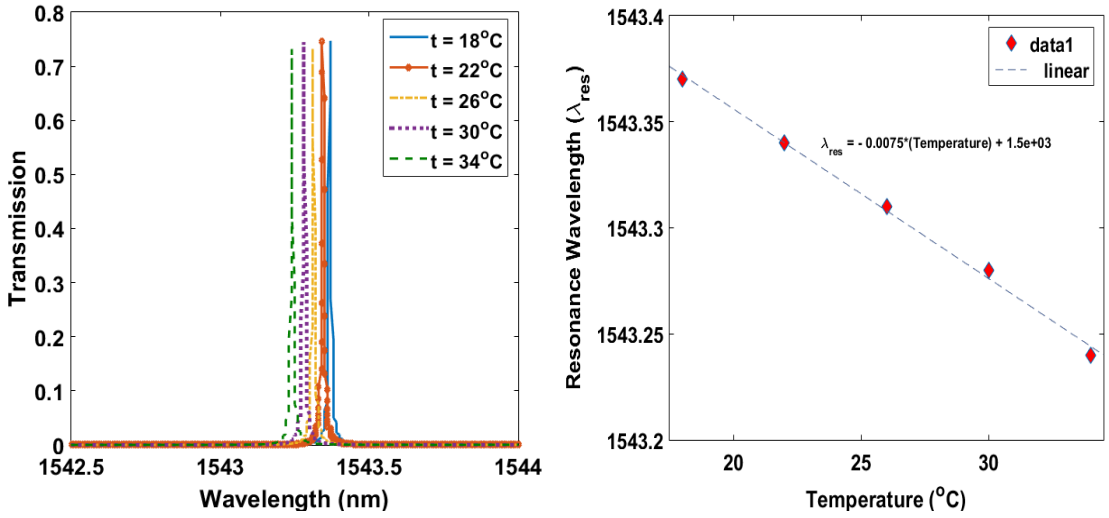

(a) (b)

Figure 5.1.7: (a) Transmission spectra for a change in temperature, (b) shift in resonant wavelength (in terms of nm) due to change in temperature

Table 5.1.2: Value of refractive index and resonant wavelength for variation of temperature

Temperature (°C)	Refractive Index	Resonant Wavelength (nm)
18	1.3221	1543.37
22	1.3218	1543.34
26	1.3214	1543.31
30	1.3210	1543.28
34	1.3205	1543.24

Table 5.1.2, presents the refractive index and resonant wavelength corresponding to a change in temperature. The proposed structure is simpler to design and can be fabricated by conventional CMOS fabrication facility and can be suitable for a lab-on-chip integration.

5.2 Cladding Modulated Grating (CMG) Waveguide

We have proposed a photonic biosensor based on a cladding modulated grating waveguide comprising of the three channels on the silicon-on-insulator (SOI) platform. In this configuration, the optical mode is propagated in the center channel and only small fraction presents outside it. Hence, the outer channels have a very low interaction with the propagated mode. Gratings are designed in the outer channels to provide the periodic perturbation in the effective index, which causes the narrow stop band in the spectra. The analysis of the structure is performed through the eigenmode expansion (EME) method (Sec. 3.5), and the parameters are optimized to get a narrow stop band. The principle of sensing is based on the shift in resonant wavelength for a change in refractive index of a biomaterial. For an extremely sensitive biosensor, higher level of illumination on the surface is required to enhance light-biomaterial interaction, which is accomplished by adopting the thinner waveguide. The structure is evaluated for three-waveguide thickness (220 nm, 150 nm, and 100 nm). The sensor structure with a 100 nm thickness has a higher sensitivity 322.96 nm/RIU with a limit of detection of the order of 1.03×10^{-4} RIU. A designed sensor is easy to fabricate using existing CMOS fabrication facility and can be used for an application of lab-on-chip devices.

The proposed CMG waveguide structure is designed to control the grating coupling coefficient by placing two narrow strip waveguides on both sides of the central core waveguide with gratings on their sidewalls [134–136]. This configuration has the flexibility of choosing a low loss central waveguide, which has enough length to accommodate the number of gratings that is required for narrow band reflectivity. The overall goal is to obtain a biosensing device that is highly sensitive, easy to fabricate using CMOS facility, and can be easily integrated with LOC applications. Here, it is also shown that employing the thinner waveguide increases the presence of optical field on the surface that results in an increasing value of the sensitivity. The organization of this work is as follows, and Sec. 5.2.1 presents the theoretical modeling of the proposed structure with the alteration of the various design parameters, Sec. 5.2.2 represents the evaluation of the biosensing characteristics followed by summary in Sec. 5.2.3.

5.2.1 Modeling of a Cladding Modulated Grating (CMG) Waveguide

The confinement of the field in the CMG waveguide is in the center core region for the fundamental quasi-TE mode. The structure utilizes SOI platform, and it is placed in between the upper cladding and substrate region both having a thickness of 2 µm and a refractive index of 3.47. The waveguide is drawn using Si material (refractive index 1.444) having a thickness (GH) of 220 nm. Initially, the modal calculation is performed using the full vector based Eigen-mode calculation method.

Figure 5.2.1 (a) and (b) schematically represents the proposed structure of the CMG waveguide consists of a central core waveguide having a width of 500 nm and two other waveguides (side channels) of width, SC = 80 nm, separated by gap width (GW). The both channels have the number of gratings of width ΔW on one side of their sidewalls. The high index contrast between the materials of waveguide and cladding enabled the confinement of the mode in the central core region, and only small fraction of the optical-field (trailing edge of the evanescent field) present outside it, which is interacting with the outer side channels as shown in Figure 5.2.1 (c). This structure is especially compelling because the corrugation in the outer channel provides lower effective index difference between the grating and non-grating region thus provides a weaker coupling strength and hence can provide a narrow stop band [136].

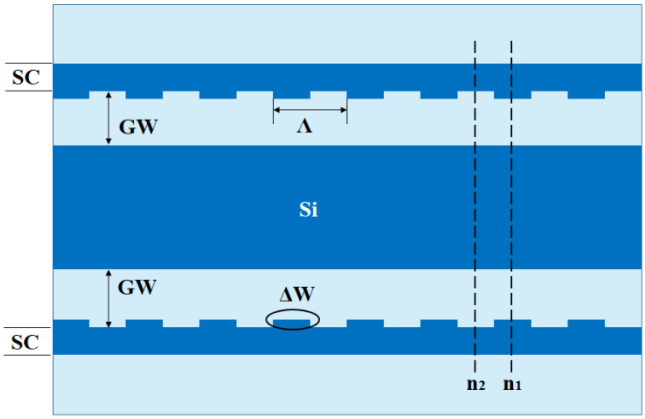

(a)

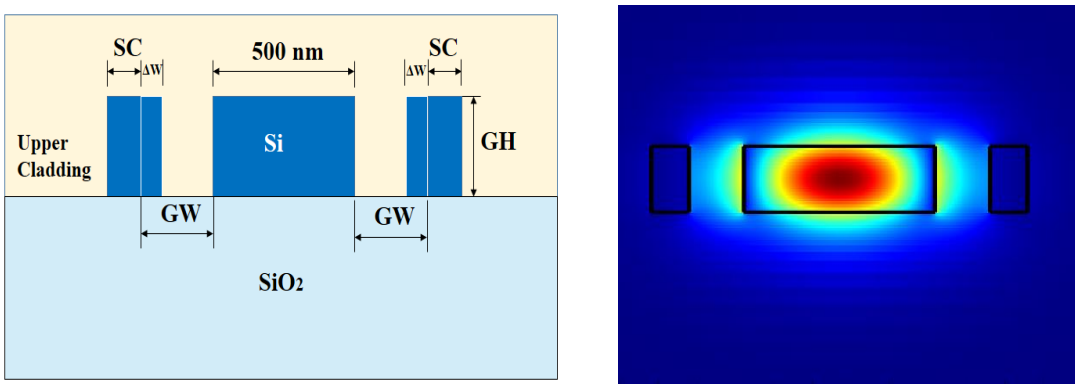

(b) (c)

Figure 5.2.1: (a) Schematic of the cladding modulated grating waveguide, (b) cross-sectional view of the structure, and (c) optical mode in a waveguide

In Figure 5.2.1 (a) for a 20 nm corrugation width (ΔW), the effective index difference is around ~0.003, which is very low. The grating period (Λ) is calculated by considering the phase matching condition given as, $\lambda_B = 2 \cdot \Lambda \cdot n_{eff}$, where n_{eff} is the average value of effective refractive index n_1 and n_2. The calculated value of the mode refractive indices are n_1 = 2.442221 and n_2 = 2.439270 for GW = 100 nm. So the calculated value of Λ is ~317 nm to get a stop band at around 1550 nm wavelength, but for the sake of reducing fabrication variability we consider Λ = 320 nm. The complete device is simulated using eigenmode expansion (EME) method [113], it is a bidirectional method, work well in the frequency domain. The EME is based on the discretization of the invariant propagation direction. In this method, the complete structure is divided into N number of non-varying substructures, the modal calculation at each substructure form a basis set, which is used further for an evaluation of the mode matching analysis at the interface between the adjoining substructures. At the interface, the tangential continuity of the field components provides the transmission/reflection between substructures. The algorithm utilizes scattering matrix method to join different sections of the structure [113,137].

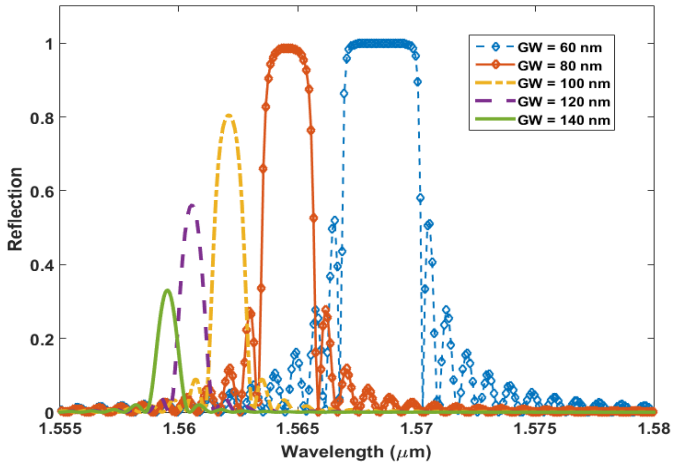

Figure 5.2.2: Reflection spectra of the CMG waveguide for a variation in gap width (GW)

The simulated reflection spectra for a number of grating periods, N = 1000 is shown in Figure 5.2.12. It is observed that a significant shift in reflection spectra is found for a variation of the GW. The reflection band becomes narrower on increasing the value of the GW, however, the value of reflectivity goes on decreasing for a fixed value of N. The value of $\Delta\lambda_{-3dB}$ (full width at half maxima) for GW = 60 nm is 3.3 nm and it varies to a 0.8 nm for GW = 140 nm. This shows that almost 4 times decrease in bandwidth for increasing GW. It is also evident that for increasing the reflectivity, the number of grating should be increased. The Figure 5.2.3 plots the relationship between peak reflectivity and the number of gratings (N). The value of reflectivity goes on increasing continuously for the higher value of N, at the same time it is also seen that the value of $\Delta\lambda_{-3dB}$ decreases. For the range of N = 2000 to 2500, $\Delta\lambda_{-3dB}$ almost becomes constant with an increasing value of reflectivity. But for higher GW value the value of reflectivity becomes very small due to very weak interaction between the field and gratings. Hence for the rest of our work we have considered the value of GW = 140 nm and N = 2000 that gives the reflectivity value of ~0.8 and $\Delta\lambda_{-3dB}$ = 0.39 nm.

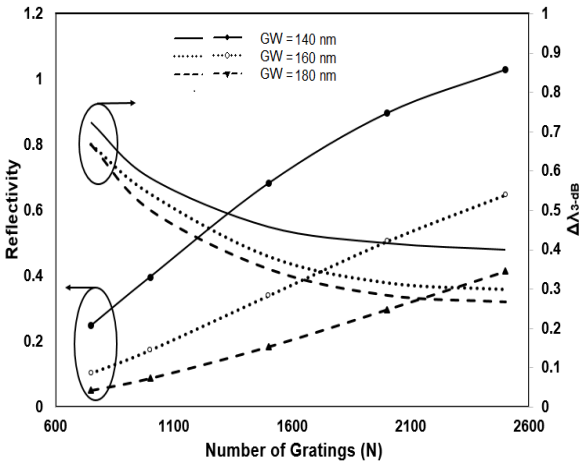

Figure 5.2.3: Reflectivity and $\Delta\lambda_{-3dB}$ for variation in GW

5.2.2 Biosensing Characteristics of CMG waveguide

From the Figure 5.2.1 (c), it is easily observable the major portion of the signal propagating in the core of the waveguide and only small fraction lie on its surface. However, for an evanescent type of the photonic biosensor, higher change in effective index of the waveguide (dn_{eff}) is required for a small change in refractive index of a biomaterial (dn_c). The higher value of dn_{eff}/dn_c is desired for higher sensitivity [16]. The use of thinner waveguide increases the presence of field on the surface of the waveguide. The theoretical proof of the concept is provided in [13–15]. Apart from that the study regarding an increase in the sensitivity to homogenous biomaterial layer is also provided [13]. The ultra-thin waveguide (thickness < 100 nm) based ring resonator for biosensing application is proposed by Sahba et.al. [16]. They have achieved a sensitivity of 100 nm/RIU and a LOD of 5×10^{-4} RIU for 90 nm thin waveguide. Thinner waveguide (thin silicon core) based biosensors also provide the possibility of better thermal stability. The Si and SiO_2 (core and substrate material) have a positive temperature coefficients [138], and the water in upper cladding have negative temperature coefficient [133], thus the increase presence of field to the cladding region causes a decrease in the impact of temperature on the effective refractive index of the optical mode.

As demonstrated in this work the performance parameter determines the resonant wavelength. So the sensitivity (S) is defined as the change in the resonant wavelength (λ_{res}) according to an alteration in the refractive index of biomaterial (n_c) [46]. Another important biosensing parameter is the LOD, which gives the value of the minimal change in refractive index required for shifting the resonant wavelength, and it is given as, LOD = ($\Delta\lambda_{min}$/S) where $\Delta\lambda_{min}$ is one fifteenth of ($\Delta\lambda_{-3dB}$) [46,85]. The lower value of LOD is required for an efficient biosensor that can be accomplished through two conditions either having a narrow resonating band in the transmission spectra (high Q factor, (λ_{res}/ $\Delta\lambda_{-3dB}$)) or a higher value of sensitivity. In the proposed structure, high Q resonating band is difficult to achieve, so we rely on increasing the value of the sensitivity.

Before analyzing the resonator structure based on CMG waveguide, we have investigated the value of dn_{eff}/dn_c for a cross-section of a waveguide shown in Figure 5.2.1 (b) for different values of thickness (GH). For these calculations, refractive index change of 0.01 RIU (refractive index unit) has assumed and biomaterial having a refractive index of 1.33 has considered in the upper cladding. The value of dn_{eff}/dn_c for three thickness values 220 nm, 150 nm and 100 nm is found out to be 0.153, 0.247, and 0.374 respectively. The corresponding modal field confinement is shown in Figure 5.2.4.

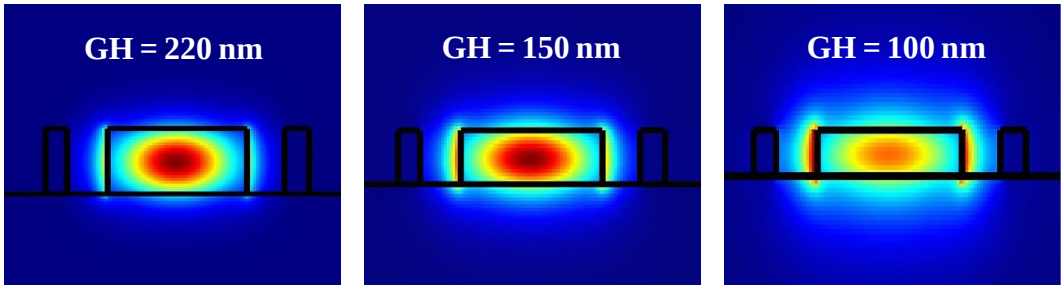

Figure 5.2.4: Optical mode confinement in the standard and the thinner waveguide

Figure 5.2.4 represents the modal field confinement in the waveguide. The confinement of field in the core region is more for the GH = 220 nm and its presence is getting on decreasing for lower values of GH. The GH = 100 nm have the higher presence of evanescent field on the surface of the waveguide. The effect of decreasing the GH also

affects the waveguide effective index and hence requires a change in the value of a grating period (Λ). The evaluated value of Λ, for a GH = 150 nm is 370 nm, and for GH = 100 nm is 440 nm. By considering the following evaluated values of Λ we have designed the CMG waveguide, and the similar procedure which is discussed in section 5.2.1, is followed by getting the narrow stop band.

The Figure 5.2.5 (a) and (b), represents the reflection spectra of the CMG waveguide for GH values. The resonant wavelength continuously shifted to lower values for increasing the value of GW, and $\Delta\lambda_{-3dB}$ decreases on increasing the value of GW. In addition, the value of reflectivity keeps on decreasing for the higher value of GW. Therefore, it is important to select the parameters that have sufficiently high reflectivity and lower $\Delta\lambda_{-3dB}$. In Figure 5.2.5 (a), it is depicted that the narrowband of around ~0.48 nm is found for GW = 180 nm and its value slightly varies on further increase the value of GW. Similarly, the Figure 5.2.5 (b) provides the narrow band ~0.51 nm for GW = 240 nm. For both the variations of GH, the number of grating periods (N) considered is 1500.

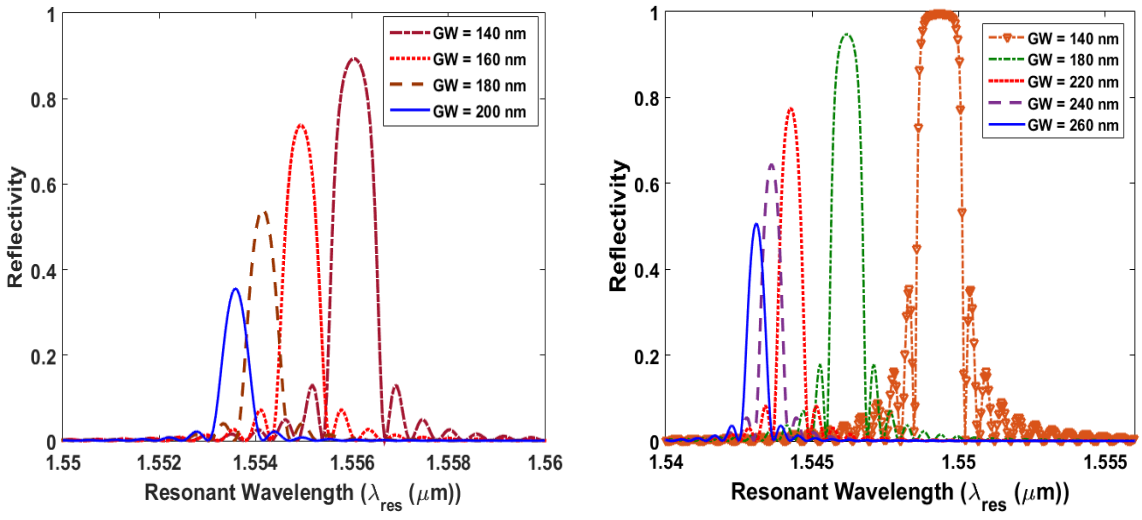

(a) (b)

Figure 5.2.5: Reflection spectra for (a) GH = 150 nm, and (b) GH = 100 nm for a variation in GW

The biosensing parameters are evaluated by considering the configuration mentioned above of the CMG waveguide. For further reference the biosensors based on the GH 220 nm, 150 nm, and 100 nm, they are designated as Design A, B and C. The parameters used in designing the sensors are listed in Table 5.2.1.

Table 5.2.1: Parameters for Design A, B and C

Design	**GH**	**GW**	**Period (Λ)**	**N**
Design A	220 nm	140 nm	320 nm	2000
Design B	150 nm	180 nm	370 nm	1500
Design C	100 nm	240 nm	440 nm	1500

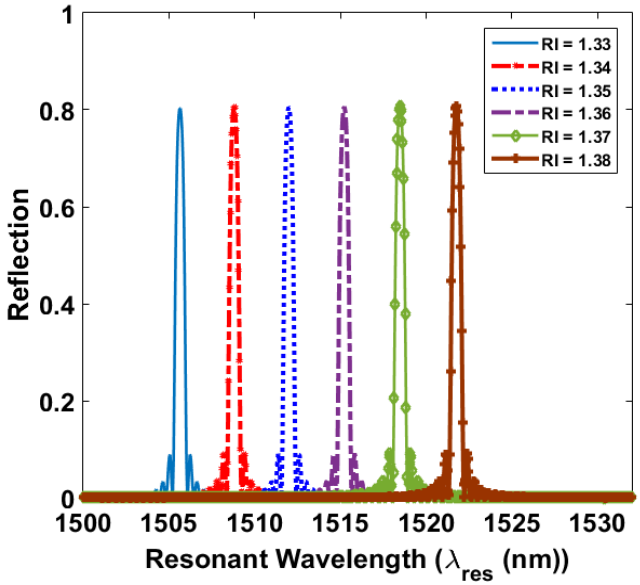

Figure 5.2.6: Output reflection spectra for the proposed sensor with a variation in refractive index of a biomaterial

To facilitate investigation of the reflectance spectra, the microfluidic framework (upper cladding) is considered to vary with the biomaterials having refractive index changes from

1.33 to 1.38 in steps of 0.01. The simulated reflection spectra for Design C is shown in Figure 5.2.6. The resonant wavelength is calculated for each biomaterial. The shift in λ_{res} of around 3.2 nm is found for a change in refractive index of a biomaterial.

The variation in resonant wavelength (λ_{res}) for change in refractive index, and corresponding values of sensitivity is shown in Figure 5.2.7 (a) and (b). It is easily observable that a resonant wavelength is shifted to a higher value for increasing the value of refractive index of the biomaterials. The slope of Design C is more than of other designs which are due to the stronger interaction between the evanescent field and biomaterial (higher value of dn_{eff}/dn_c). The corresponding value of sensitivity is plotted in the form of a bar in Figure 5.2.7 (b) and found that the Design C has a higher sensitivity of 322.96 nm/RIU and Design A has a lower value of 84.34 nm/RIU.

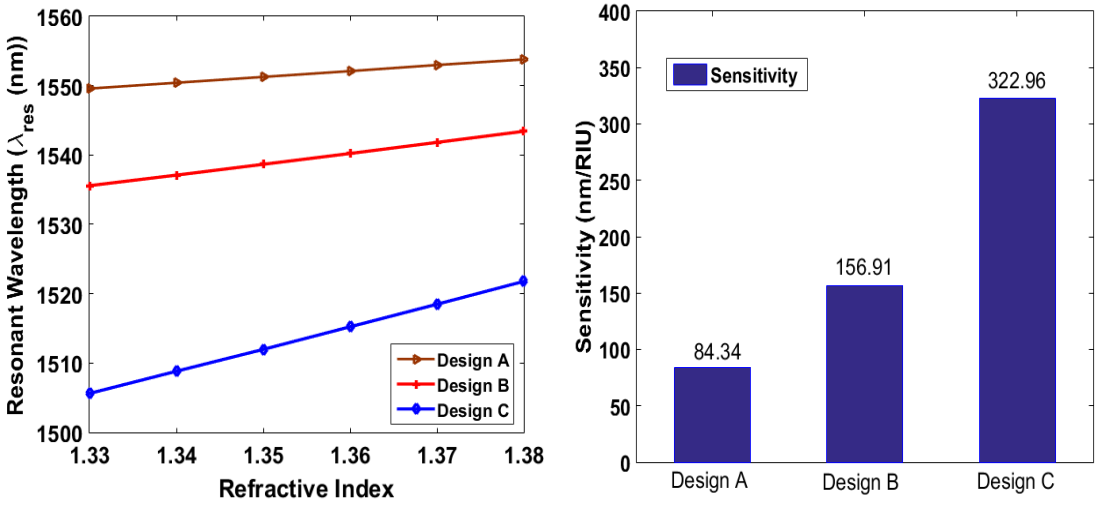

(a) (b)

Figure 5.2.7: (a) Resonant wavelength shift, and (b) sensitivity of proposed designs for a variation in refractive index of biomaterial ranges from 1.33 to 1.38 in steps of 0.01 RIU

The bandwidth ($\Delta\lambda_{-3dB}$) for Design C is 0.51 nm. Hence, the theoretically evaluated value of LOD is 1.05×10^{-4} RIU. The same value of LOD can be found by using expression

provided in [85] which is expressed in terms of dn_{eff}/dn_c given as, $\mathrm{LOD} = \Delta\lambda_{\min}/\left(2 \cdot \Lambda \cdot \left({}^{dn_{eff}}/_{dn_c}\right)\right)$. With this expression, the LOD is 1.03×10^{-4} RIU.

5.2.3 Summary

In this work, photonic biosensors have been studied based on the cascade grating waveguide and cladding modulated grating waveguide. The designed structure is easy to fabricate by using the conventional CMOS facility. Insertion of the cavity in between the two segments of the grating waveguides provides a narrow resonant peak of the high Q factor of the order of 10^5. The realization of the sensor is performed by observing wavelength shift, and almost linear dependence has been found between the resonant wavelength shift and bio-material refractive index change. The impact of temperature on biomaterials present on the surface of the sensor is also studied. The result shows 0.12 nm resonant wavelength shift in the temperature range of 34 ^{o}C of 18 ^{o}C. The proposed sensor is compact in size and can be used for an application of the lab-on-chip for the simultaneous detection of several biomaterials.

In the second part of the chapter, the cladding-modulated grating waveguide structure is evaluated for biosensing application. The structure strategies are used to lower the interaction between the propagating optical mode and the gratings. A biosensor working principle is based on an observation of a shift of resonant wavelength for a change in refractive index of a biomaterial. The functionality of the waveguide is evaluated through an EME method. Parameters are also optimized for getting the narrow stop band. For a three-waveguide thickness (220 nm, 150 nm, and 100 nm) the biosensing capability is evaluated. It is found that the sensor with a 100 nm thickness provides a higher sensitivity of 322.96 nm/RIU and the limit-of-detection of the order of 10^{-4} RIU. The device is compatible to fabricate with an existing CMOS fabrication facility and can be suitable for lab-on-chip applications.

In the next chapter, the slot waveguide is utilized for a straight resonating structure. The light confinement in the slot waveguide is in the low refractive index slot region. The

geometric parameter are adjusted, and the resonating structure based on single and dual slot waveguide is discussed. The direct interaction of the propagating optical mode with the biomaterial causes an increase in the sensitivity.

Chapter 6

Resonator based on gratings in slot waveguide

In the previous chapter, we have discussed the resonating structure based on the strip waveguide. Both the proposed devices requires large number of gratings that increase the dimension of the waveguide. In this chapter, we have implemented a grating resonator for a slot waveguide, which have various features such as increased light matter interaction, smaller number of gratings required, and wide stop band region. This chapter consist of the design artifacts of the two module of the slot waveguides, which is based on the single and dual slot waveguides.

6.1 Grating slot waveguide for refractive index sensor

The lower light matter interaction in the planar strip waveguide is occurred due to the smaller presence of the evanescent field on the surface of a waveguide. It is also evident that the higher light matter interaction causes higher sensitivity of detection. Therefore, we have explored the slot waveguide, which have higher fraction of field present in the slot region of the waveguide. Then the symmetrical sidewall gratings are designed to analyze the resonating structure for biosensing applications.

Before the design of grating in a slot waveguide, slot width and channel widths are optimized to get the desired output performance of a sensor. Figure 6.1.1 (a) presents the design of the device that consists of gratings in the slot waveguide. Simulation has been performed by considering silicon refractive index 3.47 in the parallel channels of the slot waveguide having width and thickness of 500 nm and 220 nm respectively. Silica substrate (lower cladding) of refractive index 1.444 is considered below the waveguide core having a thickness of 2 μm that is wide enough to isolate coupling of the core signal with a lower silicon substrate. The parameter of the devices is listed in Table 6.1.1.

Table 6.1.1: Design parameter used in grating slot waveguide

Parameters	Values
S	100 nm
W1	350 nm
W2	370 nm
ΔW	20 nm
Λ	320 nm
Number of gratings (N)	65

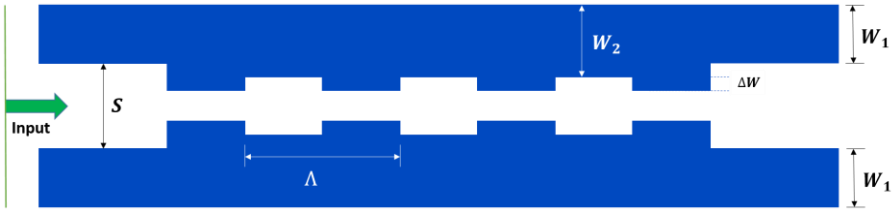

(a)

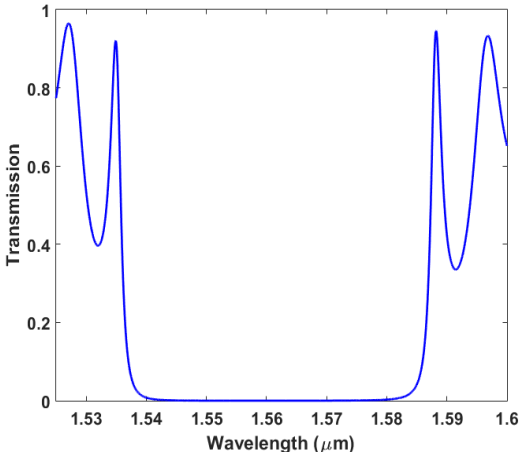

(b)

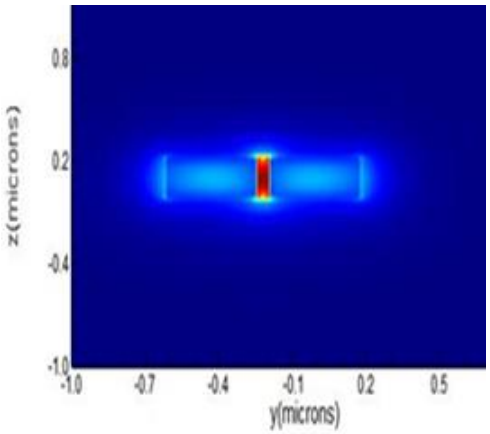

(c)

Figure 6.1.1: (a) Top view of the grating slot waveguide, (b) transmission spectra, and (c) electric field confinement in the slot region

The wideband signal propagates in a structure. Figure 6.1.1 (b) presents transmission spectra of a grating slot waveguide, it shows a wide stop band of (1.588-1.536) μm. The prime concentration of electric field lies in the slot region as shown in Figure 6.1.1 (c).

6.1.1 Sensor Design

The proposed sensor detects a shift in resonant wavelength for change in the refractive index of a biomaterial. For inducing a resonant wavelength, the additional phase shift is required to create at the center grating of a waveguide [60,85,139]. Hence, the design of the sensor is divided into two parts; first part consist of the gratings in a planar slot waveguide and the second part consist of the phase shift cavity. The cavity produces a phase change that is required to confine a narrow band in the cavity. The length of the cavity is Λ_{cavity}, the dimension is calculated using the expression $\Lambda_{cavity} = \lambda_B/(4 \cdot n_{eff})$ [46]. The complete sensor design is shown in Figure 6.1.2. The size of a slot (S) is 100 nm for high light confinement and is considered to be filled with the biomaterial having a refractive index (n_c) 1.33.

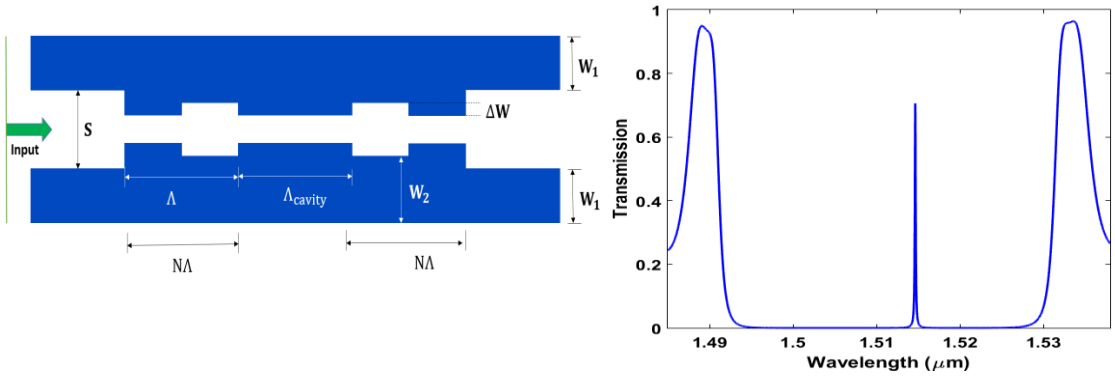

(a) (b)

Figure 6.1.2: Grating slot waveguide with a cavity defect

Analytical modeling of the device is performed through transfer matrix method and the methodology discussed in [60] is considered for the evaluation of the output parameters. Figure 6.1.2 (b) represent the overall transmission spectra of the device with a phase shift

cavity in the grating. A sharp resonant peak is clearly observable at a stop-band, which provide a very high Q factor of 21637. The high Q factor is a critical parameter that is required for quantifying the resonant wavelength shift through the evaluation of the limit of detection.

6.1.2 Result and analysis

The slot-region and upper cladding of the waveguide are provided with biomaterials having refractive indices changes from 1.33 to 1.338, and the overall output transmission spectrum is presented in **Error! Reference source not found.** (a). The shift in the resonant band for corresponding change in the refractive index of the biomaterial is shown in **Error! Reference source not found.** (b). For a refractive index sensor, sensitivity (S) is required to measure that is a ratio of the change in resonant wavelength and the change in the refractive index of the biomaterial. The expression of a sensitivity is provided in equation (2.9.1).

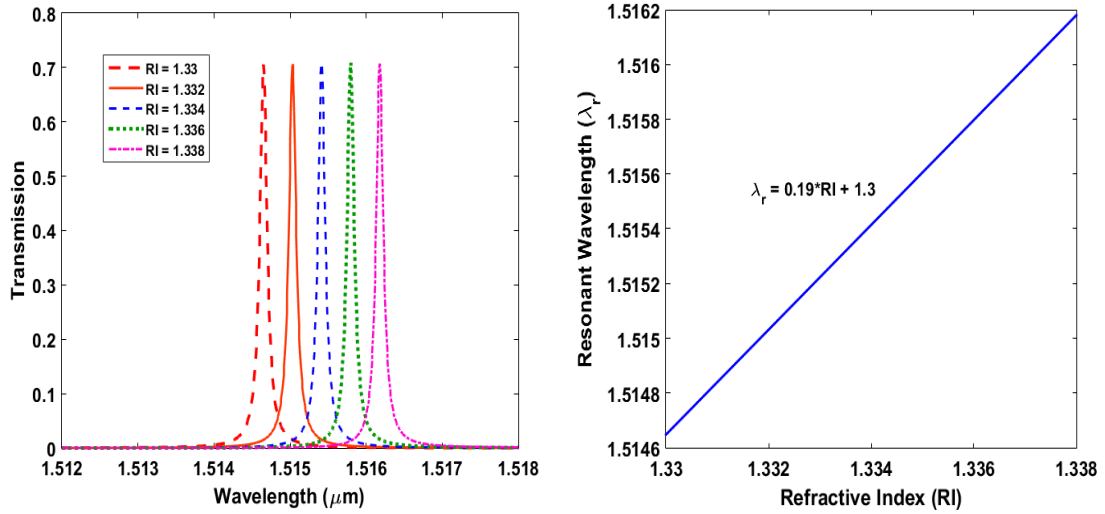

(a) (b)

Figure 6.1.3: (a) Transmission spectra of the structure, (b) shift in the resonant wavelength for a change in n_c (RI of biomaterial)

The value of sensitivity is 0.19 μm/RIU is evaluated from **Error! Reference source not ound.** (b). The minimum possible change in refractive index detected by the sensor is calculated from equation (2.9.3) is 3.684×10^{-4} RIU.

6.2 Inner Side Gratings in Dual Slot Waveguide

The single slot waveguide increases the sensitivity of the device. The aim of this work is to distribute the fraction of the propagated optical field to the dual slot of the waveguide that causes a further increase in the light matter interaction.

In this work, refractive index biosensor based on the sidewall gratings in dual slot waveguide is modeled with a TMM. The waveguide comprised of three parallel channels separated by the nanometer gap. The gratings are designed at the inner side of two outer channels of the dual-slot waveguide. The configuration offers several advantages like the sensitive spectral response, high Q resonating band, reduction in the out-of-plane scattering loss. From our knowledge, this configuration is used first time for the application of refractive index biosensor, which provides the higher sensitivity and limit of detection in the order of 10^{-6} RIU.

6.2.1 Optimization of dual-slot waveguide for refractive index biosensor

Biosensors based on a low index guided waveguides provides higher sensitivity due to its nature of confinement of field in low refractive index region which is mediated in between rails of two high index region [13]. Target biomaterial present in a slot region allows maximum interaction between the biomaterial and the modal field. In this section the theoretical analysis of the dual-slot, waveguide is present for biosensing application. The dimension of the waveguide is optimized for maximizing the resonator bulk sensitivity by varying slot width and center channel width.

(a) Theory and Modeling of Dual-Slot Waveguide Biosensor Structure

In the present work, the performance parameter of a biosensor is bulk sensitivity. The bulk or homogenous sensitivity (dn_{eff}/dn_c) is calculated as a ratio of change in the effective

refractive index of a waveguide to a change in refractive index of a biomaterial present on the upper cladding surface of a waveguide. In Ref. [104], Sahba et. al. considered the effect of dispersion on the shift in resonator wavelength through the consideration of group index (n_g). The group index is directly related to the effective refractive index of a waveguide, hence the dimension of the waveguide is required to be optimized for an optimum value to enhance the resonator bulk sensitivity. The resonator bulk sensitivity (S) directly related to a dn_{eff}/dn_c and inversely related to n_g given as [104],

$$S = \frac{\lambda_{res}}{n_g}\frac{dn_{eff}}{dn_c} = \frac{\Delta\lambda_{res}}{\Delta n_c} \tag{6.2.1}$$

Analysis of dual-slot waveguide is done by using full-vector 2D Eigen-mode calculation for the solution of fundamental quasi-TE mode. The schematic of a cross-section of the waveguide is shown in Figure 6.2.1 (a). The meshing of the waveguide geometry is performed using finite difference method, and then Maxwell's equations are articulate into an eigenvalue problem to evaluate an effective refractive index and field profile of mode [40]. The silicon (Si) channels with a refractive index of 3.47 at 1550 nm wavelength designed on the SOI platform of thickness, **GH** = 220 nm. The lower cladding material is silicon dioxide (SiO_2) of refractive index 1.444 and the upper cladding material is filled with a water of refractive index 1.326 as targeted biomaterial [11]. In the slot of a waveguide, quasi-TE mode is highly confined as compared to a TM mode. The modal confinement is more in the lower refractive index slot region enhanced a sensor sensitivity to detect a small change in refractive index of a biomaterial. Figure 6.2.1 (b) shows the modal confinement in a dual-slot waveguide.

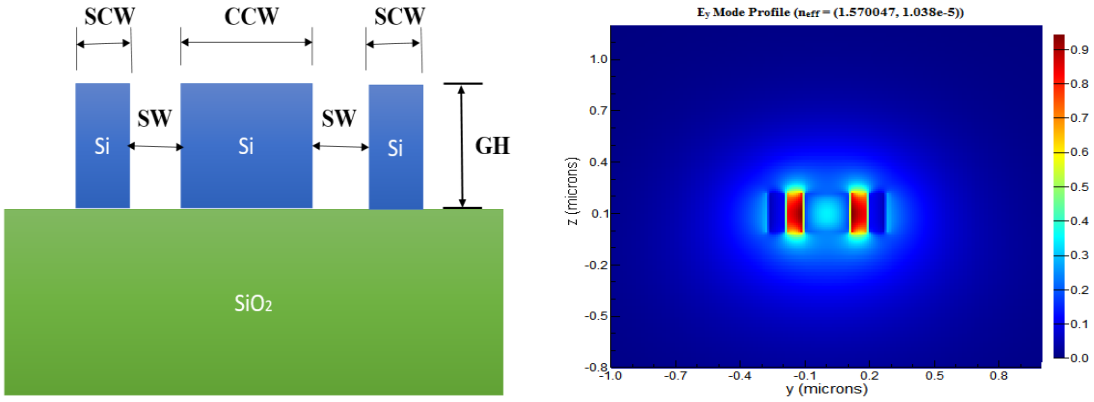

(a) (b)

Figure 6.2.1: (a) Cross-section, and (b) mode profile of a dual-slot waveguide for a center channel width (CCW) of 220 nm

The waveguide consists of two side channels of width, **SCW** and a center channel of width, **CCW**. We have assumed the width of the side channels to keep constant at 80 µm. The width of a center channel is varied from 200 nm to 280 nm for variation in slot width (**SW**) ranges from 60 nm to 140 nm to determine their effect in effective refractive index.

(b) Results and Discussion

Effective index and group index is plotted in Figure 6.2.2 for the various values of **CCW**. Figure 6.2.2 (a) demonstrates how n_{eff} varies corresponds to change in **CCW**, the lower value of n_{eff} on the occasion of increased **SW** is primarily due to the reduction in the coupling of the mode in the slot region [140,141]. The value of n_g is shown in Figure 6.2.2 (b), it is observed that the value approached to a constant value for increase in **CCW** so the sensitivity depends only on the value of dn_{eff}/dn_c.

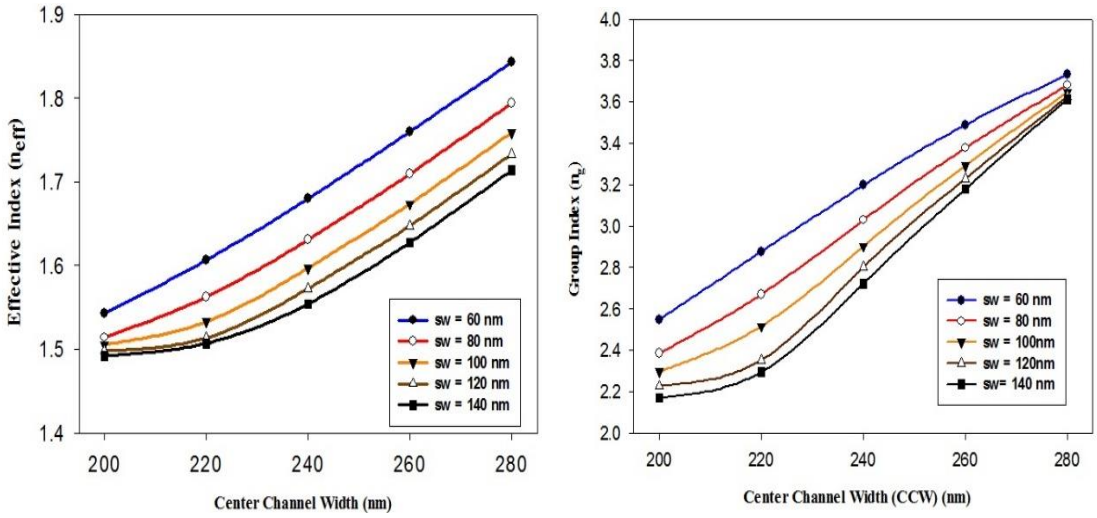

(a) (b)

Figure 6.2.2: (a) Change in the effective index, and (b) group index of a waveguide as a function of center channel width (**CCW**)

Figure 6.2.3, shown the plot of the variation of sensitivity for a change in the **CCW**. The sensitivity is more for **SW** = 60 nm due to increse in the confinement of mode, but smaller **SW** have limitations like difficulty in providing the biomaterial and capillary force in liquid [11], and also the fabrication constraint required to consider due to the occurrence of an unavoidal roughness at such a small dimension causes an additional scattering losses [40]. Therefore the considered value of maximum sensitivity (S) is 461.327 nm/RIU for **SW** = 100 nm. Figure 6.2.2 (a) and (b) represents that the value of effective index and group index increases on increasing the dimension of **CCW**. The increase in the effective index leads to a fact that the confinement of mode in the slot region decreases the sensitivity of the sensor Figure 6.2.3. The optimized dimension for a **CCW** is 220 nm for a **SW** of 100 nm, keeping the value of **SCW** fixed at 80 nm.

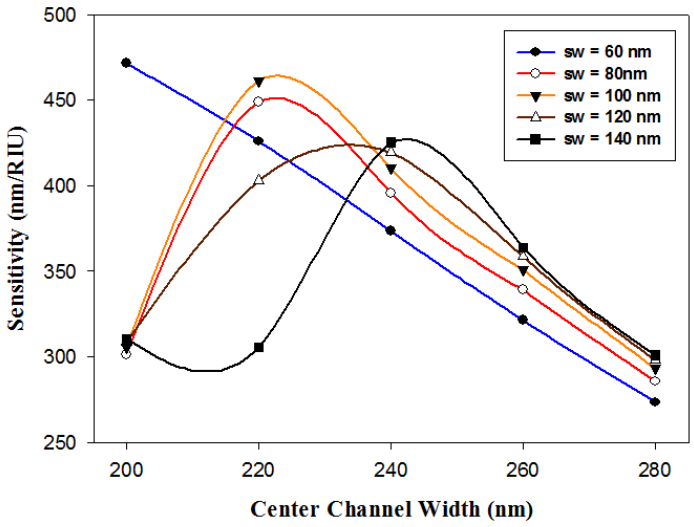

Figure 6.2.3: Sensitivity as a function of center channel width (**CCW**)

(c) Detection Limit of Biosensor

LOD is the small possible change in refractive index require for alteration of the resonance wavelength. It is inversely related to the sensitivity of biosensor, and analytically it is expressed as, LOD = σ/S (where σ is smallest resolvable-signal and S is the sensitivity). We have considered a complete system noise by using three standard deviations (σ) as a measure of sensor resolution [142].

$$\rho = 3\sigma = 1.2 \text{ pm} \qquad (6.2.2)$$

The LOD from (2) is 2.601×10^{-6} RIU. The unit of LOD is refractive index unit (RIU) used for quantification of the biosensor performance and require to compare the photonic biosensor from different structure.

The proposed sensor exhibits a resonator bulk sensitivity of 461.32 nm/RIU and a limit-of-detection of 2.601×10^{-6} RIU. The sensor easily found application for lab-on-chip diagnostics due to the advantages such as compactness, higher sensitivity, and compatibility with CMOS fabrication facilities.

6.2.2 Modeling of Sidewall Grating in Dual Slot Waveguide (DSW)

The DSW confines the field for fundamental quasi-TE mode, the mode field is calculated by using a full vector based Eigen-mode calculation method. SOI platform is used for modeling of a waveguide having refractive indices of Si and SiO_2 are 3.47 and 1.444 respectively. Before the design of the gratings, parameters of the DSW are optimized for the maximum confinement of the field in the slot region. The methodology discussed in [104] is followed by the calculation of the theoretical bulk sensitivity by considering the impact of dispersion on the effective refractive index of the DSW waveguide. The variation of parameters slot width and center channel width is studied for maximizing the sensitivity. The maximum theoretical bulk-sensitivity is found out to be 461.327 nm/RIU.

Figure 6.2.4 (a) represents the modeling of the grating in DSW. The device consists of the three parallel channel separated by the nanometer gap size represented as a slot width (**SW**). The **ΔW** represents the corrugation depth of the grating in the inner side of the outer channels of the waveguide. The grating period is denoted as Λ, Λ_c is the phase shift cavity. The analytical modeling of the structure is performed using Transfer matrix method (TMM) [60]. In the TMM, each segment of the structure is denoted by the 2×2 matrix. The generalized expression of the matrix for the grating segment (M_g) and cavity segment (M_c) is given in eq (1). M_g is calculated by using the parameters grating period (Λ), coupling coefficient (κ), grating length ($L_i = N\Lambda$, where N is the number of grating-periods). Whereas for the M_c, the value of κ and Λ are 0 and infinity respectively. The cumulative matrix representation for the device shown in Figure 6.2.4 is, $M = (M_g \cdot M_c \cdot M_g)$.

$$M_{g/c} = \begin{bmatrix} T_{11} & T_{12} \\ T_{21} & T_{22} \end{bmatrix} = \begin{bmatrix} \cosh(\delta L_i) - j\frac{\Delta\beta}{2\delta}\sinh(\delta L_i) & -j\frac{\kappa}{\delta}\sinh(\delta L_i) \\ j\frac{\kappa}{\delta}\sinh(\delta L_i) & \cosh(\delta L_i) + j\frac{\Delta\beta}{2\delta}\sinh(\delta L_i) \end{bmatrix} \quad (6.2.3)$$

Where $\Delta\beta = 2\left(\beta - \frac{\pi}{\Lambda}\right)$, $\delta = \sqrt{\kappa^2 - \left(\frac{\Delta\beta}{2}\right)^2}$, $\beta = \left(\frac{2\pi}{\lambda}\right) n_{eff} + j\alpha$ is the propagation constant with propagation loss coefficient α.

The dimensions of the parameters for a proposed device is presented in the Figure 6.2.4 (a) and (b). For the evaluation of the grating period phase matching condition needs to be satisfied which is $\lambda_B = 2 \cdot \Lambda \cdot n_{eff}$ where n_{eff} is the average of the n_1 and n_2 [143]. The mode effective indices calculated are n_1=1.633898 and n_2= 1.697135. The calculated value of grating period (Λ) is 464 nm. For the sake of the reducing the complexity during fabrication, the considered value of Λ is 460 nm. The cavity is created by adding the quarter wavelength segment, $\Lambda_c = \lambda_B/(4 \cdot n_2) = 230$ nm at the center grating of the structure. The overall cavity length is calculated as $t + \Lambda_c$. The value of other parameters are t = 230 nm, **SW** = 80 nm, corrugation depth (**ΔW**) = 20 nm and number of grating periods (N) = 120.

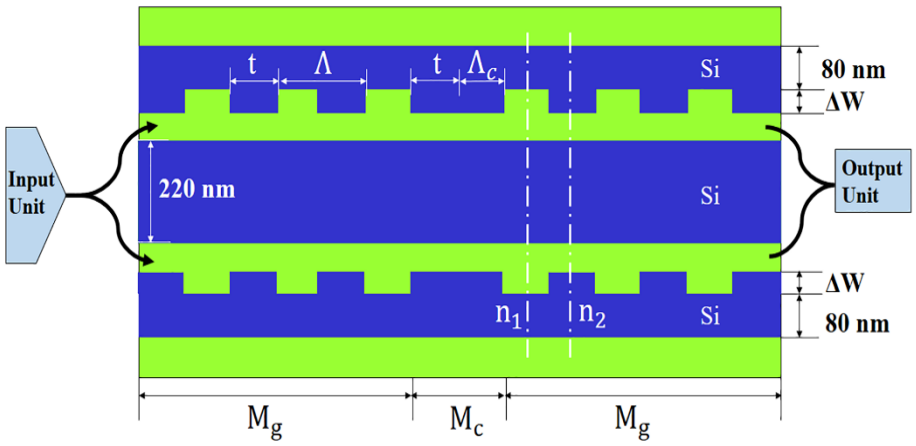

(a)

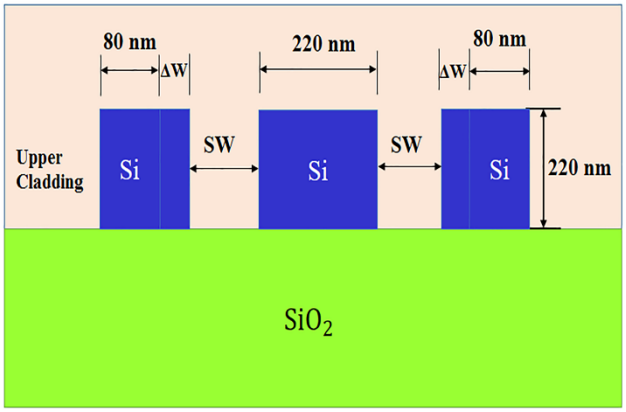

(b)

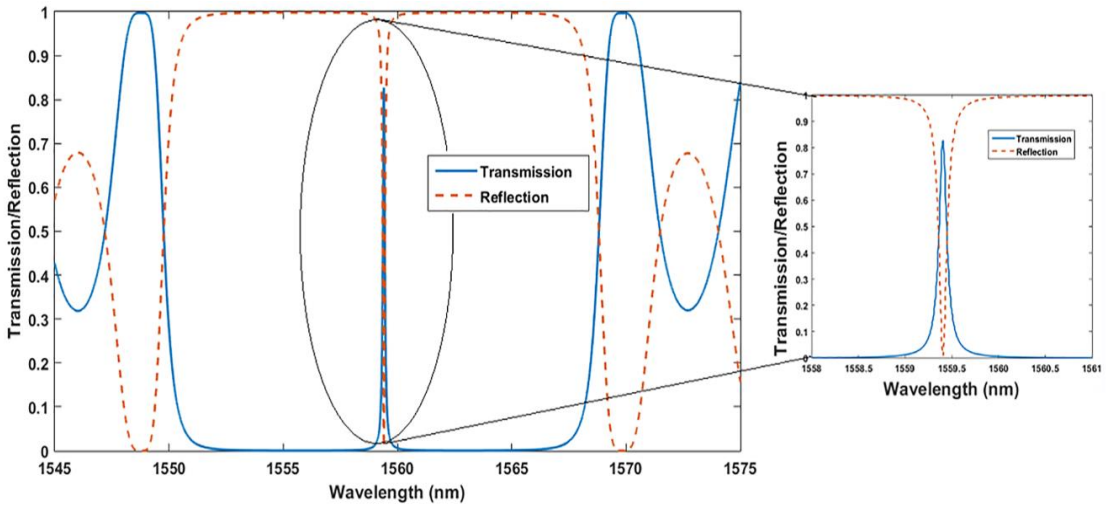

(c)

Figure 6.2.4: (a) Sidewall gratings in the inner side of the outer channels of dual slot waveguide, (b) cross-sectional view of the proposed device, (c) transmission and reflection spectra of the device (Inset represents the zoomed central region of the spectrum)

Figure 6.2.4 (c) plot the normalized transmission and reflection spectrum of the inner sidewall grating based DSW. The spectrum showed the resonating band (λ_r) with a sharp peak at 1559.41 nm wavelength comprised a -3 dB bandwidth of ~ 0.055 nm. The

calculated Q factor $(\lambda_r/(\Delta\lambda)_{-3\,dB})$ is around 28352 with a transmissivity of 0.84. The high Q factor with high transmitivity is suitable for the multiplexing and sensing application.

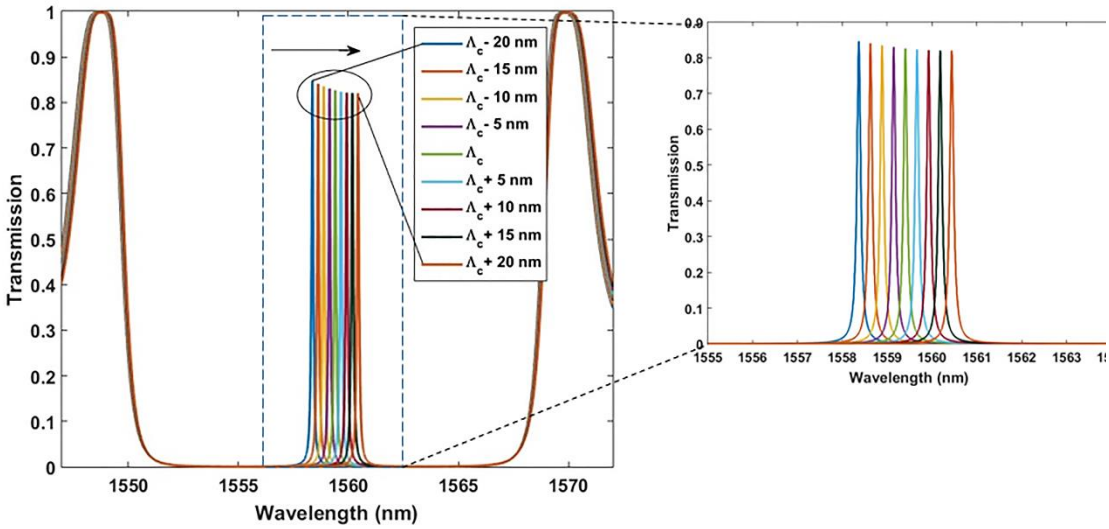

(a)

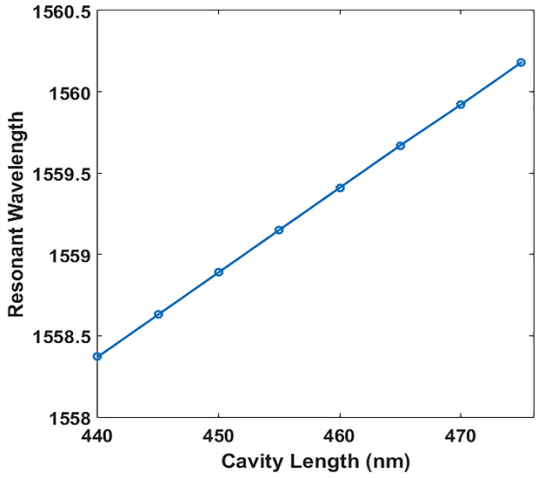

(b)

Figure 6.2.5: Transmission spectra representing shift in resonant wavelength for a change in cavity length of the device (Inset represent zoomed version of the spectrum), (b) change in resonant wavelength for a change in cavity length

For the probe of facilitating the device for multiplexing application, the variation of the change in the resonant frequency is calculated for a change in the dimension of the cavity length. The tunability of wavelength is accomplished by varying the cavity length in steps of 5 nm for a significant shift in the resonant wavelength of the device as shown in Figure 6.2.5 (a). The response for a shift in a resonant wavelength corresponding to a change in cavity length resembles the linear response (Figure 6.2.5 (b)).

(a) Effect of parameter in Transmission Spectra

To study the suitability of the device for a refractive index sensor the effect of parameters like duty cycle (ratio of t/Λ), grating depth and the number of periods (N) are considered for the evaluation of the Q factor and transmissivity.

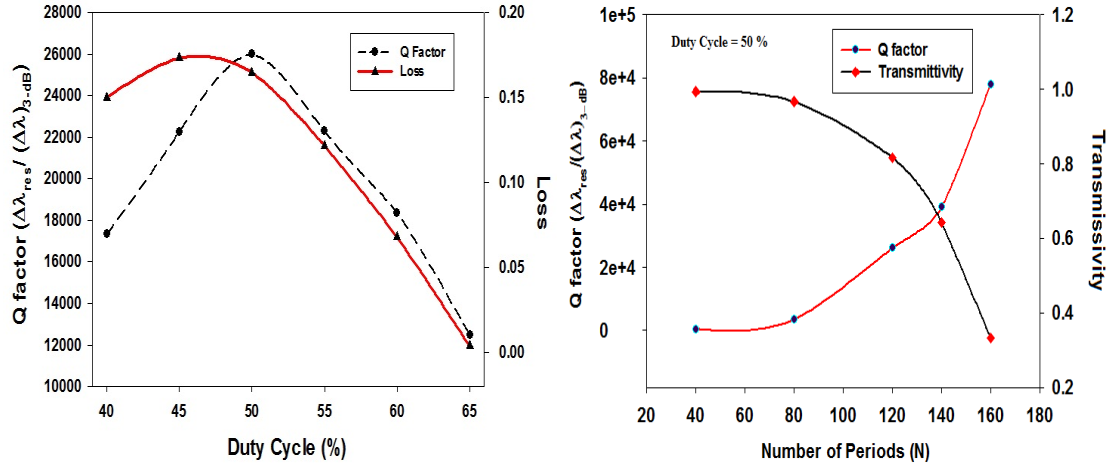

(a) (b)

Figure 6.2.6: (a) Variation of Q-factor and Loss as a function of the Duty Cycle, (b) Variation of Q factor and Transmissivity for a variation of number of grating period (N) keeping the Duty Cycle fixed at 50 %.

The loss in the device is the signal that is lost during the transaction from input to output. The signal is lost in the device due to the out-of-plane scattering when there is a mismatch of the corrugation depth and field propagation in the device. The loss is calculated as, Loss

= 1 - (T_r + R_r), where T_r and R_r, are transmissivity and reflectivity respectively [144]. From Figure 6.2.6 (a) it is observed that the Q factor is high when the duty cycle is at 50%, whereas the loss varies very little for a duty cycle ranges between 40% - 52%. The increase in the duty cycle reduces the loss significantly due to the reduction in the mode-mismatch loss that occurs when highly concentrated field encounters with the grating. Figure 6.2.6 (b) plots the variation for a change in the number of periods (N) of gratings in the waveguide for a duty cycle of 50 %, results shows that the resonating peak highly influenced by the N, for a greater N the Q factor increases significantly but the transmissivity reduced. For the rest of our work, we have selected the N equals to 120, which provides Q factor of 28352 and transmissivity of 0.84.

(b) Modeling of the Refractive Index Biosensor

We designed the refractive index biosensor based on gratings in the DSW. The microfluidic framework is considered on the upper cladding region of the structure that carries the biomaterial in the sensing region. The resonance peak is generated in the stop band of the transmission spectra due to the insertion of the cavity at the center of the grating in the DSW. The sensing principle is based on the detection of the shift in the resonant peak on account of the change in the refractive index of the upper cladding region (n_c). For a resonant shift biosensor, high transmission along with high Q factor (narrow bandwidth) is desired. Figure 6.2.7 (a) represents the combined spectral response. The refractive index of the upper cladding (n_c) material is varied from 1.328 to 1.338. As expected of the biosensor for a variation in the biomaterial, slight increase in the peak is observed on increasing n_c due to the increase of the mode effective index. The resonance bandwidth is also increased from 41 pm at n_c = 1.328 to 55 pm at n_c = 1.338 results in the reduction of the Q factor, which is occurred due to the increase in the waveguide loss. The range of Q factor for the biosensor is 27391 to 37530, that is sufficiently large for the enabling the strong light-matter interaction. A biosensor is attributed from two parameters, sensitivity (S) and LOD (Δn_{min}). The limit of detection is the minimum change in the refractive index required to shift the resonant wavelength that is detected by the sensor, and it can be expressed as [46],

$$\Delta n_{min} = \frac{\Delta\lambda_{min}}{(2\Lambda)\left(\frac{dn_{eff}}{dn_c}\right)} \qquad (6.2.4)$$

Where the calculated value of $\Delta\lambda_{min}$ is 3.6 pm, it is the one-fifteenth of $(\Delta\lambda)_{3\text{-dB}}$ of the lowest Q factor that is a measurable resonance wavelength shift [61]. The change in the effective index corresponding to a change in n_c is calculated from Figure 6.2.7 (b) and is found out to be, $dn_{eff}/dn_c = 0.7196$. Hence, the theoretical value of $\Delta n_{min} = 5.4423 \times 10^{-6}$. The value of the sensitivity ($S = \Delta\lambda/\Delta n_c$) is 661 nm/RIU. The same value of the Δn_{min} is evaluated by using the sensitivity from the expression, $\Delta n_{min} = \Delta\lambda_{min}/S$ [61].

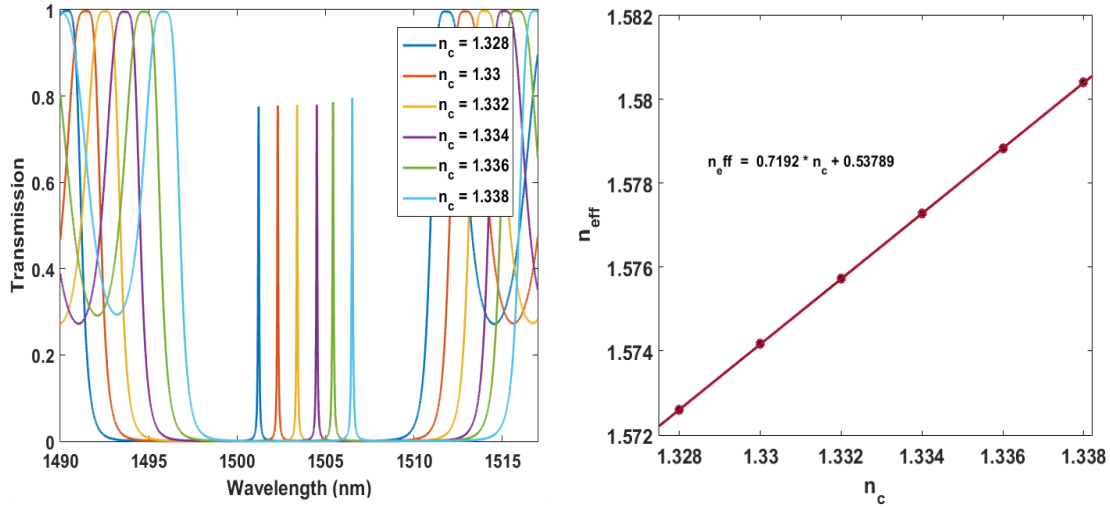

(a) (b)

Figure 6.2.7: (a) Transmission spectra of the device, and (b) Variation in effective index for a change in refractive index of biomaterial

The performance characteristics of some integrated biosensor are compared in Table 6.2.1. Sahba et al. in [104] reported a highly sensitive biosensor based on SOI ring resonator with a 150 nm thick strip waveguide. Theoretical optimization is also performed and demonstrated a sensitivity of 270 nm/RIU. In [46] Bragg grating waveguide is reported to have a sensitivity of 90 nm/RIU with a Q-factor of 13265. However an analyses

corresponding to a ring slot in photonic crystal waveguide is provided in [145], the reported sensitivity of 160 nm/RIU. A concentric dual-ring resonator with a sensitivity of 180 nm/RIU is demonstrated in [146]. The LOD and sensitivity comparison represents the definite benefit of using the proposed configuration. The LOD and sensitivity comparison represents the definite benefit of using the proposed configuration.

Table 6.2.1: Limit of detection comparison of SOI based sensors

Refractive Index Sensor	**Limit of Detection (Δn_{min})**	**Sensitivity (nm/RIU)**	**Q - factor**
PhC waveguide for liquid sensor [145]	8.75×10^{-5}	160	11477.3
SOI racetrack resonator [104]	7.5×10^{-4}	270	-
SOI ring resonator [146]	1.1×10^{-5}	180	-
SOI phase shift grating resonator [46]	5×10^{-5}	90	13265
This work	5.4423×10^{-6}	661	37530

6.2.3 Summary

In this article, modeling of a grating slot waveguide is performed for the evaluation of refractive index sensor. The optimized parameters of a sensor is presented that possess a high Q factor of 21637. The sensor works on the principle of detection of a shift in resonant wavelength for a change in refractive index of a biomaterial. Optimized parameters, specifically waveguide geometry, slot width and length of phase shift cavity is reported for maximizing the light matter interaction. The sensitivity of a sensor is 0.19 μm/RIU with a limit of detection of 3.684×10^{-4} RIU.

In this work, the sidewall grating on SOI dual slot waveguide is designed for a refractive index biosensor. The slot waveguide confines the quasi-TE mode in slot region that causes to increase the interaction between the field and biomaterial. The device geometric

parameters are optimized to obtain the high Q factor and high transmissivity for improving the performance characteristics. The analytical modeling of the device is performed using the transfer matrix method. The sensor is investigated through the measurement of the resonant wavelength shift that is caused due to the local variant of the biomaterial refractive index. The designed sensor is compact in size, possess a limit of detection (Δn_{min}) of 5.4423×10^{-6} RIU and suitable for integration in the lab-on-chip application.

Chapter 7

Hybrid Resonating Structure based on Sub-Wavelength Grating and Strip Waveguide

The most prominent configuration for confining light in low refractive index region is slot waveguide. Hence, the resonator structure based on the slot waveguide significantly improved the biosensing characteristics [41,57,102]. The main drawback of slot waveguide is the high propagation losses [57]. Perez et al. and Wang et al. reported the more advanced low loss waveguide that is based on the sub wavelength gratings (SWG) [147,148]. SWG allows to model the propagation characteristics of the waveguide by modeling the grating period, width of the gratings, duty cycle etc. It can provide an alternate solution to replace the slot waveguide for a resonating structure.

The ring resonators have been extensively explored for biosensing applications. It comprises of the bus waveguide coupled with a ring that works in two configurations: all-pass and add-drop. In all-pass configuration, single bus waveguide is utilized, whereas add-drop utilizes two bus waveguides. The configurations of ring resonators have been widely explored for enhancing the biosensing performance. Recently Sahba et al. [16] reported a ring resonator based on the ultra-thin waveguide, they have achieved a sensitivity of 133 nm/RIU. Researchers have explored the ring resonator by considering the various configurations of the waveguide [18,24,57,145,149]. The slot waveguide based ring resonator provide high sensitivity, however it suffers from higher losses [104]. Hence, in order to evaluate a performance of the biosensing device that have low loss and high sensitivity we have proposed a strategy to combine a SWG waveguide and strip waveguide. A low loss SWG waveguide have been used for bus waveguide and ring is designed through the strip waveguide. First, we discuss the fundamental aspects of the SWG waveguide and its potential capability to increase the light matter interaction. Second, the

analysis of the composite structure of ring resonator is proposed with an evaluation of the sensitivity.

The organization of the work is as follows: sec. 7.1 provides a theoretical study of the SWG waveguide, the sensor design and operating principle be discussed in sec. 7.2. In sec. 7.3 results and discussion followed by the conclusion and references at the end.

7.1 Sub-wavelength Grating (SWG) Waveguide

The SWG waveguide consist of a periodic arrangement of the high and low refractive index material. The light wave propagation in such a periodic structures follows a Bloch-Floquet relationship. It can be considered as 1D periodic structure, and its working is dependent on the period or duty cycle of gratings [150]. Since the 1D periodic structure relies on phase matching condition $\lambda_B = 2 \cdot \Lambda \cdot n_{eff}$, acts as a normal Bragg grating waveguide, where λ_B is Bragg wavelength, and n_{eff} is the effective index of the waveguide segment. Similarly, the SWG waveguide is harnessed to work for two more conditions, which relies on λ_B. When the grating period $\Lambda > \lambda_B/2 \cdot n_{eff}$, the region is suitable for designing of fiber to waveguide coupler, since in this region the Bloch wave becomes weak and radiated out. Likewise for a region $\Lambda < \lambda_B/2 \cdot n_{eff}$, the sub-wavelength region acts as a low loss waveguide [151,152]. The schematic of the SWG waveguide is shown in Figure 7.1.1. The structure is periodic only in z-direction, which make the light propagation to satisfy the Bloch-Floquet mechanism and the electric field of Bloch mode can be written as, $E(x, z) = E(x, z + \Lambda)$, and the wave equation can be written as, $E(x,y,z) = E_k(x,y,z) \cdot \exp(-ikz)$ [147].

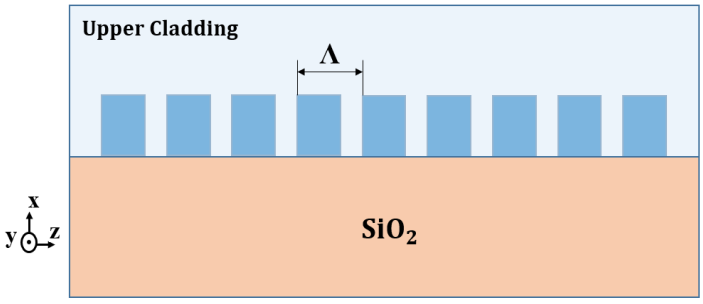

Figure 7.1.1: Sub-wavelength grating waveguide

In a way, planar waveguide is analyzed for biosensing applications using effective index method, the effective index of the SWG waveguide can also be evaluated. Since there is no analytical model is reported in the literature for representing the sub-wavelength waveguide, the numerical method is required for an evaluation of the effective index and group index [153]. The analysis is mainly dependent on the band structure calculation of 1D photonic crystals considering the Brillouin zone ranges from $-(\pi/\Lambda) < k_z < (\pi/\Lambda)$.

Steps for an evaluation of the Effective and Group Index provided in Ref. [153]

1. Since the SWG waveguide is a periodic structure of the high and low index, the approximate refractive index is evaluated through the consideration of the effective index approximation method. The equivalent effective index is represented as,

$$n = dc \cdot n_h + (1 - dc) \cdot n_w \qquad (7.1.1)$$

   The value of duty cycle (dc) of a waveguide is dependent on weighted lengths l_h and l_w of high and low refractive index respectively.

2. Then a same dimension strip waveguide is drawn in mode solve tool, and the material with the constant refractive index (n) is considered. From this step, the value of the approximate effective index (n_{eff1}) is found by performing the eigenmode calculation.

3. In this step we have evaluated the value of kx for getting the stop band region. The value of $k_x = k_0 \cdot n_{eff} = 2 \cdot (\pi/\lambda) \cdot n_{eff1} = n_{eff1} \cdot (\Lambda/\lambda)$.

4. The value of the $k_x < k_{x1}$, where kx1 is the calculated from the strip waveguide consisting of the n_h material. In simpler meaning it denotes the Bragg condition, so for a waveguide to operate at a sub-wavelength region the value of k_x must be smaller than k_{x1}.

5. The band calculation is performed for a range of k_x and from that the n_{eff} and n_g is evaluated. Then the parameter is fit to a fourth order polynomial to extract the value of n_{eff} and n_g.

In Figure 7.1.2 (a), (b) and (c) light line is plot, it is observed that for increasing the waveguide width the mode is more confined in the SWG waveguide.

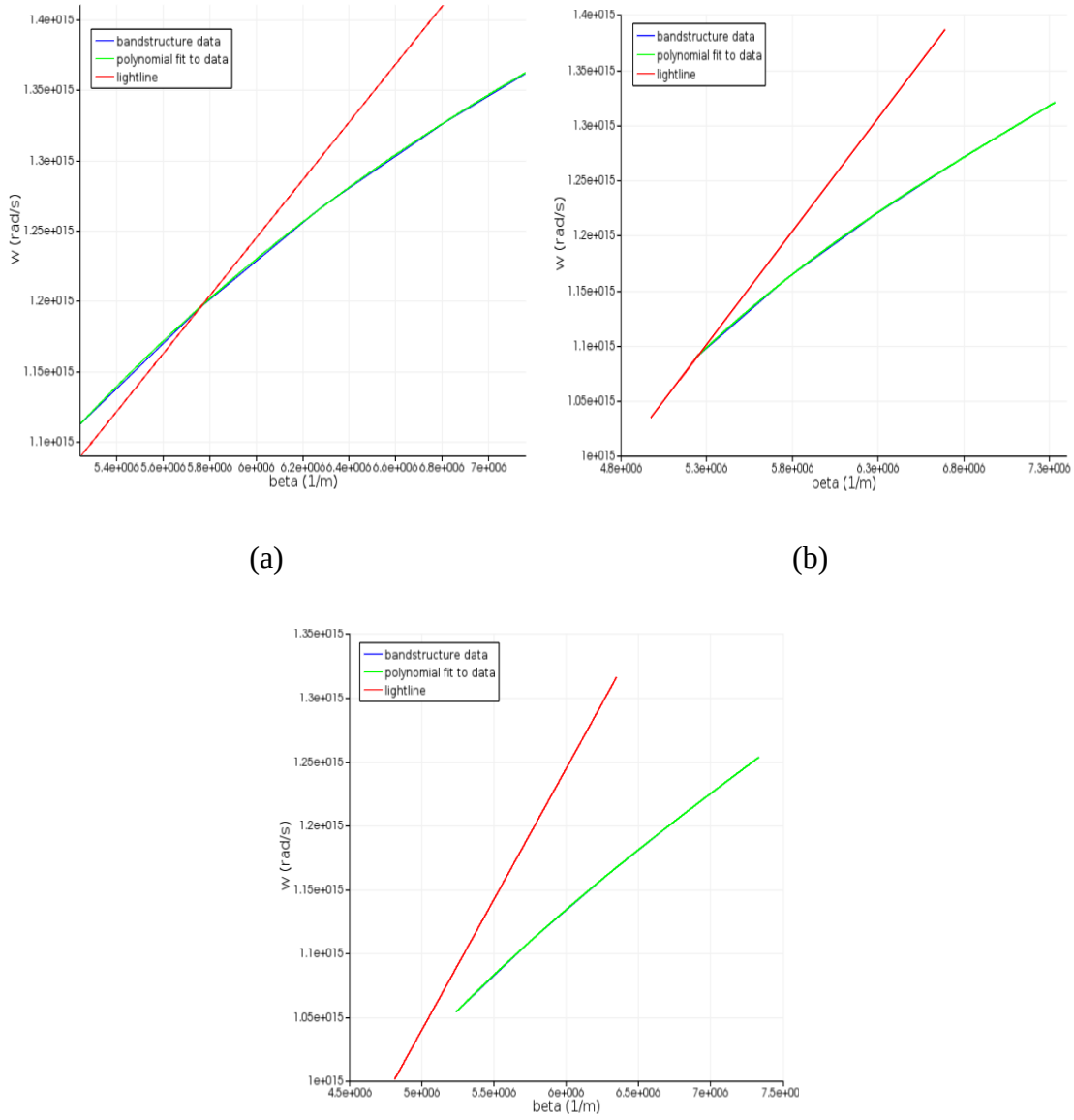

(a) (b)

(c)

Figure 7.1.2: Dispersion diagram for variation of SWG waveguide width (a) 500 nm, (b) 600 nm and (c) 700 nm

For the waveguide width of 500 nm the waveguide cutoff the light line, in that region the signals leaks out to the substrate region. However, for a SWG width of 600 nm and 700 nm the signals well confined in the waveguide for a considered range of β. It is also depicted from the results that for higher value of β the graph approaches to a constant value that means higher wavenumber derive the SWG to Bragg condition. The group velocity of the waveguide is evaluated through the slope of the graph, and hence facilitate to produce the group index of the waveguide (Figure 7.1.3). Similar group index is also found for the effective index of the propagating optical mode (Figure 7.1.3 (b)).

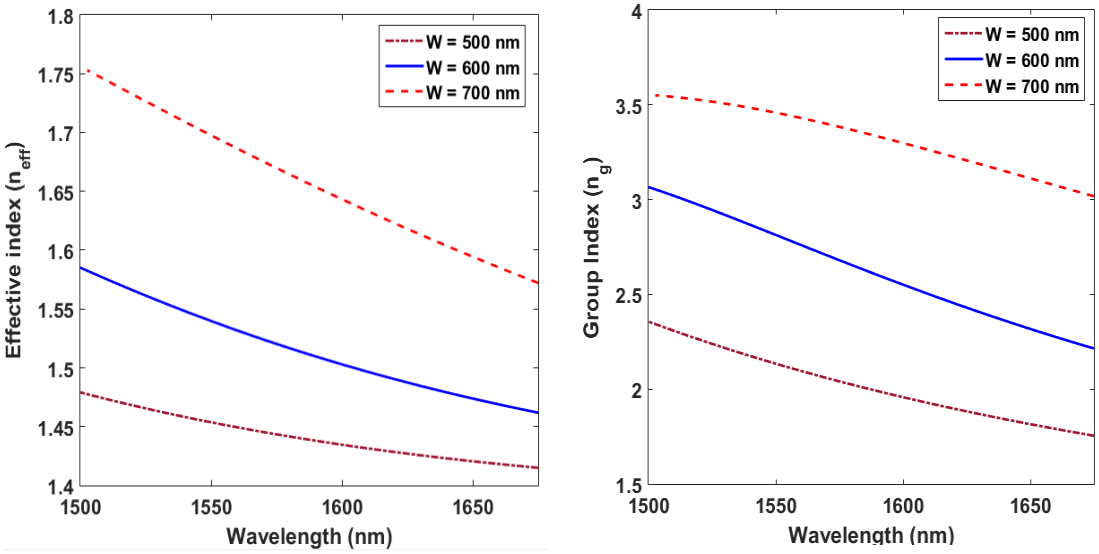

(a) (b)

Figure 7.1.3: Effective index and group index for a SWG waveguide for various waveguide width for dc = 0.6

It is also evident from the Figure 7.1.3 (b), that a slope is large for waveguide width of 600 nm for the wavelength region of interest that is around 1550 nm. So for the devising the ring resonator we have selected the waveguide width of 600 nm.

7.2 Modeling of the Hybrid Ring Resonator

The design comprised a hybrid structure of the sub-wavelength grating and strip waveguide. The add-drop configuration of the ring resonator is designed. The two parallel channels are composed of the SWG waveguide, and a central ring is made up of a strip waveguide. The considered width of the SWG and strip waveguide is 600 nm. The gap between the bus waveguides and ring is of 200 nm. At the ends of the SWG waveguides, four triangular bridge segments are attached to facilitate the signal coupling between the strip and SWG waveguide. The perpendicular length of all bridge segments are 16 µm. The radius of ring waveguide is 10 µm, the period of grating is 300 nm and the duty cycle is 0.6. The material in the upper cladding of the waveguide enables to penetrate in the gap region of the SWG, hence it directly appears in contact with the propagation of the optical field. The schematic is shown in Figure *2.2.1*.

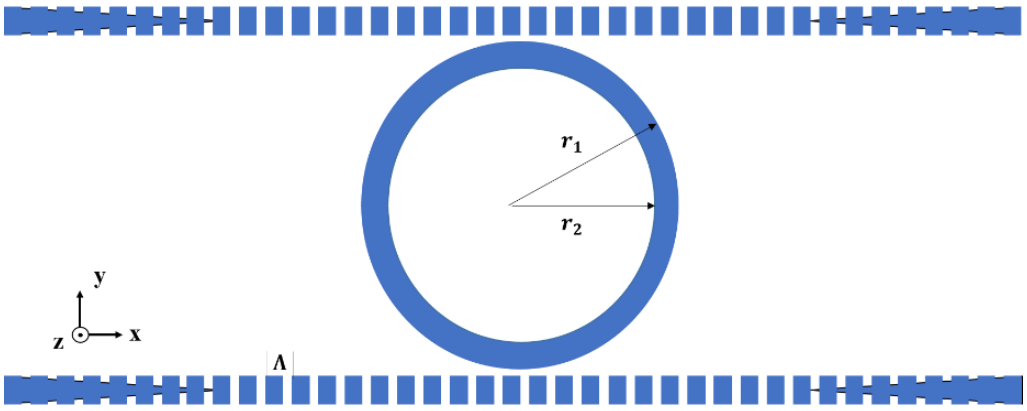

Figure 7.2.1: Integration of the SWG and strip waveguide ring resonator of 10 µm radius

The structure is simulated through the FDTD method by considering the varying refractive index of upper cladding region (n_c). The spectrum in Figure 7.2.2(a) shows a definite shift in the resonance wavelength for an increment of n_c. The zoomed version of the spectra is shown in Figure 7.2.2(b). The sensitivity is calculated by considering the equation (2.9.1) and it is found out to be 206 nm/RIU.

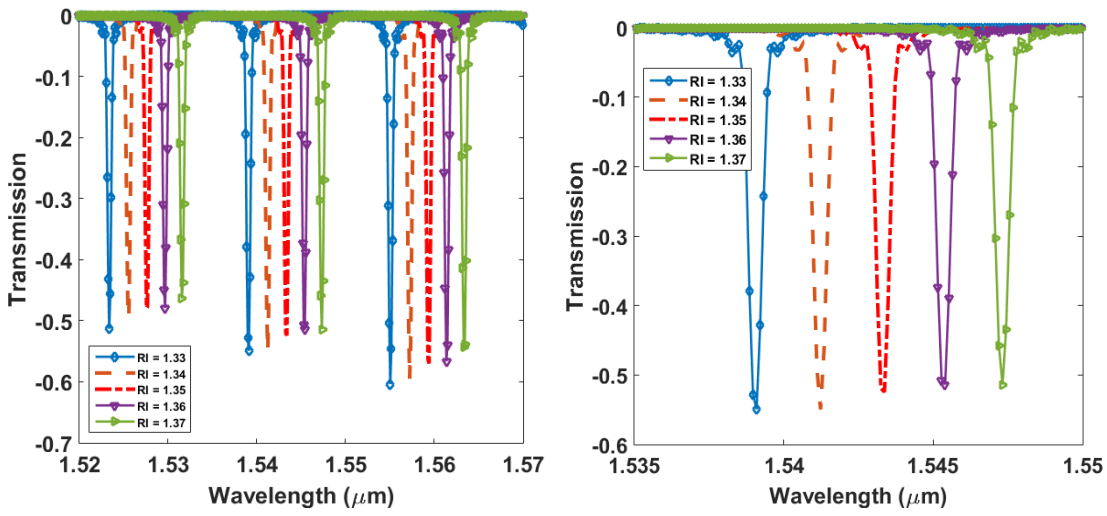

Figure 7.2.2: Transmission spectra of hybrid ring resonator for variation of the refractive index of the biomaterials

For an evaluation of the detection limit of the device the refractive index on the surface of the device is varied in steps of 0.001 RIU. Almost linear behavior has been found for the variation. The transmission spectra for the same is shown in Figure 7.2.3.

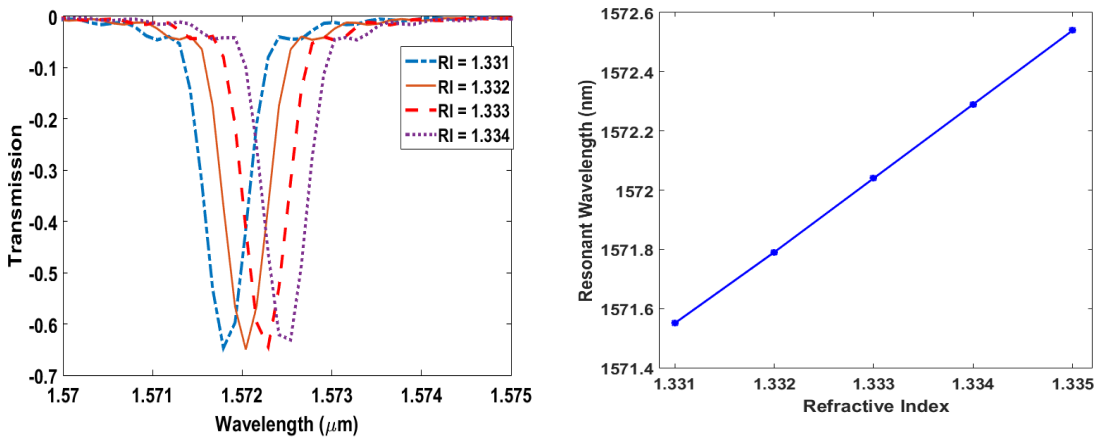

Figure 7.2.3: (a) Shift in the resonant wavelength for refractive index ranges from 1.331 to 1.334 in steps of 0.001 RIU, (b) linear response between the resonant wavelength and RI

7.3 Summary

In this chapter, we have discussed the hybrid ring resonator based on SWG and strip waveguide. The SWG is a special type of waveguide that allows modulating the optical characteristics of the waveguide by altering the waveguide width, duty cycle and the period of the gratings. Through the band structure analysis the group index and effective index is computed. The ring segment of the resonator is made of the strip waveguide on SOI platform that provides tight confinement of the optical mode in the core region. The strip waveguide on SOI provides very low bending loss. The complete structure is then simulated for biosensing applications. The sensitivity of the device is found out to be 206 nm/RIU and a detection limit of the order of 10^{-3} RIU. Since we have not optimized the structure for narrowing the stop band region. Surely narrowing the resonating band enables us to generate high value of Q factor that may improve the detection limit of the device.

Chapter 8

Conclusion and Future Scope

8.1 Conclusion

The overall goal of this thesis is to demonstrate the optical resonator for biosensing applications. There is a need of an efficient sensing device that can perform the task in no time, consumes very less power, robust, and ease to fabricate. A biosensor is a device that is utilized for many applications such as medical diagnostics, new drug investigation, food testing and future smart home healthcare systems. The assembly of a biosensor consists of transducing element, bio-recognition layer, microfluidic framework, lasing and readout systems. The biosensors on the chip are well known as lab-on-chip (LOC). The vital part of the LOC is the sensing unit. The sensing device on the integrated platform provides high sensitivity and lower limit of detection as compared to other sensing devices.

In this thesis, we have studied several configuration of integrated optical (IO) resonators for sensing application. The evanescent waves are utilized for sensing in the IO based sensor. We have proposed resonating structures based on the sidewall grating waveguide to enhance the performance of the existing biosensing devices. The change in the refractive index of a biomaterial on the surface of the sensor leads to shift in the resonant wavelength, which is used for the sensing operation.

Initially we have studied and optimized the parameters of the planar strip waveguide. Several photonic devices utilizes the strip waveguide such as ring resonators, grating waveguides, interferometers etc. Despite of the fact that the strip waveguide on SOI platform have high confinement of field, there are still several losses occurs in the configuration. The major one is the scattering losses due to the bending of the waveguide. The bending configuration is very much desired for the compact optical circuit design and in the ring resonator. The larger waveguides are more often bend to utilize the limited

substrate area. So the waveguide should be optimized to have a lower bending radius for neglible losses. By keeping this aim, we have experimentally verified the performance of the strip waveguide by employing the Michelson Interferometer configuration and then the results are compared with the simulated one. The commercially available dimensions of the waveguide are considered to facilitate the fabrication feasibility. At an end the biosensing characteristics of the device is also studied by considering the effect of phase shift provided by the unbalanced arm lengths of the device. For an approximate 500 nm arm length difference the sensitivity of the 225 nm/RIU is found with a limit of detection value of 3.43×10^{-3} RIU. Since the interferometer configuration is having a sinusoidal variation in the output, it is difficult to predict the changes occurs in biomolecule in a real time system. Therefore, the resonating configuration is investigated for eliminating the following drawbacks.

The first resonating structure for sensing application is based on the sidewall grating waveguide. The evanescent field sensing is most commonly employed in the resonating structures. The sidewall grating waveguide is analogous to a 1D photonic crystal waveguide that is having a stop band region in the transmission spectra. All the wavelength satisfies the phase matching condition are highly reflected owing to a gap in transmission spectra. This resonating structure requires the strip waveguide. Since in the conventionally reported sidewall gratings waveguide the bandwidth of the stop-band region is narrow that makes the limitation in the refractive index of biosensor. To eliminate this problem we have cascaded two different configurations of the sidewall grating waveguides that causes an increase in the stop band region. An insertion of the phase shift cavity at a center of the waveguide confine a narrow band in the middle of the stop band region. On account of altering the refractive index of the biomaterial the position of the resonant band is shifted, the process of shifting is quantified for an evaluation of the biomaterial, in this structure the effect of temperature on the refractive index of a biomaterial is also considered. The sensitivity found for the structure is 90 nm/RIU with a LOD of 10^{-4} RIU. The structure is temperature stable and only a -0.0075 nm/^{0}C temperature sensitivity is observed. In this configuration the lower value of the sensitivity is found. So forth in the next configuration

we have eliminated the requirement of resonating band in the stop band region and designed a biosensor that utilizes the movement of the narrow stop-band.

For increasing the performance of the device, we have modified the structure to make a lower interaction between the confined mode and gratings. The lower interaction causes to reduce the coupling coefficient, which further reduces the bandwidth of the stop band region. In this structure, a gap width separates the core of a waveguide and grating segments, the design is called as the cladding modulated grating waveguide. This design has an advantage of providing the narrow reflection band. The bandwidth of the reflection band of 220 nm thick NBCM waveguide is 0.39 nm. The reflection band can directly be utilized for biosensing application. However, the decrease interaction of the evanescent field and biomaterial decreases the sensitivity. Hence, the characteristics of the device is evaluated for the variation in the waveguide thickness, which are 220 nm, 150 nm and 100 nm. The main aim of opting the thickness variation is to increase the ratio of the change in the effective index to refractive index of the biomaterial dn_{eff}/dn_c. The value of dn_{eff}/dn_c for three thickness values 220 nm, 150 nm and 100 nm is found out to be 0.153, 0.247, and 0.374 respectively. For a waveguide thickness of 100 nm, the sensitivity is found to be 322.96 nm/RIU and a detection limit of the order of 10^{-4} RIU.

The second type of the resonating structure comprises of the slot waveguide. The slot waveguide is having an advantage of confining a light in the lower refractive index slot region, which cause a higher light matter interaction. Hence, a small possible change in the refractive index of a biomaterial makes significant change in the optical characteristic. Firstly, the gratings in a single slot waveguide is demonstrated. The sensitivity of the device is 190 nm/RIU with a LOD value of 3.684×10^{-4} RIU. In a second part, the dual slot waveguide is designed for a biosensing application. The parameters of the dual slot waveguide are optimized for maximizing the theoretical value of the sensitivity. The optimized dimensions of the dual slot waveguide is then used for analyzing the resonating structure by drawing the grating in the inner sidewall of the waveguide. The structure possesses a detection limit of around 10^{-6} RIU and a sensitivity of the 661 nm/RIU.

The last resonating structure is based on the hybridization of the SWG waveguide and a planar strip waveguide. The structure utilizes the advantages of both the waveguides; the SWG waveguide is ideally a lossless waveguide and having a periodic structure, which is dependent on the duty cycle of the grating. The biomaterial on the sensor surface easily infiltrated in a gap region of the grating waveguide causes a direct interaction between the propagated field and biomaterial. Moreover, the strip waveguide that is having a high confinement of the field in the core region is used for designing a ring structure. The radius of the ring is 10 μm, which is having a negligible bend loss. Hence, the overall structure is suitable for label free biosensing application. The sensitivity provided by the structure is 206 nm/RIU.

8.2 Future Scope

In this work, we have tried to optimize the performance of the resonator based biosensing devices. The devices are compact and can easily integrate with other optical devices. However more work need to be done for increase the performance characteristics of the device. Herein we provide few ideas for future implementation,

1. The use of the multislot waveguide for increasing the light matter interaction can be opted for making the resonating device. Like the single and dual slot waveguide have higher electric field to matter interaction, the multislot waveguide can be designed that can further enhance it. The designed waveguide can be used for resonating devices. For a ring resonator it is the field coupling with other parallel multislot waveguide segment is desirable that is difficult to achieve and moreover it may suffers from the scattering losses due to bending. So for avoiding such problems, it is more fruitful if straight resonating structure are designed. The multislot grating waveguide is one such configuration. The configuration definitely provides an advantage of high sensitivity. However, the high Q factor is required for getting a lower limit of detection, which is a little bit challenging.

2. Since lot of work, have been done for improving the biosensing performance. The use of porous materials for a core region of a waveguide can immensely increase the performance of the resonating structure; the most promising material is porous silicon. The refractive index of the porous silicon lies in between 1 to 3.45 depending on the size of the pores and the infiltrated material (smaller size biomolecule). The filed directly interacted with the biomolecules present in the pores of the waveguide. In addition, the decrease in the refractive index contrast cause to increase the field fraction on the surface of the waveguide. The resonating device utilizing this material increase the sensitivity and perhaps if properly designed it may also provide high Q that can provide lower detection limit.

3. A straight resonating structure can be designed by adopting the sub-wavelength grating waveguide. The configuration has an advantage of implementing the coupler and resonating unit all on the similar SWG waveguide. The grating coupler requires coupling the light from the optical fiber to the waveguide, then by altering the periodic variation of the sub-wavelength region for the perturbation of the effective index the Bragg grating resonator can be designed. However, the length of the device in large, but it surely provides an advantage of increasing the performance of the sensing device.

4. While designing the structure, fabrication variability needs to be consider. Often it is found that the roughness occurred on the surface during fabrications causes to increase the scattering losses in the device. The non-uniformity on the sidewall or the top of the waveguide characteristics. There are two ways of performing the fabrication variability. In the first approach, multiple devices should be fabricated and based on that an errors region can be found. In the second method the fabrication variability can be found by using the corner method. In the corner method the waveguide dimensions provided by the foundry are intentionally changed to fit in the corner of the rectangle. So that there are total 9 variations of the waveguide should be studied and based on that the working region of the device should decide.

Author Publications

Journals

1. Sourabh Sahu; Jalil Ali; Ghanshyam Singh "Refractive index biosensor using sidewall gratings in dual-slot waveguide" Optics Communications (Elsevier), volume 402, pages 408–412, 1 November 2017. DOI: 10.1016/j.optcom.2017.06.051 (SCI Journal, IF: 1.588).
2. Sourabh Sahu; Jalil Ali; Ghanshyam Singh, "Optimization of dual-slot waveguide for refractive index biosensor" Accepted to publish with Optica Applicata (PSP), volume 48 issue 1, 2018. (SCIE Journal, IF: 0.641), paper ID: OA-00657-2017-02.
3. Sourabh Sahu; Jalil Ali; Preecha P. Yupapin; Ghanshyam Singh "Optical biosensor based on a cladding modulated grating waveguide" Under review with Optics Communications (Elsevier, SCI Journal), paper ID: MB-2150, 2017.
4. Sourabh Sahu; Jalil Ali; Preecha P. Yupapin; Ghanshyam Singh "High-Q and temperature stable photonic biosensor based on grating waveguides" Under review with Optical and Quantum Electronics (Springer, SCI Journal), (paper ID: OQEL-D-17-00697), 2017.
5. Sourabh Sahu; Preecha P. Yupapin; Jalil Ali; Ghanshyam Singh "Porous silicon based Bragg-grating resonator for refractive index biosensing" Under review with Photonic Sensors (Springer, Scopus Journal) (paper ID: PS-01700459), 2017.
6. Sourabh Sahu; Ghanshyam Singh "Hybrid structure of sub-wavelength grating and strip waveguide based resonator for optical biosensor" Under preparation, to be submitted to Optical Engineering (SPIE, SCI Journal).

International Peer Reviewed Conferences

1. S. Sahu, K. V. Kozadaev, G. Singh, "Michelson interferometer based refractive index biosensor," in 13th International Conference on Fiber Optics and Photonics, Photonic-16, Kanpur, December 04-08, 2016, OSA Technical Digest, paper Th3A.60, ISBN: 978-1-943580-22-4, DOI: 10.1364/PHOTONICS.2016.Th3A.60.
2. Sourabh Sahu, Ghanshyam Singh "Modeling of phase shift bragg grating biosensor for non invasive detection of blood components" IEEE International Conference, ICRAIE-2016, Jaipur, India, December 23–25, 2016, IEEE Xplore Digital Library, Print ISBN: 5090-2806, DOI: 10.1109/ICRAIE.2016.7939565.
3. Sourabh Sahu; Ghanshyam Singh "Modeling of grating slot waveguide for high-Q based refractive index sensor" IEEE International Conference 'COMPTELIX-2017", July 1-2, 2017, Jaipur, IEEE Xplore Digital Library, Page(s):394–396, DOI: 10.1109/COMPTELIX.2017.8004001.

Bibliography

[1] R.M. Lequin, Enzyme Immunoassay (EIA)/Enzyme-Linked Immunosorbent Assay (ELISA), Clin. Chem. 51 (2005) 2415–2418. doi:10.1373/clinchem.2005.051532.

[2] M.S. Luchansky, R.C. Bailey, Silicon photonic microring resonators for quantitative cytokine detection and T-cell secretion analysis, Anal. Chem. 82 (2010) 1975–1981. doi:10.1021/ac902725q.

[3] D. Ivnitski, I. Abdel-Hamid, P. Atanasov, E. Wilkins, Biosensors for detection of pathogenic bacteria, Biosens. Bioelectron. 14 (1999) 599–624. doi:10.1016/S0956-5663(99)00039-1.

[4] P. Prabhathan, V.M. Murukeshan, Silicon Waveguide Multiplexed Sensor Array Configuration for Label-Free Biosensing Applications, 94 (2014).

[5] T. Bolstad, Fabrication of a Silicon Photonic Crystal Biosensor, (2014).

[6] K. Zinoviev, L.G. Carrascosa, J. Sánchez del Río, B. Sepúlveda, C. Domínguez, L.M. Lechuga, Silicon Photonic Biosensors for Lab-on-a-Chip Applications, Adv. Opt. Technol. 2008 (2008) 1–6. doi:10.1155/2008/383927.

[7] D.-X. Xu, A. Densmore, R. Ma, J.H. Schmid, M. Vachon, J. Lapointe, S. Janz, E. Post, A. Delage, P. Cheben, WDM addressed SOI ring resonator biosensor array, in: 2009 6th IEEE Int. Conf. Gr. IV Photonics, IEEE, 2009: pp. 34–36. doi:10.1109/GROUP4.2009.5338299.

[8] W.-C. Lai, S. Chakravarty, Y. Zou, R.T. Chen, Silicon nano-membrane based photonic crystal microcavities for high sensitivity bio-sensing, Opt. Lett. 37 (2012) 1208. doi:10.1364/OL.37.001208.

[9] S. Chakravarty, W.-C. Lai, Y. Zou, R.M. Gemmill, R.T. Chen, Silicon photonic

crystal microarrays for high throughput label-free detection of lung cancer cell line lysates with sensitivity and specificity, in: B.L. Miller, P.M. Fauchet (Eds.), SPIE Proc., 2013: p. 857005. doi:10.1117/12.2003012.

[10] S. Chakravarty, W.C. Lai, Y. Zou, H. a. Drabkin, R.M. Gemmill, G.R. Simon, S.H. Chin, R.T. Chen, Multiplexed specific label-free detection of NCI-H358 lung cancer cell line lysates with silicon based photonic crystal microcavity biosensors, Biosens. Bioelectron. 43 (2013) 50–55. doi:10.1016/j.bios.2012.11.012.

[11] T. Dar, J. Homola, B.M.A. Rahman, M. Rajarajan, Label-free slot-waveguide biosensor for the detection of DNA hybridization, Appl. Opt. 51 (2012) 8195. doi:10.1364/AO.51.008195.

[12] S. Talebi Fard, Optical Resonator Sensors and Systems, University of British Columbia, 2015. http://hdl.handle.net/2429/52834.

[13] A. Densmore, D.-X. Xu, P. Waldron, S. Janz, P. Cheben, J. Lapointe, A. Delge, B. Lamontagne, J.H. Schmid, E. Post, A Silicon-on-Insulator Photonic Wire Based Evanescent Field Sensor, IEEE Photonics Technol. Lett. 18 (2006) 2520–2522. doi:10.1109/LPT.2006.887374.

[14] G.J. Veldhuis, O. Parriaux, H.J.W.M. Hoekstra, P.V. Lambeck, Sensitivity enhancement in evanescent optical waveguide sensors, J. Light. Technol. 18 (2000) 677–682. doi:10.1109/50.842082.

[15] A. Densmore, D.X. Xu, S. Janz, P. Waldron, J. Lapointe, T. Mischki, G. Lopinski, A. Delâge, J.H. Schmid, P. Cheben, Sensitive label-free biomolecular detection using thin silicon waveguides, Adv. Opt. Technol. 2008 (2008). doi:10.1155/2008/725967.

[16] S.T. Fard, V. Donzella, S.A. Schmidt, J. Flueckiger, S.M. Grist, P. Talebi Fard, Y. Wu, R.J. Bojko, E. Kwok, N.A.F. Jaeger, D.M. Ratner, L. Chrostowski, Performance of ultra-thin SOI-based resonators for sensing applications, Opt. Express. 22 (2014) 14166. doi:10.1364/OE.22.014166.

[17] B.M.A. Rahman, D.M.H. Leung, K.T. V Grattan, Light guidance in low-index slot-waveguides, in: 2012 7th Int. Conf. Electr. Comput. Eng., IEEE, 2012: pp. 506–509. doi:10.1109/ICECE.2012.6471598.

[18] S. Ghosh, B.M.A. Rahman, An Innovative Straight Resonator Incorporating a Vertical Slot as an Efficient Bio-Chemical Sensor, IEEE J. Sel. Top. Quantum Electron. 23 (2017) 132–139. doi:10.1109/JSTQE.2016.2630299.

[19] B.M.A. Rahman, D.M.H. Leung, N. Kejalakshmy, L. To, Silicon slot waveguides and their rigorous characterization, in: J. Kubby, G.T. Reed (Eds.), Proc. SPIE 8629, Silicon Photonics VIII, 2013: p. 86290K. doi:10.1117/12.2008203.

[20] F. Prieto, B. Sep lveda, A. Calle, A. Llobera, C. Dom nguez, A. Abad, A. Montoya, L.M. Lechuga, An integrated optical interferometric nanodevice based on silicon technology for biosensor applications, Nanotechnology. 14 (2003) 907–912. doi:10.1088/0957-4484/14/8/312.

[21] D. Yuan, Y. Dong, Y. Liu, T. Li, Mach-Zehnder Interferometer Biochemical Sensor Based on Silicon-on-Insulator Rib Waveguide with Large Cross Section, Sensors. 15 (2015) 21500–21517. doi:10.3390/s150921500.

[22] S. Sahu, K. V Kozadaev, G. Singh, Michelson Interferometer Based Refractive Index Biosensor, in: 13th Int. Conf. Fiber Opt. Photonics, OSA, Washington, D.C., 2016: p. Th3A.60. doi:10.1364/PHOTONICS.2016.Th3A.60.

[23] Y. Zhang, S. Yang, A.E.-J. Lim, G.-Q. Lo, C. Galland, T. Baehr-Jones, M. Hochberg, A compact and low loss Y-junction for submicron silicon waveguide., Opt. Express. 21 (2013) 1310–6. doi:10.1364/OE.21.001310.

[24] X. Jiang, L. Tang, J. Song, M. Li, J.-J. He, Optical waveguide biosensor based on cascaded Mach-Zehnder interferometer and ring resonator with Vernier effect, in: B.L. Miller, P.M. Fauchet, B.T. Cunningham (Eds.), 2015: p. 931003. doi:10.1117/12.2077943.

[25] X. Fan, I.M. White, S.I. Shopova, H. Zhu, J.D. Suter, Y. Sun, Sensitive optical

biosensors for unlabeled targets: A review, Anal. Chim. Acta. 620 (2008) 8–26. doi:10.1016/j.aca.2008.05.022.

[26] M.A. Cooper, Optical biosensors in drug discovery, Nat. Rev. Drug Discov. 1 (2002) 515–528. doi:10.1038/nrd838.

[27] S.P.J. Higson, P.M. Vadgama, Biosensors: a viable monitoring technology?, Med. Biol. Eng. Comput. 32 (1994) 601–609. doi:10.1007/BF02524233.

[28] A. Sassolas, L.J. Blum, B.D. Leca-Bouvier, Immobilization strategies to develop enzymatic biosensors, Biotechnol. Adv. 30 (2012) 489–511. doi:10.1016/j.biotechadv.2011.09.003.

[29] P. Wang, Q. Liu, Physical Sensors and Measurement, in: Biomed. Sensors Meas., 2011: pp. 51–115. doi:10.1007/978-3-642-19525-9_3.

[30] D. Grieshaber, R. MacKenzie, J. Vörös, E. Reimhult, Electrochemical Biosensors - Sensor Principles and Architectures, Sensors. 8 (2008) 1400–1458. doi:10.3390/s8031400.

[31] M. Pohanka, C. Republic, Electrochemical biosensors – principles and applications, Methods. 6 (2008) 57–64. http://www.zsf.jcu.cz/jab/6_2/pohanka.pdf.

[32] X. Chen, Optical Fibre Gratings for Chemical and Bio - Sensing, (n.d.).

[33] R. Koncki, Recent developments in potentiometric biosensors for biomedical analysis, Anal. Chim. Acta. 599 (2007) 7–15. doi:10.1016/j.aca.2007.08.003.

[34] S. V. Dzydevich, A.A. Shul'ga, A.P. Soldatkin, A.M.N. Hendji, N. Jaffrezic-Renault, C. Martelet, Conductometric biosensors based on cholinesterases for sensitive detection of pesticides, Electroanalysis. 6 (1994) 752–758. doi:10.1002/elan.1140060907.

[35] K. Ramanathan, B. Danielsson, Principles and applications of thermal biosensors, Biosens. Bioelectron. 16 (2001) 417–423. doi:10.1016/S0956-5663(01)00124-5.

[36] F. Li, Q.M. Wang, J.H.C. Wang, Theoretical analysis of love mode surface acoustic

wave device as cell-based biosensor, in: Proc. - IEEE Ultrason. Symp., 2007: pp. 2111–2114. doi:10.1109/ULTSYM.2007.531.

[37] R. Wolthuis, D. McCrae, E. Saaski, J. Hartl, G. Mitchell, Development of a medical fiber-optic pH sensor based on optical absorption., IEEE Trans. Biomed. Eng. 39 (1992) 531–7. doi:10.1109/10.135548.

[38] D. Wencel, T. Abel, C. McDonagh, Optical chemical pH sensors, Anal. Chem. 86 (2014) 15–29. doi:10.1021/ac4035168.

[39] L. Calvo, Optical waveguides: from theory to applied technologies, (2007) 401. http://scholar.google.com/scholar?hl=en&btnG=Search&q=intitle:Optical+Waveguides+From+Theory+to+Applied+Technologies#0.

[40] L. Chrostowski, M. Hochberg, Silicon Photonics Design: From Devices to Systems, Cambridge Univ. Press. (2015) 437. doi:10.1017/CBO9781316084168.

[41] W.-C. Lai, S. Chakravarty, X. Wang, C. Lin, R.T. Chen, On-chip methane sensing by near-IR absorption signatures in a photonic crystal slot waveguide., Opt. Lett. 36 (2011) 984–986. doi:10.1364/OL.36.000984.

[42] S.J. Byrnes, Multilayer optical calculations, (2016) 1–20. http://arxiv.org/abs/1603.02720.

[43] A. Densmore, D. Xu, M. Vachon, S. Janz, R. Ma, Y. Li, G. Lopinski, C.C. Luebbert, Q.Y. Liu, J.H. Schmid, A. Delâge, P. Cheben, Arrays of SOI photonic wire biosensors for label-free molecular detection, Proc. SPIE 7606, Silicon Photonics V. 7606 (2010) 1–8. doi:10.1117/12.842027.

[44] V.M.N. Passaro, F. Dell'Olio, B. Casamassima, F. De Leonardis, Guided-Wave Optical Biosensors, Sensors. 7 (2007) 508–536. doi:10.3390/s7040508.

[45] A.F. Gavela, D.G. García, J.C. Ramirez, L.M. Lechuga, Last advances in silicon-based optical biosensors, Sensors (Switzerland). 16 (2016). doi:10.3390/s16030285.

[46] P. Prabhathan, V.M. Murukeshan, Z. Jing, P. V Ramana, Compact SOI nanowire refractive index sensor using phase shifted Bragg grating, Opt. Express. 17 (2009)

15330. doi:10.1364/OE.17.015330.

[47] Y. Binfeng, H. Guohua, Z. Ruohu, C. Yiping, Design of a compact and high sensitive refractive index sensor base on metal-insulator-metal plasmonic Bragg grating, 22 (2014) 1217–1222. doi:10.1364/OE.22.028662.

[48] Y. Liu, W. Peng, X. Zhang, S. Qian, Optical fiber sensor based on capillary wall for highly-sensitive refractive index measurement, Opt. Commun. 319 (2014) 106–109. doi:10.1016/j.optcom.2013.12.084.

[49] S. Sahu, G. Singh, Modeling of grating slot waveguide for high-Q based refractive index sensor, in: 2017 Int. Conf. Comput. Commun. Electron., IEEE, 2017: pp. 394–396. doi:10.1109/COMPTELIX.2017.8004001.

[50] X. Wang, C.K. Madsen, Highly sensitive compact refractive index sensor based on phase-shifted sidewall Bragg gratings in slot waveguide, Appl. Opt. 53 (2014) 96. doi:10.1364/AO.53.000096.

[51] M. Jäger, J. Bruns, E. Ehrentreich-Förster, K. Petermann, Arrays of Individually Addressable SOI Micro Ring Resonators for Bio Sensing, Adv. Photonics 2013. (2013) ST4B.3. doi:10.1364/SENSORS.2013.ST4B.3.

[52] C. Sirawattananon, M. Bahadoran, J. Ali, S. Mitatha, P.P. Yupapin, Analytical vernier effects of a PANDA ring resonator for microforce sensing application, IEEE Trans. Nanotechnol. 11 (2012) 707–712. doi:10.1109/TNANO.2012.2191976.

[53] L. Jin, M. Li, J.-J. He, Highly-sensitive silicon-on-insulator sensor based on two cascaded micro-ring resonators with vernier effect, Opt. Commun. 284 (2011) 156–159. doi:10.1016/j.optcom.2010.08.035.

[54] V. Zamora, P. Lützow, M. Weiland, D. Pergande, H. Schröder, Highly sensitive integrated optical biosensors, 8933 (2014) 1–7. doi:10.1117/12.2039676.

[55] Z. Wang, J. Yao, G. Yuan, L. Yang, Analysis of optical sensing behavior of a novel optical bean-shaped resonator biosensor integrated with MZI configuration, J. Mod. Opt. 61 (2014) 1103–1108. doi:10.1080/09500340.2014.922628.

[56] G.Y. Oh, D.G. Kim, S.H. Kim, H.C. Ki, T.U. Kim, Y.W. Choi, Integrated refractometric sensor utilizing a triangular ring resonator combined with SPR, IEEE Photonics Technol. Lett. 26 (2014) 2189–2192. doi:10.1109/LPT.2014.2349975.

[57] T. Claes, J.G. Molera, K. De Vos, E. Schacht, R. Baets, P. Bienstman, Label-free biosensing with a slot-waveguide-based ring resonator in silicon on insulator, IEEE Photonics J. 1 (2009) 197–204. doi:10.1109/JPHOT.2009.2031596.

[58] C. Ciminelli, F. Dell'Olio, D. Conteduca, C.M. Campanella, M.N. Armenise, High performance SOI microring resonator for biochemical sensing, Opt. Laser Technol. 59 (2014) 60–67. doi:10.1016/j.optlastec.2013.12.011.

[59] A.S. Jugessur, J. Dou, J.S. Aitchison, R.M. De La Rue, M. Gnan, A photonic nano-Bragg grating device integrated with microfluidic channels for bio-sensing applications, Microelectron. Eng. 86 (2009) 1488–1490. doi:10.1016/j.mee.2008.12.002.

[60] X. Wang, C.K. Madsen, Highly sensitive compact refractive index sensor based on phase-shifted sidewall Bragg gratings in slot waveguide, Appl. Opt. 53 (2014) 96. doi:10.1364/AO.53.000096.

[61] F. Kehl, D. Bischof, M. Michler, M. Keka, R. Stanley, Design of a Label-Free, Distributed Bragg Grating Resonator Based Dielectric Waveguide Biosensor, Photonics. 2 (2015) 124–138. doi:10.3390/photonics2010124.

[62] S. Talebi Fard, S.M. Grist, V. Donzella, S.A. Schmidt, J. Flueckiger, X. Wang, W. Shi, A. Millspaugh, M. Webb, D.M. Ratner, K.C. Cheung, L. Chrostowski, Label-free silicon photonic biosensors for use in clinical diagnostics, in: J. Kubby, G.T. Reed (Eds.), 2013: p. 862909. doi:10.1117/12.2005832.

[63] X. Wang, J. Flueckiger, S. Schmidt, S. Grist, S.T. Fard, J. Kirk, M. Doerfler, K.C. Cheung, D.M. Ratner, L. Chrostowski, A silicon photonic biosensor using phase-shifted Bragg gratings in slot waveguide, 8 (2013) 1–8. doi:10.1002/jbio.201300012.

[64] J. Zhang, Y. Zhang, Q. Song, H. Tian, X. Zhang, H. Wu, J. Wang, C. Yu, G. Li, D. Fan, P. Yuan, A double-ring Mach–Zehnder interferometer sensor with high sensitivity, J. Phys. D. Appl. Phys. 45 (2012) 255102. doi:10.1088/0022-3727/45/25/255102.

[65] N.A. Yebo, D. Taillaert, J. Roels, D. Lahem, M. Debliquy, D. Van Thourhout, R. Baets, Silicon-on-Insulator (SOI) Ring Resonator-Based Integrated Optical Hydrogen Sensor, IEEE Photonics Technol. Lett. 21 (2009) 960–962. doi:10.1109/LPT.2009.2021073.

[66] S. Robinson, N. Dhanlaksmi, Photonic crystal based biosensor for the detection of glucose concentration in urine, Photonic Sensors. 7 (2017) 11–19. doi:10.1007/s13320-016-0347-3.

[67] F.L. Hsiao, C. Lee, Computational study of photonic crystals nano-ring resonator for biochemical sensing, IEEE Sens. J. 10 (2010) 1185–1191. doi:10.1109/JSEN.2010.2040172.

[68] C.-C. Hsieh, S. Chakravarty, Y. Zou, L. Zhu, R.T. Chen, High Sensitivity Biosensing Based on Symmetric Coupled Cavity Structure of Photonic Crystal Microcavities, Cleo 2013. 3 (2013) CM2H.8. doi:10.1364/CLEO_SI.2013.CM2H.8.

[69] W. Xie, M. Fiers, S. Selvaraja, P. Bienstman, J. Van Campenhout, P. Absil, D. Van Thourhout, High-Q photonic crystal nanocavities on 300 mm SOI substrate fabricated with 193 nm immersion lithography, J. Light. Technol. 32 (2014) 1457–1462. doi:10.1109/JLT.2014.2308061.

[70] J. Zhou, H. Tian, D. Yang, Q. Liu, Y. Ji, Integration of high transmittance photonic crystal H2 nanocavity and broadband W1 waveguide for biosensing applications based on Silicon-on-Insulator substrate, Opt. Commun. 330 (2014) 175–183. doi:10.1016/j.optcom.2014.04.075.

[71] G. Liang, Z. Luo, K. Liu, Y. Wang, J. Dai, Y. Duan, Fiber Optic Surface Plasmon Resonance–Based Biosensor Technique: Fabrication, Advancement, and

Application, Crit. Rev. Anal. Chem. 46 (2016) 213–223. doi:10.1080/10408347.2015.1045119.

[72] X. Yu, Y. Zhang, S. Pan, P. Shum, M. Yan, Y. Leviatan, C. Li, A selectively coated photonic crystal fiber based surface plasmon resonance sensor, J. Opt. 12 (2010) 15005. doi:10.1088/2040-8978/12/1/015005.

[73] C. Themistos, B.M.A. Rahman, M. Rajarajan, K. Kalli, K.T. V Grattan, Characterization of surface-plasmon modes in metal-clad optical waveguides, Appl. Opt. 45 (2006) 8523. doi:10.1364/AO.45.008523.

[74] M.-H. Chiu, S.-F. Wang, R.-S. Chang, D-type fiber biosensor based on surface-plasmon resonance technology and heterodyne interferometry., Opt. Lett. 30 (2005) 233–235. doi:10.1364/OL.30.000233.

[75] X. Wang, Y. Wang, J. Flueckiger, R. Bojko, A. Liu, A. Reid, J. Pond, N. a F. Jaeger, L. Chrostowski, Precise control of the coupling coefficient through destructive interference in silicon waveguide Bragg gratings., Opt. Lett. 39 (2014) 5519–22. doi:10.1364/OL.39.005519.

[76] M. Fu, Refractive Index Sensing Based on the Reflectivity of the Backward Cladding-Core Mode Coupling in a Concatenated Fiber Bragg Grating and a Long Period Grating, 12 (2012) 1415–1420.

[77] S. Schmidt, J. Flueckiger, W. Wu, S.M. Grist, S. Talebi Fard, V. Donzella, P. Khumwan, E.R. Thompson, Q. Wang, P. Kulik, X. Wang, A. Sherwali, J. Kirk, K.C. Cheung, L. Chrostowski, D. Ratner, Improving the performance of silicon photonic rings, disks, and Bragg gratings for use in label-free biosensing, in: H. Mohseni, M.H. Agahi, M. Razeghi (Eds.), Biosensing Nanomedicine VII, 2014: p. 91660M. doi:10.1117/12.2062389.

[78] C.I.L. Justino, T.A. Rocha-Santos, A.C. Duarte, Review of analytical figures of merit of sensors and biosensors in clinical applications, TrAC Trends Anal. Chem. 29 (2010) 1172–1183. doi:10.1016/j.trac.2010.07.008.

[79] R. Kazemi-darsanaki, A. Azizzadeh, M. Nourbakhsh, G. Raeisi, M. Azizollahiali-, Biosensors: Functions and Applications, 2 (2013) 20–23.

[80] C. Chen, Q. Xie, D. Yang, H. Xiao, Y. Fu, Y. Tan, S. Yao, Recent advances in electrochemical glucose biosensors: a review, RSC Adv. 3 (2013) 4473. doi:10.1039/c2ra22351a.

[81] Y.Q. Fu, J.K. Luo, X.Y. Du, A.J. Flewitt, Y. Li, G.H. Markx, A.J. Walton, W.I. Milne, Recent developments on ZnO films for acoustic wave based bio-sensing and microfluidic applications: a review, Sensors Actuators, B Chem. 143 (2010) 606–619. doi:10.1016/j.snb.2009.10.010.

[82] J.L. Arlett, E.B. Myers, M.L. Roukes, Comparative advantages of mechanical biosensors, Nat. Nanotechnol. 6 (2011) 203–215. doi:10.1038/nnano.2011.44.

[83] C.-Y. Yao, Biosensors for hepatitis B virus detection, World J. Gastroenterol. 20 (2014) 12485. doi:10.3748/wjg.v20.i35.12485.

[84] A. Tlili, A. Abdelghani, S. Hleli, M. a. Maaref, Electrical Characterization of a Thiol SAM on Gold as a First Step for the Fabrication of Immunosensors based on a Quartz Crystal Microbalance, Sensors. 4 (2004) 105–114. doi:10.3390/s40670105.

[85] S. Sahu, J. Ali, G. Singh, Refractive index biosensor using sidewall gratings in dual-slot waveguide, Opt. Commun. 402 (2017) 408–412. doi:10.1016/j.optcom.2017.06.051.

[86] E. Di Fabrizio, S. Schlücker, J. Wenger, R. Regmi, H. Rigneault, G. Calafiore, M. West, S. Cabrini, M. Fleischer, N.F. van Hulst, M.F. Garcia-Parajo, A. Pucci, D. Cojoc, C.A.E. Hauser, M. Ni, Roadmap on biosensing and photonics with advanced nano-optical methods, J. Opt. 18 (2016) 63003. doi:10.1088/2040-8978/18/6/063003.

[87] J. Zhang, L. Zhang, W. Xu, Surface plasmon polaritons: physics and applications, J. Phys. D. Appl. Phys. 45 (2012) 113001. doi:10.1088/0022-3727/45/11/113001.

[88] K. Tainaka, R. Sakaguchi, H. Hayashi, S. Nakano, F.F. Liew, T. Morii, Design

strategies of fluorescent biosensors based on biological macromolecular receptors, Sensors. 10 (2010) 1355–1376. doi:10.3390/s100201355.

[89] M. Strianese, M. Staiano, G. Ruggiero, T. Labella, C. Pellecchia, S. D'Auria, Fluorescence-based biosensors, Methods Mol. Biol. 875 (2012) 193–216. doi:10.1007/978-1-61779-806-1_9.

[90] J.S. Hansen, J.B. Christensen, Recent advances in fluorescent arylboronic acids for glucose sensing, Biosensors. 3 (2013) 400–418. doi:10.3390/bios3040400.

[91] K. Tiefenthaler, W. Lukosz, Sensitivity of grating couplers as integrated-optical chemical sensors, J. Opt. Soc. Am. B. 6 (1989) 209. doi:10.1364/JOSAB.6.000209.

[92] K.E. Zinoviev, A.B. González-Guerrero, C. Domínguez, L.M. Lechuga, Integrated bimodal waveguide interferometric biosensor for label-free analysis, J. Light. Technol. 29 (2011) 1926–1930. doi:10.1109/JLT.2011.2150734.

[93] X. Guo, Surface plasmon resonance based biosensor technique: A review, J. Biophotonics. 5 (2012) 483–501. doi:10.1002/jbio.201200015.

[94] E. Wijaya, C. Lenaerts, S. Maricot, J. Hastanin, S. Habraken, J. Vilcot, R. Boukherroub, S. Szunerits, Surface plasmon resonance-based biosensors : From the development of different SPR structures to novel surface functionalization strategies, Curr. Opin. Solid State Mater. Sci. 15 (2011) 208–224. doi:10.1016/j.cossms.2011.05.001.

[95] S. Patskovsky, M. Meunier, A.V. Kabashin, Surface plasmon resonance polarizator for biosensing and imaging, Opt. Commun. 281 (2008) 5492–5496. doi:10.1016/j.optcom.2008.07.061.

[96] Y. Du, L. Shi, M. Hong, H. Li, D. Li, M. Liu, A surface plasmon resonance biosensor based on gold nanoparticle array, Opt. Commun. 298–299 (2013) 232–236. doi:10.1016/j.optcom.2013.02.024.

[97] S.D. Keighley, P. Li, P. Estrela, P. Migliorato, Optimization of DNA immobilization on gold electrodes for label-free detection by electrochemical impedance

spectroscopy, Biosens. Bioelectron. 23 (2008) 1291–1297. doi:10.1016/j.bios.2007.11.012.

[98] S. Feng, T. Lei, H. Chen, H. Cai, X. Luo, A.W. Poon, Silicon photonics: From a microresonator perspective, Laser Photonics Rev. 6 (2012) 145–177. doi:10.1002/lpor.201100020.

[99] L. Liao, A. Liu, J. Basak, H. Nguyen, M. Paniccia, Y. Chetrit, D. Rubin, Silicon photonic modulator and integration for high-speed applications, Tech. Dig. - Int. Electron Devices Meet. IEDM. (2008) 0–3. doi:10.1109/IEDM.2008.4796726.

[100] T.-K. Lee, G.-Y. Oh, H.-S. Kim, D.G. Kim, Y.-W. Choi, A high-Q biochemical sensor using a total internal reflection mirror-based triangular resonator with an asymmetric Mach–Zehnder interferometer, Opt. Commun. 285 (2012) 1807–1813. doi:10.1016/j.optcom.2011.11.089.

[101] L. Huang, H. Tian, J. Zhou, Q. Liu, P. Zhang, Y. Ji, Label-free optical sensor by designing a high-Q photonic crystal ring-slot structure, Opt. Commun. 335 (2015) 73–77. doi:10.1016/j.optcom.2014.09.014.

[102] G. Yuan, L. Gao, Y. Chen, X. Liu, J. Wang, Z. Wang, Improvement of optical sensing performances of a double-slot-waveguide- based ring resonator sensor on silicon-on-insulator platform, Optik (Stuttg). 125 (2014) 850–854. doi:10.1016/j.ijleo.2013.07.088.

[103] P. Prabhathan, V.M. Murukeshan, Silicon waveguide multiplexed sensor array configuration for label-free biosensing applications, J. Indian Inst. Sci. 94 (2014) 273–282. http://journal.library.iisc.ernet.in/index.php/iisc/article/view/4512.

[104] S. TalebiFard, S. Schmidt, W. Shi, W. Wu, N.A.F. Jaeger, E. Kwok, D.M. Ratner, L. Chrostowski, Optimized sensitivity of Silicon-on-Insulator (SOI) strip waveguide resonator sensor, Biomed. Opt. Express. 8 (2017) 500. doi:10.1364/BOE.8.000500.

[105] M.C. Estevez, M. Alvarez, L.M. Lechuga, Integrated optical devices for lab-on-a-chip biosensing applications, Laser Photon. Rev. 6 (2012) 463–487.

doi:10.1002/lpor.201100025.

[106] S. Balslev, A.M. Jorgensen, B. Bilenberg, K.B. Mogensen, D. Snakenborg, O. Geschke, J.P. Kutter, A. Kristensen, Lab-on-a-chip with integrated optical transducers, Lab Chip. 6 (2006) 213–217. doi:10.1039/B512546D.

[107] D. Mark, S. Haeberle, G. Roth, F. Von Stetten, R. Zengerle, Microfluidic lab-on-a-chip platforms: Requirements, characteristics and applications, NATO Sci. Peace Secur. Ser. A Chem. Biol. (2010) 305–376. doi:10.1007/978-90-481-9029-4-17.

[108] S. Kumar, T. Srinivas, A. Selvarajan, Beam propagation method and its application to integrated optic structures and optical fibers, Pramana. 34 (1990) 347–358. doi:10.1007/BF02845870.

[109] K. Han, C.-H. Chang, Numerical Modeling of Sub-Wavelength Anti-Reflective Structures for Solar Module Applications, Nanomaterials. 4 (2014) 87–128. doi:10.3390/nano4010087.

[110] M. Paniccia, M. Paniccia, M. Morse, M. Morse, M. Salib, M. Salib, Integrated Photonics, 2004.

[111] R.G. Hunsperger, Optical Waveguide Modes, in: Integr. Opt., Springer New York, New York, NY, 2009: pp. 17–31. doi:10.1007/b98730_2.

[112] H. Kogelnik, V. Ramaswamy, Scaling Rules for Thin-Film Optical Waveguides, Appl. Opt. 13 (1974) 1857–1862. doi:10.1364/AO.13.001857.

[113] D.F.G. Gallagher, T.P. Felici, Eigenmode expansion methods for simulation of optical propagation in photonics: pros and cons, in: Y.S. Sidorin, A. Tervonen (Eds.), Integr. …, 2003: p. 69. doi:10.1117/12.473173.

[114] M. Gnan, W.C.L. Hopman, G. Bellanca, R.M. De Ridder, R.M.D. La Rue, P. Bassi, Closure of the stop-band in photonic wire Bragg gratings, 17 (2009) 11769–11775.

[115] A. Cusano, A. Iadicicco, S. Campopiano, M. Giordano, A. Cutolo, Thinned and micro-structured fibre Bragg gratings: towards new all-fibre high-sensitivity chemical sensors, J. Opt. A Pure Appl. Opt. 7 (2005) 734–741. doi:10.1088/1464-

4258/7/12/005.

[116] D. Arora, J. Prakash, H. Singh, A. Wason, Reflectivity and Braggs Wavelength in FBG, Int. J. Eng. 5 (2011) 341–349.

[117] W.-P. Huang, Coupled-mode theory for optical waveguides: an overview, J. Opt. Soc. Am. A. 11 (1994) 963. doi:10.1364/JOSAA.11.000963.

[118] J. Buus, D.J. Blumenthal, M.-C. Amann, Tunable laser diodes and related optical sources, 2005. doi:10.1109/9780470546758.

[119] R.P.Y. Ghanshyam Singh, Vijay Janyani, Modeling of a high performance Mach – Zehnder interferometer all optical switch, Opt. Appl. XLII (2012) 613–625. doi:10.5277/oa120315.

[120] G. Singh, Modeling of a high-performance multimode interference optical switch using reconfigurable image modulated region, Opt. Eng. 51 (2012) 74006. doi:10.1117/1.OE.51.7.074006.

[121] M. Deng, C.-P. Tang, T. Zhu, Y.-J. Rao, Highly sensitive bend sensor based on Mach–Zehnder interferometer using photonic crystal fiber, Opt. Commun. 284 (2011) 2849–2853. doi:10.1016/j.optcom.2011.02.061.

[122] G. Calo, A. Farinola, V. Petruzzelli, DESIGN AND OPTIMIZATION OF HIGH SENSITIVITY PHOTONIC INTERFEROMETRIC BIOSENSORS ON POLYMERIC WAVEGUIDES, Prog. Electromagn. Res. Lett. 33 (2012) 151–166. doi:10.2528/PIERL12051303.

[123] Y. Vlasov, S. McNab, Losses in single-mode silicon-on-insulator strip waveguides and bends., Opt. Express. 12 (2004) 1622–1631. doi:10.1364/OPEX.12.001622.

[124] K.K. Lee, D.R. Lim, H.-C. Luan, A. Agarwal, J. Foresi, L.C. Kimerling, Effect of size and roughness on light transmission in a Si/SiO2 waveguide: Experiments and model, Appl. Phys. Lett. 77 (2000) 1617. doi:10.1063/1.1308532.

[125] H. Yun, Z. Lu, Y. Wang, W. Shi, L. Christowski, N.A.F. Jaeger, 2x2 Broadband Adiabatic 3-dB Couplers on SOI Strip Waveguides for TE and TM modes, CLEO

2015. (2015) 3–4.

[126] Y. Wang, Grating Coupler Design Based on Silicon-on-Insulator, University of British Columbia, 2013. https://open.library.ubc.ca/cIRcle/collections/24/items/1.0073806.

[127] Applied Nanotools Inc., (n.d.).

[128] R.J. Bojko, J. Li, L. He, T. Baehr-Jones, M. Hochberg, Y. Aida, Electron beam lithography writing strategies for low loss, high confinement silicon optical waveguides, J. Vac. Sci. Technol. B Microelectron. Nanom. Struct. 29 (2011) 06F309. doi:10.1116/1.3653266.

[129] M. Caverley, Python code, (n.d.). http://siepic.ubc.ca/probestation.

[130] S. Najafgholinezhad, S. Olyaee, A photonic crystal biosensor with temperature dependency investigation of micro-cavity resonator, Opt. - Int. J. Light Electron Opt. 125 (2014) 6562–6565. doi:10.1016/j.ijleo.2014.08.043.

[131] Z. Wang, H. Yan, Z. Wang, Y. Zou, C.-J. Yang, S. Chakravarty, H. Subbaraman, N. Tang, X. Xu, D.L. Fan, A.X. Wang, R.T. Chen, Ultralow-loss waveguide crossings for the integration of microfluidics and optical waveguide sensors, in: B.L. Gray, H. Becker (Eds.), 2015: p. 932012. doi:10.1117/12.2078384.

[132] Z. Chen, J. Flueckiger, X. Wang, F. Zhang, H. Yun, Z. Lu, M. Caverley, Y. Wang, N.A.F. Jaeger, L. Chrostowski, Spiral Bragg grating waveguides for TM mode silicon photonics, Opt. Express. 23 (2015) 25295. doi:10.1364/OE.23.025295.

[133] A.N. Bashkatov, E.A. Genina, Water refractive index in dependence on temperature and wavelength: a simple approximation, in: V. V. Tuchin (Ed.), 2003: pp. 393–395. doi:10.1117/12.518857.

[134] Q. Liu, Z. Gu, J.S. Kee, M.K. Park, Silicon waveguide filter based on cladding modulated anti-symmetric long-period grating, Opt. Express. 22 (2014) 29954. doi:10.1364/OE.22.029954.

[135] C. Wu, K. Lin, Y. Liang, C. Huang, Y. Hung, Silicon Photonic Temperature Sensor

Employing Narrowband Cladding-modulated Bragg Reflectors, in: Conf. Lasers Electro-Optics, OSA, Washington, D.C., 2016: p. JTh2A.98. doi:10.1364/CLEO_AT.2016.JTh2A.98.

[136] D.T. Spencer, M. Davenport, S. Srinivasan, J. Khurgin, P.A. Morton, J.E. Bowers, Low kappa, narrow bandwidth Si_3N_4 Bragg gratings, Opt. Express. 23 (2015) 30329. doi:10.1364/OE.23.030329.

[137] X.C. Tong Ph.D, Advanced Materials for Integrated Optical Waveguides, Springer International Publishing, Cham, 2014. doi:10.1007/978-3-319-01550-7.

[138] M. Gould, A. Pomerene, C. Hill, S. Ocheltree, Y. Zhang, T. Baehr-Jones, M. Hochberg, Ultra-thin silicon-on-insulator strip waveguides and mode couplers, Appl. Phys. Lett. 101 (2012) 221106. doi:10.1063/1.4768296.

[139] X. Wang, S. Grist, J. Flueckiger, N.A.F. Jaeger, L. Chrostowski, Silicon photonic slot waveguide Bragg gratings and resonators Abstract :, 21 (2013) 19029–19039. doi:10.1364/OE.21.019029.

[140] K.F. Palmer, D. Williams, Optical properties of water in the near infrared*, J. Opt. Soc. Am. 64 (1974) 1107. doi:10.1364/JOSA.64.001107.

[141] H. Sun, A. Chen, L.R. Dalton, Enhanced evanescent confinement in multiple-slot waveguides and its application in biochemical sensing, IEEE Photonics J. 1 (2009) 48–57. doi:10.1109/JPHOT.2009.2025602.

[142] C.F. Carlborg, K.B. Gylfason, A. Kaźmierczak, F. Dortu, M.J. Bañuls Polo, A. Maquieira Catala, G.M. Kresbach, H. Sohlström, T. Moh, L. Vivien, J. Popplewell, G. Ronan, C.A. Barrios, G. Stemme, W. van der Wijngaart, A packaged optical slot-waveguide ring resonator sensor array for multiplex label-free assays in labs-on-chips, Lab Chip. 10 (2010) 281–290. doi:10.1039/B914183A.

[143] D. Bischof, F. Kehl, M. Michler, Design method for a distributed Bragg resonator based evanescent field sensor, Opt. Commun. 380 (2016) 273–279. doi:10.1016/j.optcom.2016.06.013.

[144] M. Gnan, G. Bellanca, H.M.H. Chong, P. Bassi, R.M. De La Rue, Modelling of photonic wire Bragg gratings, Opt. Quantum Electron. 38 (2006) 133–148. doi:10.1007/s11082-006-0010-0.

[145] L. Huang, H. Tian, J. Zhou, Q. Liu, P. Zhang, Y. Ji, Label-free optical sensor by designing a high- Q photonic crystal ring – slot structure, Opt. Commun. 335 (2015) 73–77. doi:10.1016/j.optcom.2014.09.014.

[146] L. Sun, J. Yuan, T. Ma, X. Sang, B. Yan, K. Wang, C. Yu, Design and optimization of silicon concentric dual-microring resonators for refractive index sensing, Opt. Commun. 395 (2017) 212–216. doi:10.1016/j.optcom.2016.05.052.

[147] J.G. Wangüemert-pérez, P. Cheben, A. Ortega-moñux, C. Alonso-ramos, D. Pérez-galacho, R. Halir, I. Molina-fernández, D. Xu, J.H. Schmid, Evanescent field waveguide sensing with subwavelength grating structures in silicon-on-insulator, 39 (2014) 4442–4445.

[148] J. Wang, I. Glesk, L.R. Chen, Subwavelength grating filtering devices, 22 (2014) 15335–15345. doi:10.1364/OE.22.015335.

[149] L. Huang, H. Tian, D. Yang, J. Zhou, Q. Liu, P. Zhang, Y. Ji, Optimization of figure of merit in label-free biochemical sensors by designing a ring defect coupled resonator, Opt. Commun. 332 (2014) 42–49. doi:10.1016/j.optcom.2014.06.033.

[150] P. Cheben, P.J. Bock, J.H. Schmid, J. Lapointe, S. Janz, D.-X. Xu, A. Densmore, A. Delâge, B. Lamontagne, T.J. Hall, Refractive index engineering with subwavelength gratings for efficient microphotonic couplers and planar waveguide multiplexers, Opt. Lett. 35 (2010) 2526. doi:10.1364/OL.35.002526.

[151] P.J. Bock, P. Cheben, J.H. Schmid, J. Lapointe, A. Delâge, S. Janz, G.C. Aers, D.-X. Xu, A. Densmore, T.J. Hall, Subwavelength grating periodic structures in silicon-on-insulator: a new type of microphotonic waveguide., Opt. Express. 18 (2010) 20251–62. doi:10.1364/OE.18.020251.

[152] R. Halir, P.J. Bock, P. Cheben, A. Ortega-mo, C. Alonso-ramos, J.H. Schmid, J.

Lapointe, D. Xu, J.G. Wang, S. Janz, Waveguide sub-wavelength structures : a review of principles, 49 (2015) 25–49. doi:10.1002/lpor.201400083.

[153] Z. Wang, X. Xu, D. Fan, Y. Wang, R.T. Chen, High quality factor subwavelength grating waveguide micro-ring resonator based on trapezoidal silicon pillars, Opt. Lett. 41 (2016) 3375. doi:10.1364/OL.41.003375.

Appendix 1

(a) Transfer Function

The expression for electric field intensity of propagating signals in two arms is reported in [11] is given as,

$$E_0 = \frac{E_i}{2}\left(e^{-i\beta_1 L_1 - \frac{\alpha_1}{2}L_1} + e^{-i\beta_2 L_2 - \frac{\alpha_2}{2}L_2}\right)$$

In terms of Intensity, I_0

$$\frac{I_0}{I_i} = \frac{1}{4}\left|e^{-i\beta_1 L_1 - \frac{\alpha_1}{2}L_1} + e^{-i\beta_2 L_2 - \frac{\alpha_2}{2}L_2}\right|^2$$

For the lossless condition, $\beta = \beta_1 = \beta_2$ and $\alpha_1 = \alpha_2 = 0$,

where $\beta = \frac{2\pi n_g}{\lambda}$ is propagation constant, n_g is group index and α is propagation loss,

$$\frac{I_0}{I_i} = \frac{1}{4}|1 + \cos(\Delta\beta \cdot L)|^2$$

where I_0 and I_i are output and input intensity respectively, $\Delta\emptyset = \emptyset_1 - \emptyset_2 = \beta \cdot \Delta L$ is phase shift incurred and ΔL is path difference between the two arms [12].

(b) Free Spectral Range (FSR)

FSR is the distance between the two adjacent peaks in the transmission spectra. For an imbalanced MI (different arm lengths L_1 and L_2) the FSR can be derived by considering the same technique as represented for Mach Zehnder interferometer in [13].

$$FSR = \Delta\lambda = \lambda_m - \lambda_{m+1}$$

$$\Delta\emptyset = \emptyset_m - \emptyset_{m+1}$$

$$2\pi = \beta_m 2\Delta L - \beta_{m+1} 2\Delta L$$

$$\Delta\beta = \beta_m - \beta_{m+1} = \frac{\pi}{\Delta L}$$

Approximation of β varied linearly with λ

$$\Delta\beta \simeq -\frac{d\beta}{d\lambda}\Delta\lambda$$

By combining above two equations (7) and (8)

$$\Delta\lambda \approx -\Delta\beta\left(\frac{d\beta}{d\lambda}\right)^{-1} = -\frac{\pi}{\Delta L}\left(\frac{d\beta}{d\lambda}\right)^{-1}$$

$$\frac{d\beta}{d\lambda} = \frac{2\pi}{\lambda}\frac{dn}{d\lambda} + 2\pi n\left(-\frac{1}{\lambda^2}\right) = -\frac{2\pi}{\lambda^2}\left(n - \frac{dn}{d\lambda}\lambda\right)$$

From the above two equations (9) and (10) we can solve for $\Delta\lambda$

$$\text{FSR} = \Delta\lambda = \frac{\lambda^2}{2\Delta L n_g}$$

Brief CV

Sourabh Sahu received his B.E. degree from RGPV University, Bhopal, India in 2010 in Electronics and Communication Engineering with Honors. He received his M.Tech. from Malaviya National Institute of Technology (MNIT) Jaipur, India in 2012. After that, he had worked as an Assistant Professor at Gyan Ganga College of Technology, Jabalpur, India. Since July 2014, he has been pursuing Ph.D. at Malaviya National Institute of Technology, Jaipur, India. His areas of interest are silicon photonics, photonic crystal fibers, photonic crystal based devices, optoelectronics. He is currently a student member of Optical Society of America (OSA) and IEEE. He was also a vice president of OSA Student Chapter of MNIT Jaipur.